Modelling Magnetocaloric Heat Pumps

Srikrishna Sivaramakrishnan
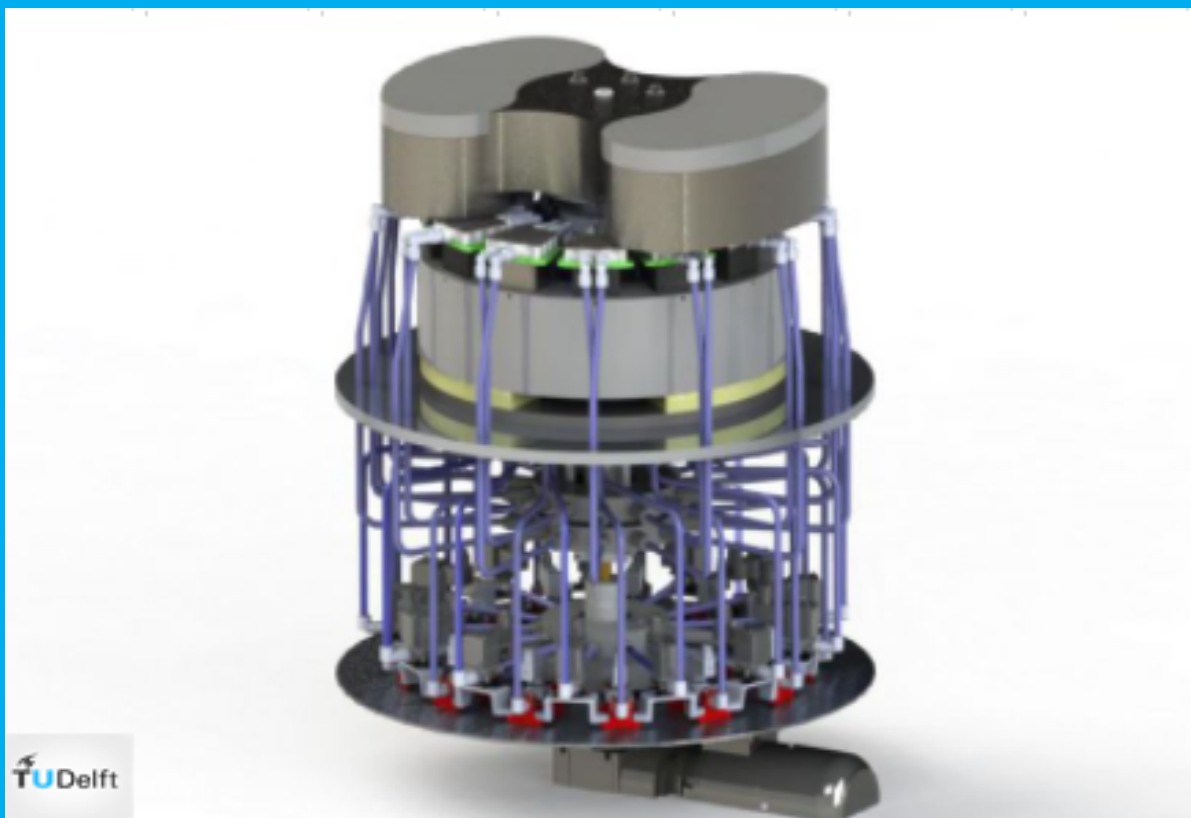
Modelling Magnetocaloric Heat Pumps

By

Srikrishna Sivaramakrishnan

in partial fulfilment of the degree of Master of Science at Delft University of Technology, to be defended publicly on Tuesday June 29, 2021 at 1:30 PM.

An electronic version of this thesis is available at `http://repository.tudelft.nl/`

TUDelft

Acknowledgment

This project on Magnetocaloric heat pumps has been a great learning experience for me in the past 12 months. Therefore, I would like to express my gratitude to the following people for making this experience a reality:

1. Dr. ir. C. A. Infante Ferreira for his experience, knowledge and guidance throughout this project.

2. Ir. D. F. Pineda Quijano for his constant inputs and guidance that brought about the success of completing the project.

Abstract

Magnetocaloric heat pumps are those types of heat pumps which use a solid MagnetoCaloric Material (MCM) in place of a refrigerant to provide the work for the heat pump. MCMs are materials whose temperature changes on the application or removal of a magnetic field. This effect is known as the MagnetoCaloric Effect (MCE). Magnetocaloric heat pumps have the potential in replacing the conventional vapour compression technology for Dutch dwellings, since they have minimum environmental impact due to the absence of the coolant fluids that can harm the environment. A model of the regenerator of the magnetocaloric heat pump is developed in this project having in mind the application of this type of heat pumps to Dutch dwellings. The magnetic field that is used in the development of the model is 0.875 T, with permanent magnets being the source of the magnetic field. A sensitivity analysis is carried out in order to obtain the methods to optimize the regenerator for improving the performance of the heat pump. The performance of the heat pump is measured through its average cooling capacity, average heating capacity, temperature span and Coefficient of Performance (COP) for heating. The MCM used for the regenerators is Gd with a total mass of 1.18 kg. The parameter that influences the performance of the heat pump the most is the porosity of the regenerator. The heat losses through the casing have the least impact on the performance of the regenerator. The frequency of the cycle also has a profound impact on the heating capacity and cooling capacity up to temperature spans of around 18 K, but it does not have such an impact on the heating COP. After increasing the frequency, decreasing the particle diameter and decreasing the porosity, the heating capacity and the temperature span are optimized. For a temperature span of 15 K, the heating capacity is 164.2 W, and for a temperature span of 20 K, the heating capacity is 99.1 W.

Contents

Nomenclature

A Area (m^2)

A_c Cross sectional area (m^2)

A_s Area of heat exchange (m^2)

B Magnetic induction (T ($N\ A^{-1}\ m^{-1}$))

b Width (m)

C Heat capacity of the material ($J\ K^{-1}$)

$\dot{C}$ Thermal power capacity ($W\ K^{-1}$)

C^* Ratio of heat capacities

c Specific Heat capacity of the material ($J\ kg^{-1}\ K^{-1}$)

c_p Specific Heat capacity at constant pressure ($J\ kg^{-1}\ K^{-1}$)

D Longitudinal thermal dispersion ($m^2\ s^{-1}$)

d Diameter (m)

d_h Hydraulic diameter (m)

d_p Particle diameter (m)

E Ergun Constant

F Frequency (Hz)

f Friction factor

H Magnetic field intensity ($A\ m^{-1}$)

h Heat Transfer Coefficient ($W\ m^{-2}\ K^{-1}$)

I_{vol} Ratio of volumes

K Permeability of the porous media (m^2)

K_f Friction factor

k Thermal conductivity ($W\ m^{-1}\ K^{-1}$)

L Length (m)

$\dot{L}$ Heat losses (W)

M Magnetization of the material ($A\ m^{-1}$)

m Mass (kg)

$\dot{m}$ Mass flow rate ($kg\ s^{-1}$)

Nu Nusselt number

NTU Number of Transfer Units

n Position vector

nt Number of time steps

P Pressure (Pa)

Pr Prandtl Number

$\dot{Q}$ Heat Rate (W)

q Volumetric specific heat ($J\ m^{-3}$)

$\dot{q}$ Heat Rate per unit volume ($W\ m^{-3}$)

R Thermal resistance ($m^2\ K\ W^{-1}$)

RD Relative Deviation

Re Reynolds Number

S Total entropy of the magnetic material ($J\ K^{-1}$)

$\dot{S}$ Entropy rate ($W\ K^{-1}$)

s Specific magnetic entropy ($J\ m^{-3}\ K^{-1}$)

T Temperature of the substance (K)

$\dot{T}$ Heat loss rate ($K s^{-1}$)

t time (s)

U Overall heat transfer coefficient ($W\ m^{-2}\ K^{-1}$)

UT Utilization

u velocity of flow ($m\ s^{-1}$)

V Volume (m^3)

$\dot{V}$ Volumetric Flow Rate ($m^3\ s^{-1}$)

$\dot{W}$ Power given by or to the system (W)

x distance in the longitudinal direction (m)

y distance in the transverse direction (m)

Z Height (m)

z distance in the vertical direction (m)

Greek Symbols

α_s Thermal diffusivity of solid material ($m^2\ s^{-1}$)

α_f Thermal diffusivity of fluid ($m^2\ s^{-1}$)

γ Magnetic potential (A)

Δ Finite change in quantity

∇ Differential operator (m^{-1})

ϵ Porosity

κ Volumetric heat capacity ($J\ m^{-3}\ K$)

μ Dynamic viscosity ($Pa\ s$)

ν Kinematic viscosity ($m^2\ s^{-1}$)

μ_0 Permeability of free space ($N\ A^{-2}$)

μ_r Relative magnetic permeability

ρ Density ($kg\ m^{-3}$)

σ Heat transfer area per unit volume ($m^2\ m^{-3}$)

ϕ Time period of cycle (s)

ψ Effectiveness

Abbreviations

AMR   Active Magnetic Regeneration

BHE   Borehole Heat Exchangers

CHEX Cold Heat Exchanger

COP   Coefficient of Performance

CV   Control Volume

DBHE Deep Borehole Heat Exchangers

DC   Direct Current

DNS   Direct Numerical Simulation

EGM   Entropy Generation Minimization

FEV   Fully Electric Vehicles

FOMT   First Order Magnetocaloric Material

HHEX   Hot Heat Exchanger

HTF   Heat Transfer Fluid

HX   Heat Exchanger

LCCP   Life Cycle Climate Performance

MCE   Magnetocaloric Effect

MCM   Magnetocaloric Material

MCU   Magnetocaloric Units

NTU   Number of Transfer Units

PEC   Performance Evaluation Criteria

SOMT   Second Order Magnetocaloric Material

TEWI   Total Equivalent Warming Impact

Superscripts

n Number

Subscripts

0   Reference value

ad   Adiabatic

air   Atmospheric air

C   Cold Heat Exchanger/ Cold End

c   cross section

case   casing

cold cold

cv   Control Volume

cycle Cycle

d   Demagnetizing

disp Axial dispersion

e External

eff Effective

el Electronic

end End

exp Experimental

f Fluid

g Grout-filled borehole

gen Generation

H Hot Heat Exchanger/ Hot End

hex heat exchanger

hot Hot

HT Heat transfer

i inner

in inlet/internal

lat Lattice

leak Leakage

load Thermal Load

loss Loss

M Magnetic

mag Magnetic work

max Maximum

MCE Magnetocaloric Effect

min Minimum

o Outer

out outlet

P at constant pressure

p particle

pipe   pipe of heat exchanger

pump   pumping work

r   Refrigerant (HTF)

Reg   Regenerator

S   Reservoir

s   solid

sat   Saturated

simu   simulation

span   Span

stat   Static

visco Viscous

w   Warm-end

z   in the vertical direction

1

Introduction

1.1. Motivation for Magnetic Refrigeration

Vapour compression technology has been widely used for commercial refrigeration, heat-pumping and air-conditioning for many years. The usefulness of vapour compression technology for these applications lies on its maturity, optimized production and maintenance costs, and safety and reliability during operation. Another factor that contributes to the wide usage of vapour compression technology is the comparatively high values of energy efficiency of around 60% for large-scale appliances [1]. However, the major issue that puts the vapour compression technology at a disadvantage is that, the refrigerants used for many applications can adversely affect the environment. The vapour compression systems currently comprise 7.8% of global pollution, 37% of which comes from the refrigerants used [2]. In particular, the use of hydrofluorocarbons as refrigerants is expected to be terminated within 30-40 years, given that they have a very high global warming. These problems of vapour compression technology have stimulated a strong search for alternatives to the currently used refrigerants for air-conditioning and refrigeration. During this search, several researchers have investigated the possible use of caloric or ferroic technology. Although caloric technology is still in the research and development phase, many researchers assert that this technology for refrigeration and heat-pumping can be the most important option for the future. Caloric technology is a solid-state technology that utilizes solid materials with caloric effects. These materials are to be used in place of the existing refrigerants. Caloric effects can be classified into three types: magnetocaloric, electrocaloric and mechanocaloric effects. Materials that exhibit two or more of these effects are considered to be multi-caloric or multi-ferroic. Since caloric technology makes use of solid-state materials, it poses no threat to the environment. Of the three types of caloric effects, Magnetocaloric effects are the most developed for refrigeration, heat-pumping and air conditioning [2].

1.2. Objective and Overview of the Report

The final objective of the project is to develop a model that can be used as a design tool of active magnetocaloric regenerators to be used in magnetocaloric heat pumps for Dutch dwellings. Therefore, the heat sink for the heat pump is a Dutch dwelling. The total heating power required in well-insulated Dutch dwellings on the coldest day is 3 kW, and it is divided into two parts, namely the space heating and the domestic hot water buffer. The focus of the project is mainly the development and optimization of the magnetocaloric regenerator. The heat source that can be used to provide the heat is a Borehole Heat Exchanger (BHE). However, the BHE is not considered for the model development and is only briefly discussed in this report. The model is developed using permanent magnets as the magnetic field source with a field intensity of 0.875 T. The performance of the heat pump is assessed through parameters like temperature span, heating capacity, cooling capacity and the COP. The project also focuses on a sensitivity analysis of the developed magnetic heat pump with different parameters for assessing its performance, and finding ways to optimize it.

This project report begins with a literature review in Chapter 2 wherein, the previous research conducted in the field of magnetocaloric heat pumps is extensively discussed. This includes the governing equations to model the heat transfer between the solid material in the regenerator and the Heat Transfer Fluid (HTF).

The literature review also includes a brief discussion of the heat source and the heat sink. The discussion of the heat source and sink is followed by the selection of important aspects of the heat pump cycle like the geometry of the regenerator and the HTF. The schematic of the cycle is then described in detail along with the heat transfer model for the regenerator and the HTF in Chapter 3. The model is then validated with the results of previous research conducted in magnetocaloric heat pumps. After validation, the regenerator model is improved for increasing the accuracy in obtaining its performance parameters. A sensitivity analysis of the different parameters of the regenerator is then carried out in order to obtain methods to optimize the regenerator's performance in Chapter 4.

1.3. Research Questions

To identify the research gap in the project, some research questions are to be answered. These research questions pave the way to achieve the objectives of this project. After these questions are answered, the design of the regenerator of the magnetocaloric heat pump can be carried out taking into account the existing prototypes and dimensions that are discussed in the following chapter. The design of the regenerator is guided by finding the answers to the following questions:

1. What is the most suitable material that can be used as MCM?

2. What is the maximum temperature span that can be obtained for magnetic heat pumps for the chosen MCM?

3. What are the maximum cooling and heating capacities that can be obtained when there is minimum temperature span across the regenerator?

4. What are the governing equations for numerically modelling the heat transfer between the regenerator and the HTF?

5. How does the heat exchange through the casing affect the performance of the regenerator?

6. What kind of method can be used to model the magnetization and demagnetization of the MCM?

To answer the first question, the choice of the MCM is made based on its availability in the market and how easy it is to obtain its properties that are required for developing the heat transfer model. The answer to the second question is important in order to understand whether this temperature span is sufficient for the heating in Dutch dwellings or if it has to be improved. The answer to the third question helps in understanding whether the thermal power is sufficient for Dutch dwellings. The answer to the fourth question helps in developing a numerical model for the heat transfer between the regenerator and the HTF. Answering the fifth question helps in understanding how important the heat loss through the casing is, for developing the model taking it into account. The answer to the sixth question is crucial since it constitutes the work provided to the heat pump and therefore, influences the performance of the heat pump.

The next set of questions pertains to the results of the model required for validation and optimization of the regenerator:

1. Which parameters influence the performance of the regenerator the most?

2. What methods can be implemented in order to optimize the performance of the regenerator?

The research questions listed in this part of the chapter are addressed in the consequent chapters.

2

Literature Review

This chapter is focused on the discussion of previous work carried out in the field of magnetic heat pumps by various authors. This includes some basic thermodynamic equations for magnetic refrigeration, the numerical heat transfer models for the regenerator and the results of the models that are summarized towards the end of the chapter.

2.1. Working Principle

The MCE refers to the change in temperature that some materials exhibit when they are subjected to a change in magnetic field. It can also be the change in magnetization induced by a temperature change. The magnitude of the MCE can be expressed by either quantifying the temperature change when the magnetic field change occurs in an adiabatic process (ΔT_{ad}) or by quantifying the magnetic entropy change (ΔS_M) when the magnetic field change occurs in an isothermal process. For the thermodynamic analysis of the MCE, the total entropy of the magnetic material is said to be composed of three entropy contributions: the magnetic entropy S_M, the lattice entropy S_{lat} and the electronic entropy S_{el}. The change in total entropy is the sum of the changes in the respective contributions.

$$\Delta S(T, H) = \Delta S_M(T, H) + \Delta S_{lat}(T) + \Delta S_{el}(T) \tag{2.1}$$

Eq. (2.1) suggests that the lattice and electronic entropies are functions of only the temperature of the substance, whereas the magnetic entropy is a function of temperature as well as the magnetic field applied to the substance. When the MCM is subject to an increasing magnetic field, the magnetic order tends to increase as the magnetic domains tend to align in the direction of the magnetic field. Therefore, the magnetic entropy decreases. When this process of magnetization takes place adiabatically, the total entropy remains constant, i.e. $\Delta S(T, H) = 0$. Therefore, a decrease in the magnetic entropy will be followed by an equal increase in the lattice entropy and electronic entropy together, which in turn increases the temperature of the substance. Conversely, during demagnetization, the magnetic entropy increases, resulting in an adiabatic decrease in temperature [3]. The following equations for adiabatic temperature change and isothermal entropy change represent the MCE.

$$\Delta T_{ad}(T, \Delta H) = -\int_{H_1}^{H_2} \left(\frac{T}{C(T, H)}\right)_H \left(\frac{\partial M(T, H)}{\partial T}\right)_H dH \tag{2.2}$$

$$\Delta S_M(T, \Delta H) = \int_{H_1}^{H_2} \left(\frac{\partial M(T, H)}{\partial T}\right)_H dH \tag{2.3}$$

From Eq. (2.2) and Eq. (2.3), it is clear that a change in magnetic field results in an adiabatic change in temperature or an isothermal change in the magnetic entropy depending on the process. Therefore, in order to enhance the MCE, the heat capacity of the substance needs to be low, a large magnetic field needs to be applied, and a magnet with large changes of magnetization with respect to temperature at constant field is to be used.

Magnetic refrigeration and heat pumping make use of the MCE for transferring heat from a colder region to a warmer region. The only difference between the operation of a vapour compression refrigeration cycle

and a magnetic refrigeration cycle is that pressure changes of the refrigerant during the compression and expansion phases of the vapour compression refrigeration cycle, are replaced with the magnetic field changes during the magnetization and demagnetization phases respectively in the magnetic refrigeration cycle. The steps of the magnetic refrigeration cycle (Brayton Cycle) are listed and briefly described below:

1. **Adiabatic magnetization**: The MCM is subject to a magnetic field that is usually provided by a permanent magnet. Since there is no energy transfer to and from the MCM, the process is adiabatic and it results in an adiabatic or isentropic temperature increase of the material.

2. **Isomagnetic enthalpy transfer**: The increased temperature of the substance is now used to provide heat to the heat sink or the hot region. The heat is usually removed by passing a fluid through the material. The magnetic field is held constant to ensure that the magnetic domains do not reabsorb the heat and change the temperature of the substance. Since heat is being transferred from the material, the overall entropy of the material decreases. Once the substance is sufficiently cooled, the MCM is separated from the coolant.

3. **Adiabatic Demagnetization**: The applied magnetic field is now removed from the cooled MCM resulting in an adiabatic decrease in the substance temperature since there is no energy transfer to and from the substance.

4. **Isomagnetic entropy transfer**: The cooled magnetic refrigerant absorbs heat from the heat source or the cold region. Since there is heat transfer to the refrigerant from the cold region, the entropy of the system increases. Therefore, there is entropy transfer to the system.

Fig. 2.1 depicts the steps of the magnetic refrigeration cycle, compared with those of the vapour compression refrigeration cycle.
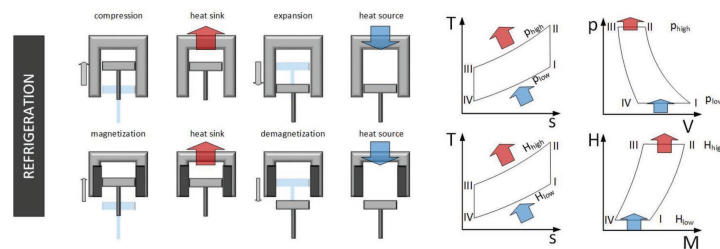
Figure 2.1: Magnetic Refrigeration cycle [2]: Four stages of the magnetic refrigeration cycle are compared with those of the vapour compression refrigeration cycle. The application and removal of pressure in vapour compression refrigeration cycle is substituted by the application and removal of magnetic field in the magnetic refrigeration cycle.

2.2. Materials Used for Magnetocaloric Refrigeration

The MCE makes use of the transition from ferromagnetism to paramagnetism at a certain temperature called the Curie temperature. At the Curie temperature, during the transition, the change in magnetization is maximum, resulting in maximum temperature and entropy change. Hence, if the magnetic refrigeration system were to operate at room temperature, then the material selected as the refrigerant is preferred to have its Curie temperature in the vicinity of the room temperature. MCMs can be classified into two types based on the order of transition from the ferromagnetic to the paramagnetic states: First Order Magnetocaloric Materials (FOMT) and Second Order Magnetocaloric Materials (SOMT). FOMTs go through a discontinuous change in magnetization with a temperature change whereas in SOMTs, the change in magnetization with temperature is continuous. Both FOMTs and SOMTs are being used for magnetic refrigeration and heat pumping. There is no doubt that the main characteristic of MCMs is its adiabatic change in temperature due to a changing magnetic field. However, MCE also involves an isothermal change in entropy. Therefore, this aspect should also be taken into consideration, given that it indicates the cooling capacity of the magnetic refrigerant. Along with these requirements there are other requirements of MCMs. There are certain parameters or criteria, that indicate the potential harm of refrigerants to the environment. One such parameter is called the Total

Equivalent Warming Impact (TEWI), which is concerned with the emissions from the refrigerant that are direct and indirect. Another parameter that is studied in detail is the Life Cycle Climate Performance (LCCP), which is the sum of all the direct and indirect emissions during the lifetime of the refrigerant. Since magnetic refrigerants are to replace the conventional refrigerants used in vapour-compression technology, the values of these parameters for magnetic refrigerants are compared with those of the conventional refrigerants. The values of the parameters for the MCMs are to be less than the conventional materials. Furthermore, although a high MCE is required for magnetic refrigeration, this should not compromise the economy of the operation. Therefore, the material to be selected as MCM should be cost effective. Finally, they should also be mechanically stable during a cycle, should have tunable properties and should be non-toxic [2].

There has been a lot of research with regards to the materials that serve the purpose of magnetocaloric refrigeration. Initially, there were several researchers who studied the MCE using ferrofluids, which consists of ferromagnetic particles in colloidal suspension. However, this method of producing MCE came to a halt due to the low concentration of particles and issues arising from the heat transfer. Brown (1976) [4] then developed a near room temperature magnetic refrigerator, which was a continuously operating device. This device made use of 1 mm thick Gadolinium (Gd) plates, with a water-ethanol solution for regeneration. With the help of regeneration, the device achieved large maximum temperature span of 47 K in 50 cycles. Such a large temperature span is due to the fact that a high magnetic field of 7 T was used by Brown (1976) [4] and there was no cooling or heating load on the cold side and hot side respectively. Since the development of the near room temperature refrigerator, Gd was studied as a potential MCM and it showed good results. However, a significant breakthrough was achieved from the investigation of $Gd_5(Si_2Ge_2)$ as MCM by Pecharsky and Gschneider (1997) [5]. This alloy provided a giant MCE at 270 K that was twice as large as the MCE provided by Gd at 294 K. The largest adiabatic temperature change at 294 K that was produced from this giant MCE is around 15 K for a field of 5 T. The peaks for isothermal entropy change and the adiabatic temperature change for the alloy were not only large, but the widths of the peaks were also lower. Therefore, these changes were concentrated at a very small range of temperature values. The major drawback for using this alloy for refrigeration at room temperature is that the MCE occurs at a temperature range much lower than that of room temperature. This initiated the need to research on other materials that can be used for magnetic refrigeration. A few years after the discovery of the giant MCE of $Gd_5(Si_2Ge_2)$, lanthanide elements including Gd were investigated for magnetocaloric behaviour by Pecharsky and Gschneider (2000) [6]. However, among these elements, Gd was the only pure element to have a Curie temperature that was close to room temperature. The different alloys of rare earth elements that have been investigated for magnetocaloric properties are La-Fe-Si-H, La-Fe-Mn-Si-H, La-Fe-Co-Si and Mn-Fe-P-Si.

Through the development of MCMs and their optimization, there have been several challenges that require attention like reducing the time for heat exchange between heat exchanger and refrigerant, smart thermal control, eradication of losses resulting from hysteresis, among others. One method to counter these problems is size reduction. Therefore, these problems stimulated the need for analyzing MCMs at the micro and nano scales. Miller et al. (2014) [7] investigated the influence of different thin film growth techniques on the magnetocaloric properties of Gd. One of the thin film growth techniques used by Miller et al. (2014) was the growth of 30 nm Gd thin films through sputtering onto substrates that are oxidized by Silicon (Si) and preheated to 450°C. On implementing this technique, Miller et al. (2014) [7], discovered the enhancement, that the pregettering of the sputtering chamber produced on the magnetocaloric properties of Gd. The maximum magnetic entropy increased by 50%, the refrigerant capacity was improved by 30% and the overall saturation magnetization value was enhanced by 35% [8].

2.3. Active Magnetic Regeneration Cycle

Due to its advantages like environment friendliness, compactness and high efficiency, magnetic refrigeration and heat pumping is a potential substitute for vapour compression technology. However, it suffers from the problem of a relatively low temperature span. Therefore, to expand the temperature span of magnetic refrigeration, an Active Magnetic Regeneration (AMR) cycle can be used for magnetic refrigeration [9]. AMR involves the use of porous magnetic material or a packed bed of magnetic particles, that are to behave as a regenerator as well as a refrigerant. The purpose of using packed bed or porous material is to implement large surface areas suitable for efficient heat transfer with a HTF. There are two heat exchangers that are used in the

AMR cycle along with the regenerator. The hot heat exchanger is the heat sink and the cold heat exchanger is the heat source in the refrigeration cycle [10]. Fig. 2.2 represents a schematic of the AMR refrigerator with the heat exchangers.
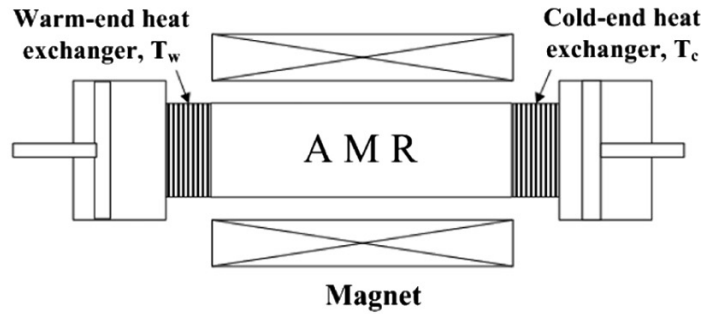
Figure 2.2: Active Magnetic Refrigeration [10]: It depicts the circulation of the HTF between the hot heat exchangers and the cold heat exchangers, as the MCM in the regenerator gets magnetized and demagnetized.

In the AMR refrigeration cycle, the purpose of the HTF is to carry the heat from the cold heat exchanger to the hot heat exchanger through the porous magnetic refrigerant, as it gets magnetized and demagnetized. At the beginning of the operation of an AMR refrigerator, the HTF at the hot and cold ends goes through transient temperature changes, wherein, the HTF in the cold heat exchanger becomes cooler and the HTF in the hot heat exchanger becomes hotter with time. Therefore, the temperature span of the AMR refrigerator increases after each cycle, due to the combined effects of regeneration and MCE. This is the transient phase of operation of the refrigerator, wherein the temperature span increases with each cycle. The number of cycles is a measure of the time span. The transient temperature profiles of the HTF at the cold and hot heat exchangers are shown in Fig. 2.3.
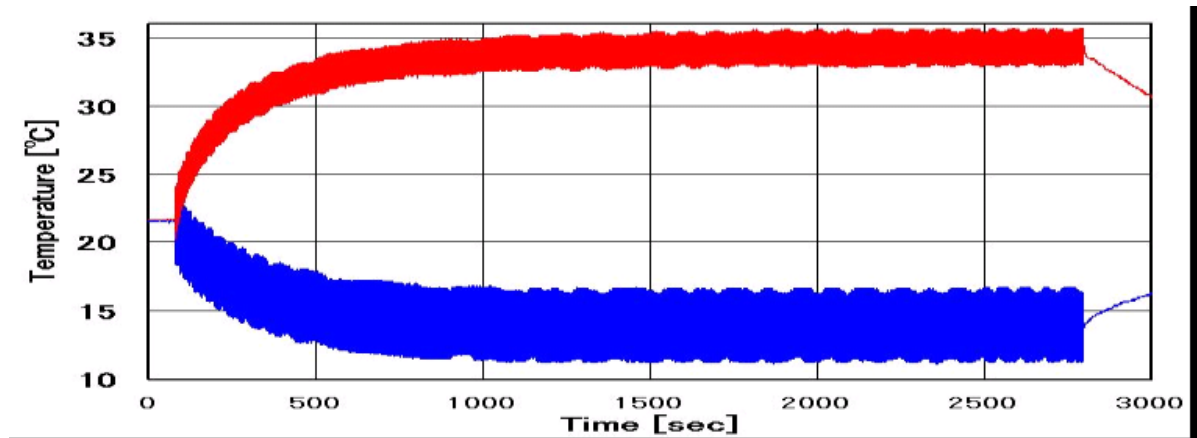
Figure 2.3: Temperature profiles of the HTF at the hot and cold ends [11]: There is a temperature decrease in the HTF at the cold side and a temperature increase of the HTF at the hot side, until there is steady state, wherein the temperature of the HTF at the hot and cold sides no longer changes.

From the temperature plots for the HTF in Fig. 2.3, it can be observed that in the initial phase of operation of the AMR refrigerator, the temperature span increases with time. As the number of cycles increases, the magnitudes of the slopes of the curves decrease, until the curves become nearly horizontal, indicating that thermal equilibrium or steady state has been reached, with a more or less constant temperature span with time.

Eventually, after a certain interval of time of operation of the refrigerator, there will be a point when thermal equilibrium is achieved wherein, the temperature of the HTF at the cold end will no longer decrease and that of the HTF at the hot end will no longer increase with time. This is the steady state condition of the AMR system, where the temperature span between the heat source and the heat sink has been expanded to its

maximum and will remain more or less constant with time [10].

The steady state operation of the cycle starts when the magnetic regenerative refrigerant absorbs the heat from the HTF coming from the hot heat exchanger. As a result the temperature of the solid refrigerant increases. The magnetic field is then applied to the regenerator and its temperature further increases. While the magnetocaloric regenerator is maintained in the magnetic field, the HTF coming from the cold heat exchanger flows through it. As a result, the temperature of the HTF increases and the temperature of the MCM decreases. After the heat exchange, the HTF exits the regenerator to the hot heat exchanger at a temperature close to the maximum temperature of the regenerator after the application of magnetic field, and the cold end of the regenerator cools down to a temperature, close to the temperature of the HTF coming from the cold heat exchanger. The cooled magnetic regenerator is now demagnetized on removal of the magnetic field. The regenerator further cools down. Now, the HTF coming from the hot heat exchanger flows through the regenerator, and its temperature decreases. Naturally, the temperature of the regenerator increases during this heat exchanging process. The HTF exits the regenerator to the cold side at a temperature close to the temperature of the cold end of the cooled regenerator after demagnetization giving the HTF the required refrigeration capacity, and the hot end of the regenerator reaches a temperature close to the temperature of the HTF coming from the hot heat exchanger. This completes one cycle of AMR.

AMR can also be seen with a cascading viewpoint. By cascading, it is meant that the AMR refrigerator can be viewed as one that is composed of a number of pseudo-Carnot magnetic refrigeration cycles. These pseudo cycles can also be referred to as micro-magnetic cycles along the temperature span in a cascaded configuration. The heat transfer fluid of the heat exchangers interacts with these magnetic cycles, to transfer heat from the cold end to the warm end in each such micro-cycle. The cascading view point and the active heat regeneration viewpoints are depicted through the curves in Fig. 2.4 and Fig. 2.5 [9].
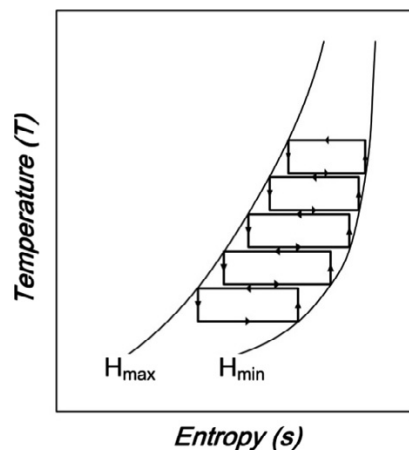
Figure 2.4: Cascading viewpoint [9]: The AMR refrigeration cycle is taken to be composed of multiple pseudo-Carnot magnetic refrigeration cycles.
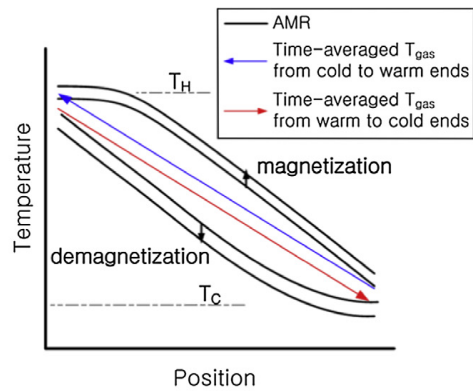
Figure 2.5: Active Heat Regeneration viewpoint [9]: The heat regeneration viewpoint is such that there is a step-wise increase in the HTF temperature at the hot side when the HTF flows from the cold side to the hot side after magnetization, and there is a step-wise decrease in the HTF temperature at the cold side when the HTF flows from the hot side to the cold side after demagnetization.

Since, the AMR cycle makes use of heat exchangers for regeneration and MCE, the requirements for designing an AMR cycle would be similar to those for designing heat exchangers like low pressure drop of the HTF, high heat transfer rate, low thermal conduction in the direction of flow, etc. Along with these requirements there should also be good MCE through affordable material. The structure of the regenerator should be such that it has low porosity and adequate integrity.

There are two types of AMR refrigerators: static and dynamic. In static refrigerators, the source of magnetic field is a superconducting electromagnet. The AMR is kept in a fixed position as the heat transfer traverses through the regenerator between the hot and the cold end heat exchangers. On the contrary, the dynamic AMR involves the mechanical movement of a strong DC magnet or the regenerator to produce the required MCE. In other words, the relative motion between the regenerator and the DC magnet is responsible for the (de)magnetization. After the (de)magnetization, the magnetic regenerator is moved so that the heat transfer fluid passes through its pores from the hot to the cold ends and vice versa [9].

Cycle losses
Practically, an AMR refrigerator undergoes several kinds of losses. Some of these losses are listed below [13]:

1. Dead zones: These are zones that are neither part of the regenerator nor the heat exchangers.

2. Heat leaks into these volumes during its transit between the porous regenerator and the heat exchangers.

3. Unwanted thermal interactions between the regenerator material and the walls of the material.

Taking the cascaded viewpoint of the AMR cycle into consideration, there are chances of mismatch in heat exchange between the adjacent micro-cascaded cycles. This would cause disturbances in these pseudo-Carnot cycles and would lead to irreversibility, affecting the efficiency of the AMR cycle. Therefore, the increase in temperature span of an actual AMR refrigerator would not be very significant [9]. Fig. 2.6 portrays an actual, practical AMR refrigeration cycle indicating the different kinds of energy losses particularly in the form of heat.
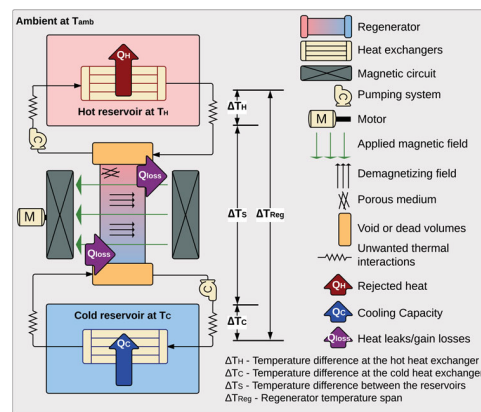
Figure 2.6: Actual AMR Cycle with losses [13]: A complete AMR cycle with the components and the losses that occur during the cycle operation

2.4. Experimental and Theoretical Work on Magnetic Heat Pump Prototypes

The magnetocaloric heat pump prototypes that were initially developed had employed superconducting coils for providing the magnetic field [12]. However, there was a shift from superconducting coils to permanent magnets in the years that followed because of their benefits like relatively low energy cost, little maintenance, absence of electromagnetic perturbations and recyclability.

Trevizoli et al. (2016)

Trevizoli et al. (2016) [13] presented some of the problems that internally develop in an AMR heat pump or regenerator and the compromises that have to be made while eradicating some of these problems. Some of these problems include limited heat transfer area in the regenerator matrix and pressure losses, which hamper the design of AMR heat pumps and refrigerators. Along with the presentation of these problems in AMR devices, Trevizoli et al. (2016) [13] developed some numerical equations to model the flow of the HTF through the regenerator matrix (discussed later in this chapter).

The regenerator geometry that has been used by Trevizoli et al. (2016) [13] is a packed bed. The regenerator is a cylinder that consists of a packed bed of Gd spherical particles with diameters from 0.2 to 1 mm. The length of the regenerator is 100 mm. The diameter of the regenerator varies from 15 to 23.5 mm. The porosity of the packed bed cylinder is 0.36. Trevizoli et al. (2016) [13] give an overview of the existing design alternatives for the components of AMR refrigeration. The authors give several design alternatives for the geometry of the regenerator matrix and its housing, magnetic circuits, the pumping system, and the variation of the magnetic field. The choice of one design alternative will influence the choice of the others. Therefore, there are many challenges that are interlinked between the different components and are difficult to tackle. Trevizoli et al. (2016) [13] suggested the use of Entropy Generation Minimization (EGM) along with Performance Evaluation Criteria (PEC) to address the multiple physical phenomena and the design optimization of AMR systems. The main objective function that is used in this methodology is the entropy generation rate $\dot{S}_{gen}$ (W K^{-1}). The entropy generation rate is analyzed for the different operating conditions and performance parameters of the AMR. The combination of parameters for which the entropy generation rate is minimum is to be chosen. Trevizoli et al. (2016) [13] found that the entropy generation is minimum when there are large amounts of MCM in the regenerator matrix. In other words, the thickness of the casing wall is small. It is also observed that the entropy generation rate decreases with a decrease in mass flow rate of the HTF, irrespective of required cooling capacity.

de Vries and v. d. Meer (2017)

de Vries and v. d. Meer (2017) [16] studied Peltier thermal diodes in combination with micro-channel heat exchangers as a potential solution to the problem of insufficient power density provided by a magnetocaloric device, the main cause of which is the limited convective heat transfer when the HTF flows through the de-

vice. This is done through the reverse engineering of a Peltier module, followed by the detailed analysis of a 2-D single-stage device. This device comprises a thin layer of MCM, that is enveloped by two Peltier modules and the heat exchangers.

In the system, the HTF that is analyzed is water. The Peltier module selected for the analysis is Micropelt MPC-D701. The MCM that is chosen is Gd due to its popularity and the MCE provided by it at room temperature.

de Vries and v. d. Meer (2017) [16] conducted the analysis of the 2-D single-stage system, using some energy equations. Eq. (2.4) and Eq. (2.5) are used to solve the energy balance for the MCM:

$$\rho c \frac{\partial T}{\partial t} + \nabla \cdot (k \nabla T) - \dot{q}_{MCE} = 0 \tag{2.4}$$

$$\dot{q}_{MCE} + T \frac{dB}{dt} \frac{\partial M(B, T)}{\partial T} = 0 \tag{2.5}$$

The results of the modelling of this single stage device are not satisfactory. Although the power density and the frequency of operation are enhanced, there are certain unwanted side effects that occur. One of the major unwanted side effects is the decrease in temperature span of the device, which is due to the heat leakages through the device. To summarize, the performance of a heat pump which operates only on the Peltier effect is higher than that of a heat pump operating on both the Peltier effect and the MCE.

Aprea et al. (2016)

Aprea et al. (2016) [17] designed a novel rotary magnetic refrigerator using permanent magnets, in order to realise the potential of magnetic refrigeration in providing cooling at close to room temperature. Gd is used as the MCM and demineralized water is used as the HTF. The AMR system consists of 8 regenerators, each of them containing a packed bed of Gd spheres. Each regenerator containing a packed bed has a length of 45 mm, a height of 20 mm and a width of 35 mm. The porosity in each of the packed beds is around 0.365. Each sphere has a diameter of 400-500 μm. The total mass of Gd in each regenerator is 150 g, making it a total Gd mass of 1.2 kg for the regenerator system. The regenerators are arranged in a circular manner and are fixed onto an aluminium ring with a spacing of 45° between each regenerator. The magnetic field provided by the permanent magnet is 1.25 T. The HTF is pumped through the regenerators with the help of a rotary vane pump. The hot reservoir for the system is a coaxial heat exchanger, and an electric heater is used as a cold reservoir. A brushless DC motor is used to drive the magnetic refrigerator by rotating the magnet at a variable speed ranging from 0.1-1 Hz. The results of the design suggest that the performance of the magnetic refrigerator was quite low, mainly because of the thermal losses. At no load, the maximum temperature span achieved by the refrigerator is 11.3°C. For a thermal load of 57 W on the cold side, the temperature span reached a value of 9.15°C. For a hot reservoir temperature of 22°C and a cooling capacity of 163 W, the COP reached a maximum value of 1.8.

Huang et al. (2019)

Huang et al. (2019) [18] developed a prototype for an AMR refrigerator known as the FAME cooler, in order to study the performance of different MCMs in an actual environment. The magnetic field is periodic in nature, having a frequency of 3 Hz. The HTF that is used for this prototype is water. The regenerator system consists of 7 regenerators that are arranged in a circular manner with a spacing of 51.42° between each regenerator. Each regenerator consists of a packed bed of Gd spheres. The Gd spheres in each of the packed beds have a diameter of 400-800 μm. Each regenerator has a length of 60 mm, a width of 45 mm and a height of 13 mm. The porosity of each of the packed beds is 0.36. There are two heat exchangers for the hot and the cold end respectively. For the cold side heat exchanger, a cartridge heater is used as the insert. This heat exchanger is insulated with polystyrene foam. The purpose of the hot end heat exchanger with a thermostatic bath is to control the starting temperature and the hot end temperature of the HTF. The flow of the HTF through the AMR refrigerator is produced by a DC diaphragm pump. The design of the AMR refrigerator is flexible. It allows for the modification of the regenerator, by changing the number of beds or simply replacing the MCM in the regenerator beds. For a magnetic field of 0.875 T, it is found that the maximum value of the change in entropy is 2.97 $J \, kg^{-1} \, K^{-1}$, and the adiabatic change in temperature reached its peak of 3.54 K. With the hot end temperature at 295 K, the temperature span reached a maximum of 11.6 K, at no thermal load. The zero-

span cooling power reached a maximum of 162.4 W and the cooling COP is found to be 1.59. The maximum value of the COP is 1.85 for a zero-span cooling power of 102.4 W.

2.5. Application of magnetocaloric devices

There have been various devices to which the MCE has been applied for better performance. Some of the important applications have been discussed below.

Johra et al. (2019)

Johra et al. (2019) [20] developed and tested a prototype of a magnetocaloric heat pump with AMR, under the project ENOVHEAT. This heat pump is developed for use in indoor environments, particularly in residential buildings. For enhancing the performance of the heat pump, the thermal mass of the building is used as a strategy in this project to store thermal energy so that the heat pump works at full capacity (and therefore with a higher COP) every time it has to work. The authors had previously researched on the integration of the heat pump in dwellings and they extend this research in this paper by incorporating a heat storage control strategy, given that the residential building has energy flexibility potential. The heat pump that is used for this research is rotary magnetic heat pump having AMR. The regenerator system consists of a total of 13 regenerators. These regenerators are basically cassettes having a trapezoidal shape. Each such trapezoidal regenerator consists of a packed bed of Gd spheres. Each Gd sphere has a diameter of 450 μm. Each regenerator has a length of 59 mm, a height of 17 mm and an average width of 61.43 mm. The packed bed in each regenerator has a porosity of around 0.534.

Torregrosa-Jaime et al. (2013)

Torregrosa-Jaime et al. (2013) [14] presented the initial steps for designing a magnetocaloric air-conditioning system for an electric minibus. This system consists of two reversible magnetocaloric heat pumps, each one operating at the front and back of the minibus respectively. For aiding the design of the system, Torregrosa-Jaime et al. (2013) [14] developed a dynamic model for the hydraulic loops, the cabin and the hot and cold-side heat exchangers to be integrated with the magnetocaloric units, since the minibus system would function in dynamic conditions that are influenced by the heat load in the cabin. This modelling was done under the European ICE project to develop magnetocaloric heat pump technology to be used in Fully Electric Vehicles (FEV). Fig. 2.7 represents the magnetic air conditioning system of a minibus.
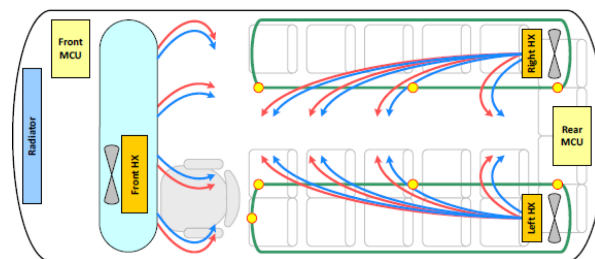
Figure 2.7: Magnetic Air conditioning system in a minibus: topview. MCU = Magnetocaloric units, HX = Heat exchanger [14]

Fig. 2.7 shows two Magnetocaloric Units (MCU), or the magnetic heat pumps, at the front near the driver's seat and at the back for the passenger compartment. There are three heat exchangers that are installed in the minibus: one at the front of the bus in the driver zone and two in the passenger cabins at the rear of the bus. The HTF that is used for the transferring the thermal power through the system is a 50% mixture of water and glycol. The HTF flows between the MCUs and the heat exchangers.

During the design of the MCU, high importance is given to the regenerator. The regenerator consists of different MCMs, each having a different Curie temperature. The materials are chosen such that the Curie temperatures are distributed between the minimum and maximum temperatures of the hot and cold sides, thereby providing the maximum possible MCE for an increased temperature span. The regenerator consists of micro-channels for the HTF to flow through it, and for the heat exchange to take place between the HTF and the regenerator matrix. The entry and exit of the HTF to and from the matrix is optimized to prevent hydraulic losses. There is a packing of insulation around the regenerator matrix to provide support to the

regenerator [14].

The MCE of the regenerator is enhanced stage-wise, i.e., at the end of each stage, when the Curie temperature is reached, a MCM with a higher Curie temperature is added to the regenerator matrix to enhance the temperature span in the next stage of operation, thereby increasing the overall MCE of the system. There are multiple stages like this in the MCUs of this project, since the operational temperatures during the summer and winter vary a lot. Therefore, by increasing the MCE stage-wise by using several MCMs to bridge the temperature span between the hot and cold reservoirs, the temperature span of the regenerator is also increased. Enhancing the frequency of the cycle is a cheaper way to increase the temperature span of the device, which allows to reduce the weight of the permanent magnets that are used to provide the magnetic field. For adiabatic (de)magnetization, the temperature span that is achieved with the present technology is 40 K with a magnetic field of less than 1 T [14].

Torregrosa-Jaime et al. (2013) [14] also pointed out that the thermal power of the magnetic heat pump can be enhanced by strengthening the magnetic field, increasing the frequency of the cycle, and improving the convective heat transfer. The convective heat transfer is usually enhanced by decreasing the height of the micro-channels of the regenerator, thereby decreasing the surface area per micro-channel and increasing the surface area per unit volume of the regenerator matrix. However, increasing the frequency of the cycle, also leads to an increase in the pressure drop through the regenerator, thereby increasing the workload of the circulation pumps. Also, if the height of the micro-channel is reduced, hydraulic losses tend to increase. Therefore, the most cost effective method to increase the thermal power, is to increase the strength of the magnetic field. Materials with improved magnetocaloric properties can also be an option for improving the thermal power of the MCUs. The thermal power that is obtained with the current state-of-the-art technology can reach a maximum of 2000 W, depending on the temperature span of the regenerator at steady state, as well as on the mass of the MCM. The COP of the magnetic heat pump prototype that is obtained is 2.24, which is the highest achieved COP.

Torregrosa-Jaime et al. (2014)
Torregrosa-Jaime et al. (2014) [15] further developed the design of the magnetocaloric air conditioning system for an electric minibus. This included describing the dynamic models to assist the system design and analyzing the operating conditions of the MCU in detail.

The hydraulic loops and the heat exchangers represent important parts of the integrated design of the system, as they ensure the heat transfer through the magnetic heat pumps. The hydraulic loops are divided into two parts: the external loop and the internal loop. The external loop comprises the radiator, which interacts thermally with the external surroundings. The internal loop consists of the air conditioners that heat or cool the air inside the minibus cabin, depending on whether it is winter or summer. Torregrosa-Jaime et al. (2014) [15] made an energy balance for each of the heat exchangers, taking into account the thermal and inertial losses, during the flow of air and the HTF through the ducting. The effectiveness-NTU method is used to make the energy balance. The effectiveness ψ, is defined as the ratio of the actual heat transfer rate to the maximum possible heat transfer rate. It is influenced by the properties of the heat exchanger and the temperature and mass flow rate of the the HTF and air. The formula for the effectiveness is given by Eq. (2.6).

$$\psi = \frac{\dot{Q}}{\dot{Q}_{max}} \tag{2.6}$$

In Eq. (2.6), the maximum heat transfer rate is associated with the fluid with minimum specific heat capacity. It is given by Eq. (2.7).

$$\dot{Q}_{max} = \dot{m} \cdot c_{p,min} \cdot (T_{H,in} - T_{C,in}) \tag{2.7}$$

Where: $T_{H,in}$ is the temperature of the hot fluid at the heat exchanger inlet and $T_{C,in}$ is the temperature of the cold fluid at the heat exchanger inlet.

Torregrosa-Jaime et al. (2014) [15] considered the fluid with minimum specific heat capacity to be air. Therefore:

$$\dot{Q}_{max} = \dot{m}_{air} \cdot c_{p,air} \cdot (T_{H,in} - T_{C,in}) \tag{2.8}$$

The Number of Transfer Units (NTU) of a heat exchanger, is related to the overall heat transfer coefficient

through Eq. (2.9).

$$NTU = \frac{UA}{c_{p,\,\text{air}} \cdot \dot{m}_{air}} \tag{2.9}$$

The ratio of heat capacities C^* is obtained through Eq. (2.10).

$$C^* = \frac{\dot{C}_{\text{min}}}{\dot{C}_{\text{max}}} = \frac{c_{p,\,\text{air}} \cdot \dot{m}_{\text{air}}}{c_{p,f} \cdot \dot{m}_f} \tag{2.10}$$

Depending on the type of heat exchanger and the type of fluid flow, there are different relations between the effectiveness, the NTU and the ratio of heat capacities. The type of heat exchangers that are used are cross flow, mini-channel heat exchangers, where there is no mixing of the two fluids. Therefore, the effectiveness is calculated using Eq. (2.11).

$$\psi = 1 - \exp\left\{ \frac{NTU^{0.22} \cdot \left[\exp\left(-C^* \cdot NTU^{0.78} \right) - 1 \right]}{C^*} \right\} \tag{2.11}$$

For the regenerator matrix for AMR, the materials that are used by Torregrosa-Jaime et al. (2014) [15] are Gd-based alloys, since the properties of these alloys have been studied in detail in other literature pertaining to magnetocaloric refrigeration, thereby resulting in more accurate results from simulation. The regenerator matrix comprises of plates that are stacked and placed in parallel with the magnetic field. The thickness of these plates varies between 0.4 and 0.6 mm. The stacks of plates are spaced from each other by a small gap ranging from 0.1 to 0.2 mm, to facilitate the smooth transport of the HTF through the matrix between the hot and cold ends. This small gap is also known as the channel width. Table 2.1 summarizes the design parameters for the AMR matrix.

Table 2.1: AMR parameters [15]

Property	Value
Width of MCM plates (mm)	15
Thickness of MCM plates (mm)	0.4 - 0.6
Mass of MCM in one AMR (g)	4550
Channel width (mm)	0.1 - 0.2
Frequency of one cycle (Hz)	4

It is important to obtain the thermal load inside the minibus during the summer and winter, in order to deduce the required cooling and heating power of the system and the corresponding working temperatures. This is done in order to obtain the Curie temperature and the mass of the MCM for the regenerator, to carry out the first steps of designing the system. To determine the thermal load, the cabin was simulated by Torregrosa-Jaime et al. (2014) [15]. For each of the two seasons, two working modes have been analysed: pre-conditioning mode at the time of start-up and the steady-state mode when the minibus is occupied by the average number of people. The results of the cabin model simulations suggest that the thermal load is maximum during the pre-conditioning mode while operating in the winter season. Therefore, the heat pump is sized to satisfy the maximum load, with each of the two heat pumps operating at half of the maximum load. The model developed by Torregrosa-Jaime et al. (2014) [15] showed that during the summer, the temperature span that is required for the magnetic heat pumps is 37 K for a maximum thermal load of 1.6 kW during the steady state operation, and during the winter, the required temperature span for the heat pumps is 40 K, for a maximum thermal load of 3.39 kW during the pre-conditioning warm-up mode.

Table 2.2 shows an overview of the work carried out by the above authors.

Table 2.2: Overview of work on Magnetic Heat Pump Prototypes

Ref.	Model	Material	$\dot{Q}_{cool,load}$ (W)	COP	Field (T)	F_{cycle} (Hz)	ΔT_{span} (K)
[13]	Thermodynamic, Mathematical	Gd	15	-	1.45	2	20
[15]	Thermodynamic, Integrated	Gd alloy	1600	2.24	<1	4	40
[17]	Thermal, Experimental	Gd	163	1.8	1.25	1	11.3
[18]	Thermal, Experimental	Gd	102.4	1.85	0.875	3	11.6

The summary of the different geometries of the regenerator used by the authors and their corresponding dimensions are shown in Table 2.3.

Table 2.3: Overview of Regenerator Geometries with Dimensions

Ref.	Geometry	Length (mm)	Width (mm)	Height (mm)	Diameter (mm)	Porosity	Particle Diameter (μm)	No. of Regenerators
[13]	Packed bed	100	-	-	15 - 23.5	0.36	200 - 1000	1
[15]	Flat plate	15	15	0.4 - 0.6	-	-	-	10
[17]	Packed bed	45	35	20	-	0.365	400 - 500	8
[18]	Packed bed	60	45	13	-	0.36	400 - 800	7
[20]	Packed bed	59	61.43	17	-	0.534	450	13

2.6. Numerical models for Magnetocaloric Devices

Numerical Models for AMR refrigeration have undergone developments through the past three decades. The initial models that were developed were simple, and they were sometimes referred to as the steady state models. These models were concerned with overall energy and entropy balances for the AMR system, and they did not take the heat transfer processes in the regenerator into account. Among the other models being developed, there were those based on transient responses of the system, wherein, the details of the local heat transfer between the HTF and the regenerator were included. These transient models are therefore, more accurate in representing the physics of the AMR refrigerator.

Trevizoli et al. (2016):
Trevizoli et al. (2016) [13], address some of the challenges encountered in the various prototypes of magnetic heat pumps and AMR refrigeration devices. To numerically address some of these challenges, an energy balance is made using the first law of thermodynamics for the AMR as stated in Eq. (2.12).

$$\dot{Q}_H = \dot{Q}_C + \dot{W}_{mag} + \dot{W}_{pump} \tag{2.12}$$

$\dot{Q}_H$ is the heat rejected to the hot end or the heat sink, thereby representing the heat pumping capacity, and $\dot{Q}_C$ is the heat drawn from the cold end or the heat source, representing the cooling or refrigeration capacity. $\dot{W}_{pump}$ is the power given to the pump to counter the pressure drop due to the flow of the HTF through the regenerator matrix, and $\dot{W}_{mag}$ is the magnetic work due to the application of the magnetic field. Eq. (2.12) represents the ideal case. A more realistic case would include some of the heat losses that occur in the system. Therefore, Trevizoli et al. (2016) [13] included the different heat losses in a term called $\dot{L}$ to Eq. (2.12). Therefore, the inclusion of this term leads to Eq. (2.13).

$$\dot{Q}_H = \left(\dot{Q}_C - \dot{L}\right) + \dot{W}_{mag} + \dot{W}_{pump} \tag{2.13}$$

The different losses in AMR refrigerator that were briefly discussed in the previous chapter are included in the $\dot{L}$ term in Eq. (2.13), and were studied in detail by Trevizoli et al. (2016) [13]. The losses are studied to identify the limitations on the AMR refrigeration devices and areas that need improvement. In order to analyse the losses in detail, momentum and energy equations were developed for the solid phase as well as the liquid phase in the regenerator. Eq. (2.14) is an one dimensional momentum equation.

$$\frac{\rho_f}{\varepsilon}\left(\frac{\partial u}{\partial t}\right) + \frac{\partial P}{\partial x} + \frac{\mu_f}{K}u + \frac{E\rho_f}{K^{1/2}}|u|u = 0 \tag{2.14}$$

Eq. (2.14) is the momentum equation for the fluid phase (HTF). The first term on the left hand side represents the inertial force on a macroscopic scale. The second term on the left hand side represents the pressure gradient of the HTF flowing through the pores, the third term is the shear stress at the microscopic level, and the fourth term represents the microscopic Ergun inertial force. The Ergun constant E and the permeability of porous media K are influenced by the geometry of the regenerator matrix. Eq. (2.15) is the fluid phase energy equation.

$$\varepsilon\frac{\partial T_f}{\partial t} + \frac{U\sigma}{\rho_f c_{p,f}}\left(T_f - T_s\right) + u\frac{\partial T_f}{\partial x} - \varepsilon\left(\frac{k_{f,eff}}{\rho_f c_{p,f}} + D\right) \times \frac{\partial^2 T_f}{\partial x^2} - \frac{1}{\rho_f c_{p,f}}\left|\frac{\partial P}{\partial x}u\right| - \dot{T}_{loss} = 0 \tag{2.15}$$

The first term on the left side of Eq. (2.15) represents the thermal capacity due to inertial effects, the second term and the third term represent the convective heat transfer between the HTF and the solid regenerator matrix, the fourth term represents the conductive heat transfer of the HTF coming in contact with the matrix, the fifth term represents dissipation due to viscosity and the last term is the heat loss term that is concerned with parasitic heat leaks or gains through the matrix housing and the surroundings. The energy equation for the solid phase representing the solid regenerator matrix is given by Eq. (2.16).

$$(1 - \varepsilon)\frac{\partial T_s}{\partial t} + \frac{U\sigma}{\rho_s c_s}\left(T_s - T_f\right) - (1 - \varepsilon)\frac{k_{s,eff}}{\rho_s c_s}\frac{\partial^2 T_s}{\partial x^2} + \frac{\partial T_{MCE}}{\partial t} = 0 \tag{2.16}$$

The terms in Eq. (2.16) have the same meaning as that of the terms in Eq. (2.15). The major difference between both the energy equations is that, in Eq. (2.16) for the solid phase, there is no term for convection and viscous dissipation, due to the fact that the solid matrix is rigid. Another remark that can be made with regards to Eq. (2.16) is that, there is an MCE term, which clearly indicates that the solid matrix is made of MCM

with a certain porosity.

Nielsen (2010)

A simple approach towards the modelling of AMR systems is the 2-dimensional model. The 2-dimensional models help in determining the transverse thermal gradient with respect to the direction of flow of the HTF. The 3-dimensional approach is also being employed for AMR modelling. In a 3-dimensional model, the porous or packed bed magnetocaloric regenerator is divided into cells. By imposing certain boundary conditions in each cell, the heat transfer and fluid flow problems are solved. This 2-dimensional model is developed by Nielson (2010) [19].

A 2-dimensional numeric model for a parallel-plate AMR refrigerator is developed, simulating half a plate of MCM and half of a fluid channel. Through certain assumptions, the boundary conditions were thought to be either thermally coupled inner boundaries or adiabatic. Therefore, Eq. (2.17) and Eq. (2.18) are the governing equations that were developed for the thermal system.

$$\frac{\partial T_f}{\partial t} - \frac{k_f}{\rho_f c_f}\left(\frac{\partial^2 T_f}{\partial x^2} + \frac{\partial^2 T_f}{\partial y^2}\right) + (\mathbf{u}\cdot\nabla)T_f = 0 \tag{2.17}$$

$$\frac{\partial T_s}{\partial t} - \frac{k_s}{\rho_s c_s}\left(\frac{\partial^2 T_s}{\partial x^2} + \frac{\partial^2 T_s}{\partial y^2}\right) = 0 \tag{2.18}$$

The subscripts s and f represent the corresponding properties of the solid regenerator and the HTF. In Eq. (2.17), there are three terms in the equation. The first term on the left-hand side of the equation is the transient term as there is time-dependence for the temperature. The second term on the left-hand side of the equation is the diffusive term and the third term is the convective term, as there is a velocity vector $\mathbf{u}$ of the flowing HTF. In Eq. (2.18), the convective term is absent owing to the presence of only conduction in the solid material.

It is observed that Eq. (2.17) and Eq. (2.18) are similar to the solid and fluid phase energy equations (Eq. (2.15) and Eq. (2.16)) developed by Trevizoli et al. (2016) [13]. The main difference between these sets of equations is that Nielson (2010) [19] has developed Eq. (2.17) and Eq. (2.18) for a particular plate and fluid channel, whereas Eq. (2.15) and Eq. (2.16) developed by Trevizoli et al. (2016) [13] covers the entire regenerator matrix, taking into account the porosity, along with the conductive and convective heat transfer.

Eq. (2.17) and Eq. (2.18) can be modified by placing a source term, to represent the heat given out or generated by the regenerator during the magnetization or demagnetization processes. This leads to Eq. (2.4) developed by de Vries and v. d. Meer (2017) [16], which is the energy balance for the MCM in the regenerator.

Johra et al. (2019)

Numerical models have been developed for the magnetic heat pump as part of the study by Johra et al. (2019) [20]. Eq. (2.19) and Eq. (2.20) are the equations that are used to develop the numerical models.

$$\frac{\partial}{\partial x}\left(k_{disp}A_c\frac{\partial T_f}{\partial x}\right) - \dot{m}_f c_{p,f}\frac{\partial T_f}{\partial x} - \frac{Nuk_f}{d_h}\sigma A_c\left(T_f - T_s\right) + \left|\frac{\partial P}{\partial x}\frac{\dot{m}_f}{\rho_f}\right| \quad - A_c\varepsilon\rho_f c_{p,f}\frac{\partial T_f}{\partial t} = 0 \tag{2.19}$$

$$\frac{\partial}{\partial x}\left(k_{stat}A_c\frac{\partial T_s}{\partial x}\right) + \frac{Nuk_f}{d_h}\sigma A_c\left(T_f - T_s\right) \quad - A_c(1-\varepsilon)\rho_s \times \left[c_{p,H}\frac{\partial T_s}{\partial t} + T_s\left(\frac{\partial s_s}{\partial H}\right)_{T_s}\frac{\partial H}{\partial t}\right] = 0 \tag{2.20}$$

Eq. (2.19) represents the numerical energy balance for the HTF and Eq. (2.20) represents that for the solid regenerator matrix. Eq. (2.19) and Eq. (2.20) were solved by Johra et al. (2019) [20] applying the finite volume method with the help of MATLAB. The results of the model are comparable with that of experimental data.

Eq. (2.19) and Eq. (2.20) are also comparable to Eq. (2.15) and Eq. (2.16) developed by Trevizoli et al. (2016) [13]. Both sets of equations for the solid and fluid energy balance contain similar terms for conduction, convection and the heat transfer due to the MCE.

The residential building under study by Johra et al. (2019) [20] is a single Danish family house. The heating system in the house consists of a vertical borehole ground source heat exchanger and a hydronic radiant

under-floor heating system. The ground source heat exchanger acts as a heat source and the hydronic heating system acts as a heat sink. The main purpose of this heating system is to enhance the performance of the heat pump. The use of vertical boreholes as the heat source and the under-floor heating system as the heat sink, decreases the required temperature span of the heat pump, thereby facilitating the design of the magnetocaloric heat pump. A thermodynamic numerical model is created for this building heating system, with the help of MATLAB and SIMULINK. For this purpose, an energy balance equation similar to Eq. (2.17) is solved. Apart from that, an effectiveness-NTU method is used, similar to that used by Torregrosa-Jaime et al. (2014) [15], but with a different equation for the effectiveness-NTU relation. A resistance network analogy is used to calculate the overall heat transfer coefficient through the various components in the system, like the piping and heat exchangers. Eq. (2.21) is used to obtain the overall heat transfer coefficient for the hydronic heating system, given that it is modelled as a horizontal heat exchanger.

$$U = \frac{1}{R_f + R_{pipe} + R_{hex}} \tag{2.21}$$

In the right-hand side of Eq. (2.21), R_f stands for the thermal resistance of the fluid, R_{pipe} stands for the thermal resistance of the pipe and R_{hex} stands for the thermal resistance of interaction between the tubes of the heat exchanger. The pressure drop due to the friction of the fluid flowing through the pipes is determined using Eq. (2.22), which is the Darcy-Weisbach equation.

$$\Delta P = \frac{\rho \times u^2}{2} \left(\frac{f \times L}{d_h} + K_f \right) \tag{2.22}$$

Risser et al. (2013)

A numerical model was developed by Risser et al. (2013) [21] for optimizing the design of magnetic refrigerators having AMR. The numerical model is developed in such a way that it targets different design strategies for enhancing different parameters like power density, temperature span, energy efficiency, COP and the likes. The coolant channels are positioned parallel to the magnetic flux. Risser et al. (2013) [21] developed an one dimensional equation for the energy balance of the HTF flowing through the coolant channels, given by Eq. (2.23).

$$\rho_f \cdot c_{p,f} \cdot \left(\frac{\partial T_f}{\partial t} + u \cdot \frac{\partial T_f}{\partial x} \right) - k_f \cdot \frac{\partial^2 T_f}{\partial x^2} - \dot{q}_{visco} - \dot{q}_{HT} = 0 \tag{2.23}$$

The first term of the left hand side of Eq. (2.23) contains the unsteady term and the convection term due to the fluid flow through the channels. The second term is the heat transfer due to thermal conduction between the HTF and the solid refrigerant it is in contact with, the third term represents the viscous dissipation of the fluid heat, and the final term represents the overall heat transfer between the HTF and the MCM.

A similar one dimensional equation for the heat transfer to the solid MCM is given in Eq. (2.24):

$$\rho_s \cdot c_{p,s} \cdot \frac{\partial T_s}{\partial t} - k_s \cdot \frac{\partial^2 T_s}{\partial x^2} - \dot{q}_{MCE} - \dot{q}_{leak} + \dot{q}_{HT} = 0 \tag{2.24}$$

Similar to Eq. (2.23), Eq. (2.24) also has an unsteady term. It is observed that in Eq. (2.24), there is a term $\dot{q}_{leak}$ which represents the heat leaks from the AMR to the HTF or the surroundings, mainly due to the improper insulation around the AMR. It is also noticed that Eq. (2.23) and Eq. (2.24) have a common term on their right hand sides which is $\dot{q}_{HT}$. The only difference is the sign of the term. The term has opposite signs in the two energy equations, which indicates that when heat is added to the HTF, it is removed from the MCM and vice-versa.

Eq. (2.23) and Eq. (2.24) for the solid and fluid energy balance can be compared to the energy balance equations (Eq. (2.17) and Eq. (2.18)) developed by Nielson (2010) [19]. The only difference is that, in Eq. (2.23) and Eq. (2.24), the viscous heat losses and the heat leaks into the regenerator matrix through the insulation have been considered.

There are two types of magnetic field in the magnetic refrigerator being modelled: The internal and external magnetic field. The internal magnetic field is that which is generated in the material due to the alignment of the magnetic dipoles in the direction of the applied field. This is the cause of the MCE of the MCM to take

place. In particular, it is responsible for the adiabatic temperature of the MCM. Risser et al. (2013) [21] developed this connection between the thermal models (Eq. (2.24) and Eq. (2.26)) and the magnetic model through a relation between the magnetocaloric heat and the adiabatic temperature change, given by Eq. (2.25).

$$\dot{q}_{MCE} = \frac{\partial T_{ad}(T_s, H_{in})}{\partial H_{in}} \cdot \frac{\partial H_{in}}{\partial t} \cdot \rho_s \cdot c_{p,s}(T_s, H_{in}) \tag{2.25}$$

There is a term in Eq. (2.20) ($(\frac{\partial s_s}{\partial H})_{T_s} \frac{\partial H}{\partial t}$) used by Johra et al. (2019) [20] which is similar to the right hand side of Eq. (2.25). Both these terms represent the heat transfer due to the MCE $\dot{q}_{MCE}$. The difference between the two terms is that, the term in Eq. (2.20) represents the isothermal entropy change due to the magnetic field, whereas the term in Eq. (2.25) represents the adiabatic temperature change due to the magnetic field.

The external magnetic field is the field that is caused by the magnetic induction from the permanent magnet used to provide the magnetic field. There is also the demagnetizing field that makes a contribution to the magnetic field. Using these concepts of external magnetic and demagnetizing fields, Risser et al. (2013) [21] developed another connection between the thermal and magnetic numerical models. This relation is given by Eq. (2.26).

$$B = \mu_0 \cdot (H_e + M(T_s, H_{in}) + H_d) \tag{2.26}$$

The connection that is established through Eq. (2.26) comes from the magnetization M of the material, since it depends on the temperature of the material and the internal magnetic field. Therefore, the magnetization changes due to a change in the temperature, and once the temperature of the MCM is close to the Curie temperature, the magnetization changes from ferro to paramagnetism, thereby providing the MCE. The internally generated magnetic field intensity is related to the external magnetic field intensity and the demagnetizing magnetic field intensity through Eq. (2.27).

$$H_{in} = H_e + H_d \tag{2.27}$$

Risser et al. (2013) [21] solved the one dimensional heat equations for the solid MCM and HTF, and the magnetic models using Gauss-Seidel iterative procedure. The solution of these equations in the models, is followed by the calibration of the models. One of the parameters that is used to calibrate the model is I_{vol}, which is the ratio of the volume of HTF that is transported through the regenerator during half a cycle to the volume of the HTF contained between the MCM. The ratio is also expressed as a ratio of lengths through Eq. (2.28).

$$I_{vol} = \frac{1}{L_x} \cdot \int_0^{\phi/2} u(t) \cdot dt \tag{2.28}$$

Where, L_x is the length of the AMR along the x direction and ϕ is the duration of one AMR cycle.

The total temperature span of the AMR device is calculated by integrating the temperatures of the MCM during heating and cooling at the outlet of the channel over time, taking the difference between them and then dividing by the total cycle time as given in Eq. (2.29).

$$\Delta T_{span} = \frac{1}{\phi} \cdot \left(\int_\phi T_{H,out}(t) \cdot dt - \int_\phi T_{C,out}(t) \cdot dt \right) \tag{2.29}$$

The relative deviation of the temperature span is computed on comparison with the simulated and experimental values. Eq. (2.30) is the formula that can be used to calculate the relative deviation in the temperature span.

$$RD = \frac{\Delta T_{span,simu} - \Delta T_{span,exp}}{\Delta T_{span,exp}} \tag{2.30}$$

The model developed by Risser et al. (2013) [21], is useful in analyzing the behaviour of AMR magnetocaloric devices. If the behaviour of the device is determined, it allows for the optimization of the driving parameters and size of the components in the device. In this way, the efficiency, COP, power density and temperature span can be enhanced. The sizing of the device can then be done for specific applications of magnetocaloric refrigeration.

Kamran et al. (2016)
A numerical model is developed by Kamran et al. (2016) [22] for AMR refrigerators or heat pumps. The type

of regenerator that is used is a micro-channel regenerator. The micro-channels are circular in shape, made of Gd, with a diameter between 0.7 and 2 mm. Water is the chosen HTF. The flow of the HTF through the regenerator is driven by two piston-cylinder displacers. These displacers operate at different mass flow rate, that vary during the operation of the cycle. Fig. 2.8 shows a schematic of the system.
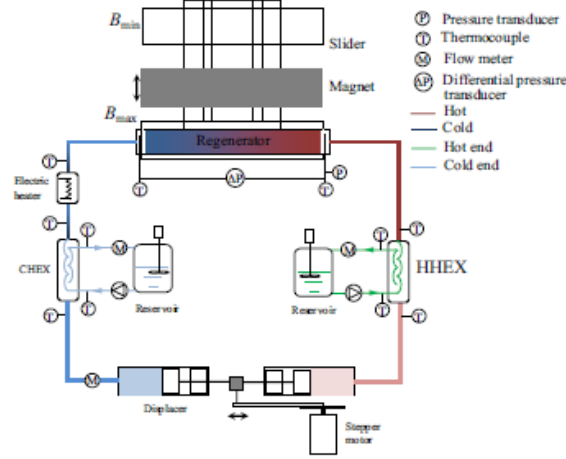
Figure 2.8: Schematic of AMR refrigerator [22]: The HTF from the hot heat exchanger flows into the regenerator for a heat exchange process, wherein, the regenerator becomes hotter and the HTF becomes cooler as it exits the regenerator to the cold heat exchanger. The regenerator is demagnetized in order to be heated up further. Then, the HTF from the cold end heat exchanger flows into the regenerator, gains heat from it, and flows to the hot end. The regenerator cools down during this process and is further cooled down through magnetization. The HTF from the hot end, then flows through the regenerator. In the process, the HTF cools down and exits the regenerator to the cold heat exchanger

The regenerator loop of the refrigerator contains the micro-channel regenerator, the heat exchangers at the hot and cold sides, and the displacer. Like several other authors, Kamran et al. (2016) [22] modelled the heat transfer in the solid MCM and the HTF, taking into consideration, the conduction in the solid and HTF, and the convection due to the HTF as it gets transported through the micro-channels. Eq. (2.31) to Eq. (2.34) are the equations for mass, momentum and energy conservation for modelling the heat transfer between the HTF and the solid regenerator.

$$\nabla \cdot u = 0 \tag{2.31}$$

$$\rho_f \left(\frac{\partial u}{\partial t} + u \cdot \nabla u \right) + \nabla P - \mu_f \left(\nabla^2 u \right) = 0 \tag{2.32}$$

$$\frac{\partial T_f}{\partial t} + u \cdot \nabla T_f - \alpha_f \left(\nabla^2 T_f \right) = 0 \tag{2.33}$$

$$\frac{\partial T_s}{\partial t} - \alpha_s \left(\nabla^2 T_s \right) = 0 \tag{2.34}$$

Eq. (2.31) to Eq. (2.34) are solved subject to certain boundary conditions depending on the design of the micro-channels. The MCE is then implemented in the model using the method of discretization. Eq. (2.35) shows this discretization.

$$T_s \left(x, y, z, t^{n+1} \right) = T_s \left(x, y, z, t^n \right) \pm \Delta T_{ad} \left[T_s \left(x, y, z, t^n \right), \Delta B \right] \tag{2.35}$$

In Eq. (2.35), the t^n is the nth time step in the discretization. The heat transfer in the heat exchangers is modelled using the effectiveness-NTU method, similar to Johra et al. (2019) [20]. The difference lies in the equation for effectiveness used by Kamran et al. (2016) [22]. The type of heat exchangers in this case is double-pipe with the type of flow being counter-flow. Therefore the relation used by Kamran et al. (2016) [22] is given in Eq. (2.36).

$$\psi = \frac{1 - \exp[-NTU(1 - C^*)]}{1 - C^* \exp[-NTU(1 - C^*)]} \tag{2.36}$$

The overall heat transfer coefficient for the heat exchangers is calculated using Eq. (2.37).

$$U = \left[\frac{1}{h_f} + \frac{d_{i,hex}}{2k_{hex}} \ln\left(\frac{d_{o,hex}}{d_{i,hex}}\right) + \frac{d_{i,hex}}{h_{hex,f} d_{o,hex}} \right]^{-1} \tag{2.37}$$

For the fluid in the inner tube of the cold and hot heat exchangers, the heat transfer coefficient is given by Eq. (2.38).

$$h_{f,hex} = Nu \frac{k_{f,hex}}{d_{h,hex}} \tag{2.38}$$

In Eq. (2.38), the Nusselt number Nu is obtained using different correlations depending on the Reynolds number Re.

The simulations of the model are performed by Kamran et al. (2016) [22] using FLUENT. The results of the simulation indicate that the micro-channel regenerators have a better cooling capacity than parallel plate regenerators, by a margin of 7%.

Kamran et al. (2016) [23] continued the numeric modelling of the AMR refrigerator using micro-channel regenerators to develop it for a multi-layer/multi-material regenerator. The materials that are used apart from the hypothetical compounds of Gd are the compounds based on the alloy $LaFe_{13-x-y}Co_x Si_y$, that are available commercially. For the momentum and energy equations, as well as the finite difference simulation, Eq. (2.31) to Eq. (2.35) apply. The effectiveness-NTU relations also apply for the heat transfer between the MCM and HTF. The major difference is in the boundary conditions that are used and the computational scheme, since the arrangement of the regenerator is multi-material in contrast to the previous literature, which is a single material regenerator. By using multiple MCMs, the cooling capacity is found to be enhanced. However, the zero temperature span is found to be reduced on using multiple materials.

Mugica et al. (2018)

Mugica et al. (2018) [24] developed a Direct Numerical Simulation (DNS) solver in 3D, for better design of magnetocaloric refrigerators. The solver covers four physical aspects: the magnetic field, fluid velocity field, temperature field and the MCE. The MCM that is used for the simulation is Gd and the HTF used is water.

The first part of the DNS solver consists of the continuity equation and the Navier-Stokes equation of the fluid for determining the incompressible hydrodynamic field. These correspond to Eq. (2.39) and Eq. (2.40) respectively.

$$\nabla \cdot u = 0 \tag{2.39}$$

$$\frac{\partial u}{\partial t} + (u \cdot \nabla) u + \frac{\nabla P}{\rho_f} - \nu_f \nabla^2 u = 0 \tag{2.40}$$

Mugica et al. (2018) [24] introduced a magnetic potential in order to obtain the magnetic field in the regenerator at each position of the magnet. This potential is given by γ. Eq. (2.41) describes this equation in terms of the magnetic field intensity (vector).

$$H = -\nabla\gamma \tag{2.41}$$

Eq. (2.42) and Eq. (2.43) are then used to solve for the magnetic field in the regenerator.

$$\nabla \cdot \left[\mu_r(T, H) H \right] = 0 \tag{2.42}$$

$$\mu_r = 1 + \frac{M(T, H)}{H} \tag{2.43}$$

To solve for the temperature field in the solid MCM of the regenerator and the HTF, an energy balance is made for each phase. The equations are similar to those developed by previous authors.

$$\kappa_H(T, H) \frac{\partial T_s}{\partial t} + \mu_0 T_s \frac{\partial M(T, H)}{\partial T}\bigg|_H \frac{\partial H}{\partial t} - k_s \nabla^2 T = 0 \tag{2.44}$$

$$\frac{\partial T_f}{\partial t} + \boldsymbol{u} \cdot \nabla T - \frac{k_f}{\rho_f c_f} \nabla^2 T = 0 \tag{2.45}$$

Eq. (2.44) and Eq. (2.45) are similar to Eq. (2.17) and Eq. (2.18) developed by Nielson (2010) [19]. There is also a close similarity between Eq. (2.44) and Eq. (2.4) which was developed for the solid phase by de Vries and v. d. Meer (2017) [16]. The second term of Eq. (2.44) represents the volumetric heat due to the MCE, which is simply given as $\dot{q}_{MCE}$ in Eq. (2.4).

Table 2.4 summarizes the numerical modelling carried out by the above authors for the HTF.

Table 2.4: Summary of numerical modelling: HTF

Ref.	Unsteady term	Conduction term	Convection term	Heat transfer term	Viscous term	Dimension	Geometry
[13]	$\varepsilon \frac{\partial T_f}{\partial t} - \dot{T}_{loss}$	$\varepsilon \left(\frac{k_{f,eff}}{\rho_f c_{p,f}} + D \right) \times \frac{\partial^2 T_f}{\partial x^2}$	$-u \frac{\partial T_f}{\partial x}$	$-\frac{\alpha \sigma}{\rho_f c_{p,f}} (T_f - T_s)$	$-\frac{1}{\rho_f c_{p,f}} \left\| \frac{\partial p}{\partial x} \right\| u$	1 D	Packed bed
[19]	$\frac{\partial T_f}{\partial t}$	$\frac{k_f}{\rho_f c_f} \left(\frac{\partial^2 T_f}{\partial x^2} + \frac{\partial^2 T_f}{\partial y^2} \right)$	$-(\mathbf{u} \cdot \nabla) T_f$	-	-	2 D	Parallel plate
[20]	$A_c \varepsilon \rho_f c_f \frac{\partial T_f}{\partial t}$	$\frac{\partial}{\partial x} \left(k_{\text{disp}} A_c \frac{\partial T_f}{\partial x} \right)$	$\dot{m}_f c_f \frac{\partial T_f}{\partial x}$	$\frac{Nu k_f}{d_h} \sigma A_c (T_f - T_s)$	$\frac{\partial P}{\partial x} \frac{\dot{m}_f}{\rho_f}$	1 D	Packed bed
[21]	$\rho_f \cdot c_f \cdot \left(\frac{\partial T_f}{\partial t} \right)$	$k_f \cdot \frac{\partial^2 T_f}{\partial x^2}$	$\rho_f \cdot c_f \cdot u \cdot \frac{\partial T_f}{\partial x}$	$\dot{q}_{HT}$	$\dot{q}_{visco}$	1 D	Rectangular channels
[22]	$\frac{\partial T_f}{\partial t}$	$\alpha_f (\nabla^2 T_f)$	$u \cdot \nabla T_f$	-	-	3 D	Micro-channel
[24]	$\frac{\partial T_f}{\partial t}$	$\frac{k_f}{\rho_f c_f} \nabla^2 T$	$u \cdot \nabla T$	-	-	3 D	Packed bed

Table 2.5 shows the same summary of the numerical modelling carried for the solid MCM in the regenerator.

Table 2.5: Summary of numerical modelling: Solid MCM

Ref.	Unsteady term	Conduction term	MCE term	Heat transfer term	Dimension	Geometry
[13]	$(1-\varepsilon)\frac{\partial T_s}{\partial t} + \frac{\partial T_{MCE}}{\partial t}$	$(1-\varepsilon)\frac{k_{s,eff}}{\rho_s c_s}\frac{\partial^2 T_s}{\partial x^2}$	-	$-\frac{\alpha\sigma}{\rho_s c_s}(T_s - T_f)$	1 D	Packed bed
[16]	$\rho C_p \frac{\partial T}{\partial t}$	$\nabla \cdot (k\nabla T)$	$\dot{q}_{MCE}$	-	2 D	Rectangular plates
[19]	$\frac{\partial T_s}{\partial t}$	$\frac{k_s}{\rho_s c_s}\left(\frac{\partial^2 T_s}{\partial x^2} + \frac{\partial^2 T_s}{\partial y^2}\right)$	-	$\frac{Nu k_f}{d_h}\sigma A_c(T_f - T_s)$	2 D	Parallel plate
[20]	$A_c(1-\varepsilon)\rho_s c_H \frac{\partial T_s}{\partial t}$	$\frac{\partial}{\partial z}\left(k_{\text{stat}}A_c\frac{\partial T_s}{\partial x}\right)$	$A_c(1-\varepsilon)\rho_s c_H T_s\left(\frac{\partial s}{\partial H}\right)_{T_s}\frac{\partial H}{\partial t}$	-	1 D	Packed bed
[21]	$\rho_s c_p \frac{\partial T_s}{\partial t}$	$k_s\frac{\partial^2 T_s}{\partial x^2}$	$\frac{\partial T_{ad}(T_s,H_{in})}{\partial H_{in}}\cdot\frac{\partial H_{in}}{\partial t}\cdot\rho_s\cdot c_p(T_s,H_{in})$	$\dot{q}_{HT}$	1 D	Rectangular channels
[22]	$\frac{\partial T_s}{\partial t}$	$\alpha_s(\nabla^2 T_s)$	-	-	3 D	Micro-channel
[24]	$\kappa_H(T,H)\frac{\partial T_s}{\partial t}$	$k_s\nabla^2 T$	$\mu_0 T_s\frac{\partial M(T,H)}{\partial T}\Big|_H\frac{\partial H}{\partial t}$	-	3 D	Packed bed

The momentum balance has also been carried out by some of the authors. It is important to study the momentum balance of the HTF, since the flow changes direction during each cycle. Therefore, Table 2.6 summarizes the momentum balance carried out by the authors.

Table 2.6: Summary of momentum balances carried out by the authors

Ref.	Unsteady term	Inertial term	Viscous term	Pressure term
[13]	$\frac{\rho_f}{\epsilon}(\frac{\partial u}{\partial t})$	$\frac{E\rho_f}{K^{1/2}}\lvert u \rvert u$	$\frac{\mu_f}{K}u$	$\frac{\partial P}{\partial x}$
[22]	$\rho_f(\frac{\partial u}{\partial t})$	$\rho_f u \cdot \nabla u$	$-\mu_f \nabla^2 u$	∇P
[23]	$\rho_f(\frac{\partial u}{\partial t})$	$\rho_f u \cdot \nabla u$	$-\mu_f \nabla^2 u$	∇P
[24]	$\frac{\partial u}{\partial t}$	$(u \cdot \nabla)u$	$\nu_f \nabla^2 u$	$\frac{\nabla P}{\rho_f}$

2.7. Heat source and heat sink for Dutch Dwellings

The heat source that is to be studied for this project is a BHE and the heat sink is the Dutch dwellings. This chapter focuses on the heat source and the amount of heat it can deliver to the hot water buffer and the space in the dwelling, and the thermal requirements of the hot water buffer and the space in the dwelling.

2.7.1. Borehole Heat Exchangers

BHEs are the most widely used ground source heat exchangers. They are basically heat exchangers inside boreholes. The main purpose of these heat exchangers is the extraction of heat from the soil at shallow levels. The BHEs can be of two types: U-tube and a pair of coaxial pipes. The BHEs are utilized to extract the heat from the top layers of the earth's crust that are at relatively low temperatures. In this way, the temperature of the HTF circulating through the heat exchanger is increased. The energy transfer from the surrounding soil to the BHEs is through conduction. The temperature of the soil fluctuates a lot at shallow depths, and it becomes more uniform with increasing depth below the ground level [25]. Therefore, as the borehole is located at relatively shallow levels, the temperature of the soil fluctuates a lot, therefore the conductive heat transfer from the soil to the BHE is quite low and non-uniform and is insufficient to attain even medium temperatures.

If the borehole is situated at a deeper level, the amount of heat extracted can be enhanced, thereby increasing the output temperature of the HTF. This type of BHE is called Deep BHE (DBHE). Other advantages that the DBHE has, apart from the higher temperature of the surrounding rocks, are higher heat transfer area and the larger heat conductivity of the surrounding rocks. However, its thermal capacity is less compared to that of a thermal water well at similar depth.

It is important to study the heat transfer through the BHEs, since they are the heat source, and it will help in determining the amount of heat extracted from this source.

Al-Khoury et al. (2010)
Al-Khoury et al. (2010) [26] modelled the heat transfer in double U-tube BHEs and the surrounding soil using finite element methods. The main purpose of this model is to simulate the heat transfer processes in multiple number of borehole heat exchangers that are embedded in multiple layers of soil mass. The model that is developed is in three dimensions.

The soil mass surrounding the borehole is considered to be a two-phase porous material in the presence of groundwater flowing through the pores (solid particles and fluid groundwater). If the soil is dry, then it is a one-phase material (solid particles only). Therefore, the heat transfer from the soil mass to the BHE is a combination of conduction and convection. The heat transfer through conduction takes place between the lower layers of the earth, the air and the tube walls of the BHE. The convective heat transfer occurs as a result of the groundwater flowing through the pores (diffusion). Therefore, Al-Khoury et al. (2010) [26] developed an energy balance for the solid and the fluid phase of the soil mass using Fourier's law given below by Eq. (2.46) and Eq. (2.47) respectively.

$$(1-\epsilon)\rho c_p \frac{\partial T_s}{\partial t} - (1-\epsilon)\nabla(k\nabla T_s) = 0 \tag{2.46}$$

$$\epsilon \rho c_p \frac{\partial T_f}{\partial t} + \rho c_p \mathbf{u}\nabla T_f - \epsilon\nabla(k_f \nabla T_f) = 0 \tag{2.47}$$

On developing this energy balance, Al-Khoury et al. (2010) [26] assumed the two phases of the soil mass to be in thermodynamic equilibrium and that there is no net heat transfer between the two phases. Therefore:

$$T_s = T_f = T \tag{2.48}$$

On implementing Eq. (2.48), the following energy balance is obtained for the two-phase material.

$$\rho c_p \frac{\partial T}{\partial t} + \rho c_p \mathbf{u} \nabla T - \nabla(k \nabla T) = 0 \tag{2.49}$$

The double U-tube BHE comprises a borehole filled with grout, two inner pipes and two outer pipes. Each pair of inner and outer pipes form a U-tube. Therefore, this double U-tube BHE system consists of a total of 5 pipes, including the grout filled borehole. Al-Khoury et al. (2010) [26] modelled the transient heat transfer through this system using a control volume approach. The control volume of the system with all the pipes is shown in Fig. 2.9.
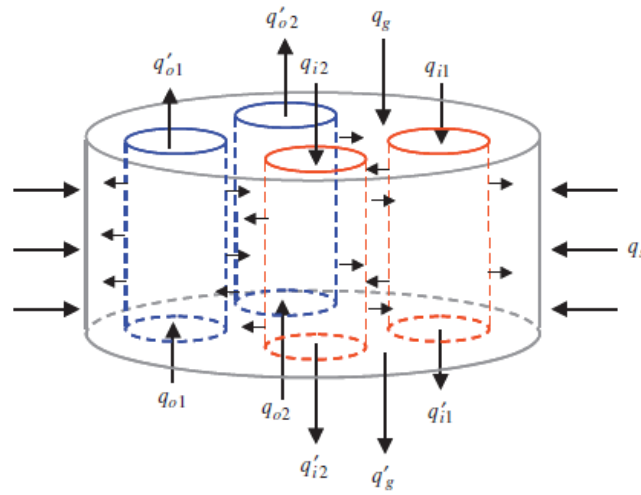
Figure 2.9: Control volume for BHE system [26] q_{o1} is the heat that is entering and leaving the first outer pipe of the BHE. q_{o2} is the heat that is entering and leaving the second outer pipe. q_{i1} is the heat entering and leaving the first inner pipe and q_{i2} is the heat entering and leaving the second inner pipe. q_g is the heat entering and leaving the grout of the BHE.

Al-Khoury et al. (2010) [26] developed the following energy balance for the inner pipes, outer pipes and the grout-filled borehole respectively.

$$\rho c_r \frac{\partial T_i}{\partial t} - k_r \frac{d^2 T_i}{dz^2} + \rho c_r u \frac{d T_i}{dz} = U_{ig}\left(T_i - T_g\right) \tag{2.50}$$

$$\rho c_r \frac{\partial T_o}{\partial t} - k_r \frac{d^2 T_o}{dz^2} - \rho c_r u \frac{d T_o}{dz} = U_{og}\left(T_o - T_g\right) \tag{2.51}$$

$$\rho c_g \frac{\partial T_g}{\partial t} - k_g \frac{d^2 T_g}{dz^2} = U_{ig}\left(T_g - T_i\right) + U_{og}\left(T_g - T_o\right) \tag{2.52}$$

Eq. (2.50) to Eq. (2.52) are solved, subject to certain boundary conditions. The heat transfer coefficients are determined, and the equations are subject to finite element analysis to study the temperature profiles of the coolant (HTF) in the inner and outer pipes.

Rees et al. (2013)
Rees et al. (2013) [27] designed a model in three dimensions for the heat transfer and fluid flow through a BHE. The model is designed, such that it enables the determination of the dynamic behaviour of various

components over small and large timescales. A finite volume approach is used for this model, wherein multi-block meshes are used to represent the soil, the pipes, the HTF and the grout appropriately.

The integral form of the convection-diffusion temperature equation is used in this model by Rees et al. (2013) [27] and is given by Eq. (2.53).

$$\frac{\partial}{\partial t} \int_V \rho c_p T d\mathbf{V} + \int_A \rho c_p T \mathbf{u} \cdot \mathbf{n} d\mathbf{A} = \int_A k \nabla T \cdot \mathbf{n} d\mathbf{A} \tag{2.53}$$

Eq. (2.53) is discretized using the finite volume method. Each term of the convection-diffusion temperature equation is handled separately.

The discretized model is then validated analytically, as well as experimentally. This validation is done in order to obtain the most suitable design parameters for the BHEs, which can be more of a cross check, if the accuracy of the model is high enough compared to the analytical and experimental results. The model is found to predict the temperature at the outlet of the pipe with high accuracy over a period of 18 months. The monthly heat transfer calculated using this model is also accurate on comparison with experimental data. Since the accuracy of heat transfer is quite high, the model can be used to predict heat transfer variations with the depth and diameter of the borehole, thereby verifying the most suitable parameters for the design of BHEs.

In order to initiate the modelling for the heat transfer from the soil to the BHE, it is crucial to understand the temperature variation in the soil in the Netherlands through the year and determine the temperature of the soil on the coldest day. A good estimate for the soil temperature on the coldest day would be 6°C [28]. This would be the constant value of the temperature for a depth of around 5 m or below.

2.7.2. Dutch Dwellings
The heat from the magnetic heat pump is to be supplied to the space in the housing through the under floor heating system, and to the domestic hot water buffer. Therefore, a Dutch dwelling is the heat sink for this magnetic heat pump cycle. On the coldest day, it is estimated that the total thermal power required for Dutch dwellings is 3 kW, 60% of which is used for space heating and 30% of which is used for the domestic hot water buffer. Therefore, the thermal power required for space heating is 1.8 kW and 0.9 kW for the domestic hot water buffer.

It is important to understand the temperature requirements of the space Dutch dwelling, in order to obtain the temperature to be achieved at the end of the magnetic heat pump cycle. A good estimate of the maximum temperature to be achieved by the under floor heating system on the coldest day should be 29°C. Therefore, if the under floor heating system is to supply heat to this temperature, the temperature of the HTF entering the under floor heating system should at least be 35°C, allowing for a sufficient temperature difference for the heat transfer to take place. In case of the hot water buffer, the water temperature is very high and is above 40°C. Therefore, the HTF temperature should be at least 50-60°C in order to achieve the requirements for the domestic hot water buffer.

2.8. Selection of Important Aspects of Magnetocaloric Heat Pumps

Certain choices are to be made for the important components of the magnetocaloric heat pump. The selection of these components is discussed in this chapter.

2.8.1. Selection of Regenerator Geometry

The geometry that is chosen as a starting point for modelling the heat and momentum transfer through the regenerator is a packed bed geometry. The packed bed geometry is the most commonly used geometry by various authors in modelling the AMR cycle. Such a regenerator usually contains a packed bed of MCM spheres. The spheres are usually made of Gadolinium. The packed bed has a certain porosity ϵ, and the HTF flows through the pores. The packed bed geometry makes it convenient for the regenerator to be numerically modelled in one dimension quite accurately. Therefore, this choice is a good starting point before other suitable geometries are explored.

2.8.2. Choice of Numerical Model

After selecting the geometry of the regenerator, it is important to select the most suitable equations from the numerical modelling for the selected packed bed geometry. Therefore, the most suitable choice is a combination of equations developed by Trevizoli et al. (2016) [13], and those developed by Johra et al. (2019) [20], since both the groups of authors used a packed bed regenerator geometry. Therefore, Eq. (2.15), Eq. (2.16), Eq. (2.19) and Eq. (2.20) are used in order to develop the initial model for the heat transfer for the packed bed regenerator, and Eq. (2.14) is used to initially model the momentum transfer through the regenerator.

2.8.3. Selection of Heat Transfer Fluid and Magnetocaloric Material

The HTF to be circulated through the heat pump cycle is to be selected, once the numerical model to be used for the regenerator is chosen. Preferably, a single HTF for the entire cycle is chosen, since it will avoid unnecessary heat losses arising from the need of additional heat exchangers due to more than one HTFs. While selecting the HTF, its properties like viscosity and density should be considered. The HTF that is most suitable for this heat pump cycle would be a solution of water and ethylene glycol. The composition of the solution would be 80% water and 20% ethylene glycol by volume. The main reason for the selection of the ethylene glycol solution is because of its antifreeze properties, that are suitable for standard heating and cooling applications, making it the most common antifreeze fluid. The 20% ethylene glycol solution has a freezing point -7.9°C [29]. The composition of 20% ethylene glycol is chosen because the viscosity and density of this composition is quite low, which maybe beneficial in reducing the pressure drop during the flow of the HTF through the ducting. Another reason for this choice is that the specific heat capacity of this composition is quite high compared to other compositions of the ethylene glycol solution [29]. Table 2.7 shows the properties of the chosen HTF.

Table 2.7: Properties of 20% ethylene glycol solution [29]

Property	Value
Freezing point (°C)	-7.9
Boiling point (°C)	102.2
Dynamic viscosity (at room temperature) (Pa s)	$1.4*10^{-3}$
Density (at room temperature) (kg/m^3)	1030
Specific heat capacity (J/(kg K))	3807

The solid MCM that is selected for this project is pure Gd. Although the MCE that is provided by Gd is less when compared with some of its alloys, the reason for its selection is that it is commonly available, and that its properties can be obtained quite easily. The properties of Gd that are used in this project are given in Table 3.1 in the following chapter.

<div style="text-align: right; font-size: 4em;">3</div>

Development of the Magnetocaloric Heat Pump Cycle Model

This chapter focuses on the project work of developing the magnetic heat pump cycle. This includes the discussion of the regenerator model with dimensions of the selected geometry (packed bed) and developing the heat transfer model using the energy balance equations reported in the literature review.

3.1. The Magnetic Heat Pump System

This part is dedicated to the description of the complete magnetic heat pump cycle with the regnerator, the BHEs and the space and domestic hot water heating. This includes an analysis of the regenerator setup along with the dimensions of the regenerator. Fig. 3.1 is a schematic of the heat pump system to form the complete AMR cycle.
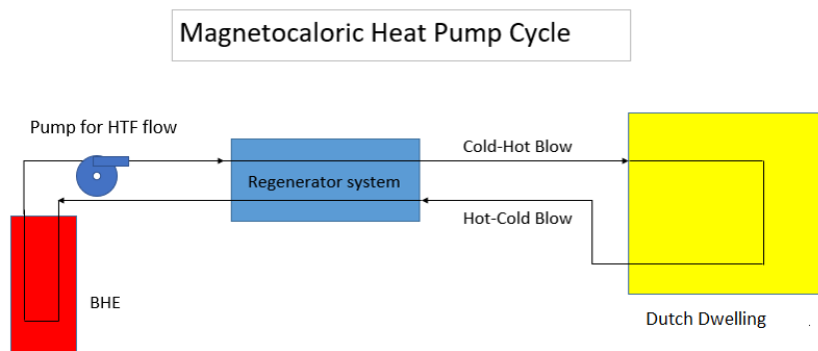
Figure 3.1: Magnetocaloric Heat Pump Cycle: The main components of the cycle shown are the BHE, the regenerator and the Dutch dwelling. The pump is shown as a means of transporting the HTF between the BHE and the Dutch dwelling

As shown in Fig. 3.1, the BHE is the heat source that extracts heat from underground and provides it to the HTF. The HTF then passes through the regenerator which is magnetized at this point. The heat exchange between the HTF and the regenerator results in a further temperature increase in the HTF before it exits the regenerator and enters the underfloor space heating system which is the heat sink. For modelling the heat transfer through the different parts of the cycle, it is first crucial to understand the heat transfer mechanisms between the solid MCM in the regenerator and the HTF. Therefore, in the following part of this chapter, the model of the regenerator system is first discussed with the dimensions, which is followed by the development of the heat transfer model to model the heat exchange between the regenerator and the HTF.

3.2. Model of the Regenerator System

The regenerator system taken as basis for this project consists of 7 regenerators in a circular arrangement similar to that proposed by Huang et al. (2019) [18]. This arrangement is shown in Fig. 3.2.

<div style="text-align: center;">29</div>
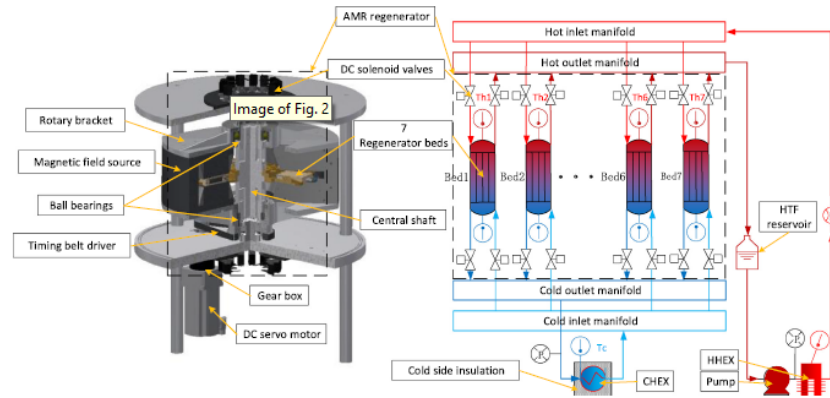
Figure 3.2: Regenerator arrangement around the magnetic field source [18]: The air gap of the magnet, through which each regenerator fits, is shown on the left hand side. The valves through the which the HTF flows and enters the regenerators are shown in the right hand side.

As shown in Fig. 3.2, the 7 regenerators are arranged circularly covering 360°. Therefore, each regenerator is positioned such that the angle made between any two regenerators is 51.42°. Permanent magnets are used to provide the magnetic field since they are more common and less expensive compared to other magnets. It can produce a maximum field of around 2 T. The regenerators are placed in this manner so that the permanent magnets can sweep over each regenerator completely to achieve the full magnetization. In Fig. 3.2, it is also observed that the number of valves that are open for the fluid flow is 4. This means that 4 regenerators will receive the total flow during one blowing process and 3 regenerators will receive the total flow for the other blowing process (since the total number of regenerators is 7). Therefore, the flow is considered to be divided into 3.5 valves on an average. Hence, the flow rate that is received by each regenerator is the total flow rate of the system divided by 3.5.

Each regenerator is a cuboid filled with small Gd spheres to form a packed bed. The dimensions of the regenerator are chosen from Huang et al. (2019) [18] in order to be able to verify the developed model by comparing the results with those of these authors. Table 3.1 provides the dimensions of the regenerator and the properties of the Gd particles.

Table 3.1: Regenerator Properties [18]

Property	Value
Width (m)	0.045
Height (m)	0.013
Length (m)	0.06
Porosity	0.36
Diameter of each spherical particle (m)	0.0006
Density of Gd (kg/m^3)	7504

Fig. 3.3 depicts the model of the regenerator with the dimensions given in Table 3.1.
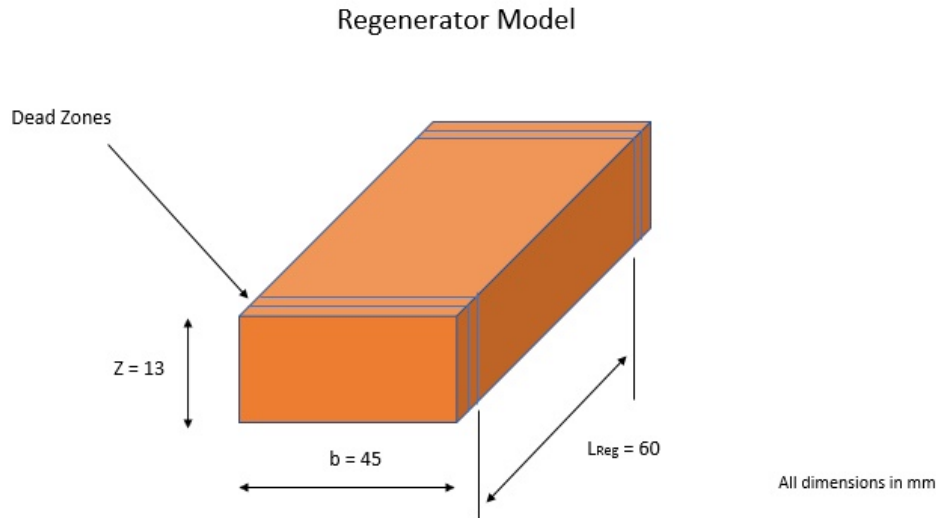
Figure 3.3: Regenerator model with dimensions: The length of the regenerator shown in the figure is 60 mm, excluding the dead zones.

In Fig. 3.3 it is to be noted that 60 mm is the length of the packed bed and it does not include the dead zones in the regenerator.

3.3. Development of Heat Transfer Model for the Active Magnetic Regenerator

This part focuses on the heat transfer model that is developed for the active magnetic regenerator using MAT-LAB and SIMULINK. For the model development, the control volume approach is used in order to take into account the transient temperature response as well as the distance-dependent temperature response of the HTF. For simplicity, the magnetic field is assumed to be applied and removed instantaneously at the end of the Hot-to-Cold blow and the Cold-to-Hot blow respectively. The modelling of the transient heat transfer between the HTF and the solid MCM is done using SIMULINK and the instantaneous application and removal of the magnetic field is carried out through a MATLAB code linked with the SIMULINK model. First, the control volume approach is discussed along with the heat transfer equations for the HTF and the solid regenerator. This is followed by the discussion of the method for switching between the hot-to-cold and cold-to-hot blow, through the use of the conditional switches in SIMULINK and the discussion of the approach for applying and removing the magnetic field instantaneously using MATLAB. The simulations are carried out with fixed time steps in order to improve accuracy in the model and also to achieve periodic steady-state in the simulation more easily. The size of each time step in the model is such that the total time required for one blowing process (Hot-to-Cold or Cold-to-Hot) comprises 50 such time steps.

3.3.1. The Control Volume Approach

The regenerator is divided into 30 control volumes in order to increase the accuracy of the model. Therefore if the total length of the regenerator L_{Reg} is 0.06 m, then the length of each control volume is given by Eq. (3.1).

$$L_{cv} = \frac{L_{Reg}}{30} = \frac{0.06}{30} = 0.002 \ m \tag{3.1}$$

The energy balance for one control volume for the solid and HTF are shown in Fig. 3.4.
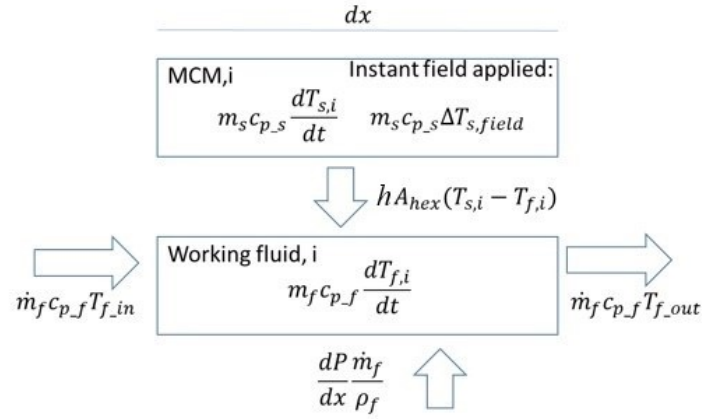
Figure 3.4: Energy balance for Solid Regenerator and HTF. The common mode of heat transfer between the solid MCM and the HTF is the convective heat transfer.

In each control volume, Eq. (2.19) and Eq. (2.20) by Johra et al. (2019) [20] apply. The equations are simplified according to the conditions for the model development. The first condition is that the magnetic field is applied instantaneously, therefore, the MCE terms in Eq. (2.20) can be neglected. The second condition is that the heat transfer due to conduction between the solid regenerator and the HTF is considered negligible. Hence, the conduction terms can be neglected in both the equations. Eq. (3.2) and Eq. (3.3) are the simplified heat transfer equations for the HTF and the solid respectively.

$$-\dot{m}_f c_{p,f} \frac{\partial T_f}{\partial x} - \frac{Nuk_f}{d_h} \sigma A_c \left(T_f - T_s\right) + \left|\frac{\partial P}{\partial x} \frac{\dot{m}_f}{\rho_f}\right| - A_c \varepsilon \rho_f c_{p,f} \frac{\partial T_f}{\partial t} = 0 \tag{3.2}$$

$$\frac{Nuk_f}{d_h} \sigma A_c \left(T_f - T_s\right) - A_c(1-\varepsilon)\rho_s c_p \frac{\partial T_s}{\partial t} = 0 \tag{3.3}$$

Eq. (3.2) and Eq. (3.3) are integrated over length dx to obtain Eq. (3.4) and Eq. (3.5) respectively.

$$-\dot{m}_f c_{p,f}(T_{f,out} - T_{f,in}) - h_f A_s \left(T_f - T_s\right) + \left|\frac{\partial P}{\partial x} \frac{\dot{m}_f}{\rho_f} L_{cv}\right| - V_{cv} \varepsilon \rho_f c_{p,f} \frac{dT_f}{\partial t} = 0 \tag{3.4}$$

$$h_f A_s \left(T_f - T_s\right) - V_{cv}(1-\varepsilon)\rho_s c_{p,s} \frac{dT_s}{\partial t} = 0 \tag{3.5}$$

Where:
V_{cv} = Volume of one regenerator control volume (m^3)
h_f = convective heat transfer ($Wm^{-2}K^{-1}$) given by Eq. (3.6).

$$h_f = \frac{Nuk_f}{d_h} \tag{3.6}$$

A modification to Eq. (3.4) is the inclusion of heat losses from the HTF. These losses are in the form of heat leakages from the HTF to the surroundings through the casing of the regenerator. Therefore, a heat transfer coefficient is obtained to consider these losses and the heat exchange area considered in this case is the area of the regenerator casing. Eq. (3.7) is the modified version of the HTF energy balance which considers these heat losses.

$$-\dot{m}_f c_{p,f}(T_{f,out} - T_{f,in}) - h_f A_s \left(T_f - T_s\right) + \left|\frac{\partial P}{\partial x} \frac{\dot{m}_f}{\rho_f} L_{cv}\right| - V_{cv} \varepsilon \rho_f c_{p,f} \frac{dT_f}{\partial t} - h_{loss} A_{case}(T_f - T_{air}) = 0 \tag{3.7}$$

A_s is the surface area of heat exchange between solid and HTF given by Eq. (3.8).

$$A_s = \sigma * A_c * L_{cv} \tag{3.8}$$

In Eq. (3.7), the first term represents the position-dependent temperature response of the HTF, due to its flow through the voids of the regenerator. The second term represents the convective heat transfer between the

HTF and the solid regenerator, and it is the common term for both Eq. (3.5) and Eq. (3.7). The third term of Eq. (3.7) is the heat production due to the pressure drop of the fluid flow. The fourth term represents the transient temperature response of the HTF and the final term represents the heat losses to the environment. In Eq. (3.5) there are just two terms, the first term being the common term, which is convective heat transfer, and the second term, which is the transient temperature response of the solid regenerator. Eq. (3.5) and Eq. (3.7) are applied to each control volume of the regenerator. Another simplification that is made in the model is that the outlet temperature of the HTF is equal to the transient HTF temperature, in other words:

$$T_{f,out} = T_f \tag{3.9}$$

3.3.2. Calculation of MCM and HTF Properties

For each control volume and instant of time, the properties are calculated for the continuously changing HTF temperature to enhance the accuracy of the model. The properties that are required for the HTF are the density ρ_f, the specific heat capacity $c_{p,f}$, the dynamic viscosity μ_f and the thermal conductivity k_f. Eq. (3.10) to Eq. (3.13) are used to calculate the four temperature-dependent properties for 20% ethylene glycol.

$$\rho_f = -0.0032 * T_f^2 - 0.2163 * T_f + 1034.7 \tag{3.10}$$

$$c_{p,f} = 2.1265 * T_f + 3820.6 \tag{3.11}$$

$$\mu_f = -0.0000000197 * T_f^3 + 0.000002677 * T_f^2 - 0.000137 * T_f + 0.003594 \tag{3.12}$$

$$k_f = -0.0000016 * T_f^2 + 0.0011 * T_f + 0.4708 \tag{3.13}$$

The required properties of the solid regenerator material (Gd) are the density ρ_s and the specific heat capacity $c_{p,s}$. The density can be treated as a constant throughout the cycle, as it does not vary too much with temperature, and its value is given in Table 3.1. However, the specific heat capacity of Gd changes significantly close to its Curie temperature. Therefore, the temperature dependent specific heat capacity is implemented in the heat transfer model. Since the change is discontinuous, the spline function is used in MATLAB in order to account for the discontinuity in the specific heat capacity of the solid. In order to obtain the spline, the data for the specific heat capacity as a function of temperature is collected [31]. The specific heat capacity not only depends on the temperature but also on magnetic field. The data set is obtained for a temperature range of 250 to 350 K, and for a magnetic field range of 0 to 2 T. The spline function in MATLAB is then used in order to find the value of the specific heat capacity for a particular solid temperature. Since the specific heat capacity of the solid also depends on the magnetic field, two splines are to be obtained corresponding to two different functions of specific heat capacity with temperature: One for no magnetic field and one for a magnetic field of 0.875 T. The plots of the specific heat capacity as a function of the solid temperature for no magnetic field and 0.875 T are shown in Fig. 3.5.
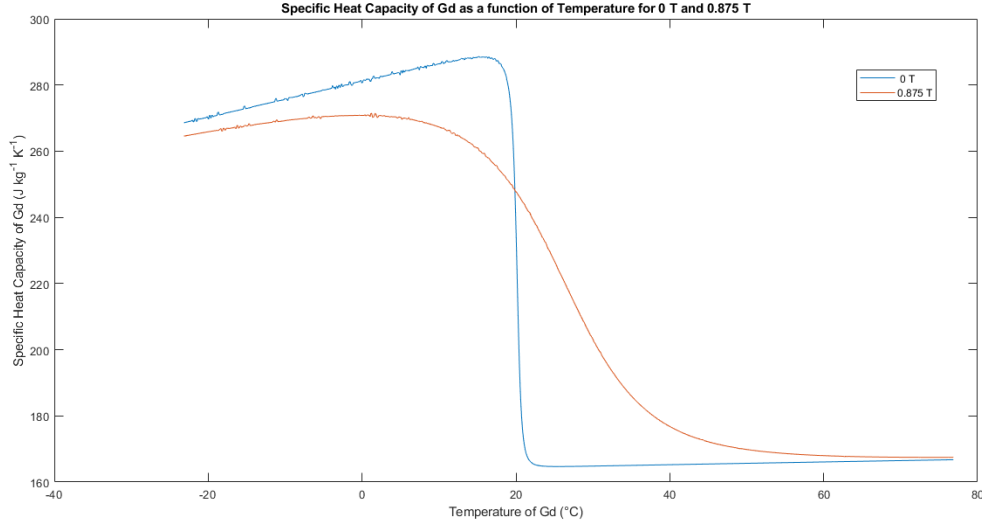
Figure 3.5: Specific heat capacity of the solid as a function of temperature for 0 T and 0.875 T. The curve for the specific heat capacity is smoother for 0.875 T.

The plot in Fig. 3.5 shows a discontinuity in the specific heat capacity at a temperature of Gd close to the Curie temperature for no magnetic field. The specific heat capacity drops from around 290 $Jkg^{-1}K^{-1}$ to around 160 $Jkg^{-1}K^{-1}$ for a very small temperature change in this range. The specific heat capacity vs temperature curve for 0.875 T has a smoother transition close to the Curie temperature compared to that for no magnetic field. The specific heat drops from around 270 $Jkg^{-1}K^{-1}$ to around 165 $Jkg^{-1}K^{-1}$ close to the Curie temperature of Gd.

The data of the specific heat capacity as function of Gd temperature for 0 T and 0.875 T are fed from the MATLAB workspace to the SIMULINK model using the simin function of SIMULINK. The workspace data is then fed to two MATLAB functions for calculating the specific heat capacity as a function of the transient temperature of the solid in each control volume of the model. The method that is used to calculate the specific heat capacity is spline interpolation, since it makes use of the splines that are created for 0 T and 0.875 T. Each MATLAB function corresponds to the specific heat capacity for 0 T and that for 0.875 T, depending on the blowing process.

3.3.3. Regenerator Geometry

The cross section of the regenerator is to be decided, and the chosen cross section is a rectangular cross section, such that it fits into the magnet for the magnetization and demagnetization. The width of the regenerator is given by b (m) and the height (or depth) of the regenerator is given by Z (m). Therefore, the cross section area of the regenerator is given by Eq. (3.14) and Eq. (3.15).

$$A_c = b * Z \tag{3.14}$$

$$A_c = 0.045 * 0.013 = 5.85 * 10^{-4} m^2 \tag{3.15}$$

Therefore, the volume of each control volume V_{cv} is obtained from Eq. (3.16).

$$V_{cv} = A_c * L_{cv} = 1.17 * 10^{-6} \ m^3 \tag{3.16}$$

The diameter of each spherical particle is given by d_p which is 0.0006 m as per Table 3.1. In order to calculate the other properties for the packed bed flow, a hydraulic diameter or characteristic length scale is required and is related to the porosity and the particle diameter through Eq. (3.17).

$$d_h = d_p * (\frac{\epsilon}{1 - \epsilon}) = 3.375 * 10^{-4} \ m \tag{3.17}$$

The specific surface area σ is given by Eq. (3.18).

$$\sigma = \frac{6 * (1 - \epsilon)}{d_p} = 6400 \ m^{-1} \tag{3.18}$$

Therefore, the area of heat exchange between the solid regenerator and the HTF is given by Eq. (3.19).

$$A_s = \sigma * b * Z * L_{cv} = 7.49 * 10^{-3} \ m^2 \tag{3.19}$$

The area of the regenerator casing A_{case} is the total surface of the area of the cuboid regenerator, taking into consideration the thickness of the regenerator casing (excluding the cross section area). The area of the casing is calculated for each control volume. Therefore, the length that is taken to calculate the surface area is the length of each control volume L_{cv}. The thickness of the regenerator casing on either side of the width and the height is 3.5 mm. Therefore, in order to calculate surface area including the regenerator casing thickness, the width and the height are added by 3.5*2 which is 7 mm. Therefore, the area of the casing is calculated using Eq. (3.20).

$$A_{case} = 2 * [(b + 0.007) * L_{cv} + (Z + 0.007) * L_{cv}] = 2.88 * 10^{-4} \ m^2 \tag{3.20}$$

The area of the casing is obtained in order to calculate the heat loss from the HTF to the surroundings through the regenerator casing.

3.3.4. Constitutive Equations for Fluid flow

The velocity of flow is calculated using Eq. (3.21).

$$u = \frac{\dot{m}_f}{\rho_f * \epsilon * A_c} \tag{3.21}$$

The Reynolds Number Re and Prandtl Number Pr are calculated using Eq. (3.22) and Eq. (3.23) respectively.

$$Re = \frac{\rho_f * u * d_h}{\mu_f} \tag{3.22}$$

$$Pr = \frac{\mu_f * c_{p,f}}{k_f} \tag{3.23}$$

The Nusselt Number Nu is calculated using the correlation for packed bed given by Mills [30]:

$$Nu = (0.5 * Re^{0.5} + 0.2 * Re^{\frac{2}{3}}) * Pr^{\frac{1}{3}} \tag{3.24}$$

The convective heat transfer coefficient h_f is then obtained using Eq. (3.6).

The pressure drop per unit length of the regenerator is given by the Ergun correlation [30]:

$$\frac{\partial P}{\partial x} = \frac{150 * \mu_f * u}{d_h^2} + \frac{1.75 * \rho_f * u^2}{d_h} \tag{3.25}$$

An estimate of the heat transfer coefficient for the losses is taken to be 20 $W \ m^2 \ K^{-1}$. The ambient temperature T_{air} in Eq. (3.7) is considered to be 25°C. Since this temperature is higher than the constant HTF temperature at the hot side (21.85°C), the heat loss is actually heat addition from the environment to the HTF in the regenerator through the casing. This may impact the cooling capacity of the regenerator since the HTF temperature rises as a result of this heat addition.

The heat transfer equations and correlations are applied for each control volume of the regenerator. The outlet HTF temperature $T_{f,out}$ of the one control volume will be the inlet HTF temperature $T_{f,in}$ for the next control volume.

3.3.5. Implementation of the Model in MATLAB and SIMULINK

The SIMULINK model is used only for simulating the Hot-to-Cold blow and the Cold-to-Hot blow without the application or removal of the magnetic field. The application and removal of the instantaneous magnetic field is done using a MATLAB code. To serve this purpose, the SIMULINK model is run cycle-wise using the MATLAB code. The 'sim()' command is used to run a SIMULINK model using the MATLAB code. The initial temperature of the HTF at the hot side and cold side is specified in MATLAB. These are the boundary conditions that decide the temperature span for simulating both the blowing processes. The AMR cycle could have been run using only SIMULINK, however, SIMULINK does not respond well to instantaneous changes in solid and fluid temperature due to the instantaneous application and removal of the magnetic field. When it was attempted to implement the magnetization and demagnetization in SIMULINK, the solid temperature instantaneously increased, but at the very next time step, the solid temperature decreased instantaneously to the same temperature before the field is being applied. Therefore, the only solution to this problem is the cycle-wise running of the SIMULINK model using a MATLAB code. The cycle-wise running of the MATLAB code is done using a 'for' loop. The count of the loop is the number of cycles that are required to be simulated, which is a user-defined choice. Each blowing process is simulated in one loop. This means that the 'sim()' command is used twice in one loop, once for the Hot-to-Cold blow and once for the Cold-to-Hot blow to complete one loop (cycle).

The running of the SIMULINK model using the MATLAB code requires the transfer of the data of certain variables from MATLAB to SIMULINK and vice-versa. The main variables that are required for transfer from MATLAB to SIMULINK are the initial temperatures of the HTF and the solid for each of the 30 control volumes in the SIMULINK model. A linear distribution is created for the initial solid and the HTF temperatures across the 30 control volumes. A linear distribution is created because it helps achieve the periodic steady-state condition faster. The linear distribution is done using the 'linspace' command in MATLAB. The end points of the linear distribution are the cold and hot reservoir temperatures, which correspond to the temperatures of the fluid entering the cold and hot side during the Cold-to-Hot blow and Hot-to-Cold blow process respectively. The number of points in the linear distribution is 30, corresponding to the number of the control volume. The solid and fluid have the same initial temperature in each control volume. The values of these initial temperatures are stored in two arrays, one for the solid and another for the fluid. These two arrays are created before the start of the 'for' loop for the cycles. The elements of these arrays are transferred to the initial condition blocks in each control volume in the SIMULINK model. There are some other variables that are to be transferred from SIMULINK to the MATLAB workspace using the 'simout' function block in SIMULINK, such as the temperatures of the solid MCM in each of the 30 control volumes at the end of one blowing process, since the functions of magnetization and demagnetization are to be applied only at the last time step of the corresponding blowing process. The temperatures of the HTF of each control volume at the end of one blowing process are also required since they are to be used as initial conditions for the fluid phase for the next blowing process. The other important variable required for transfer from MATLAB to SIMULINK is that for the flow direction. It has two values, each of them corresponding to one particular blowing process.

The implementation of the model using MATLAB and SIMULINK is summarized using the process flow diagram in Fig. 3.6.
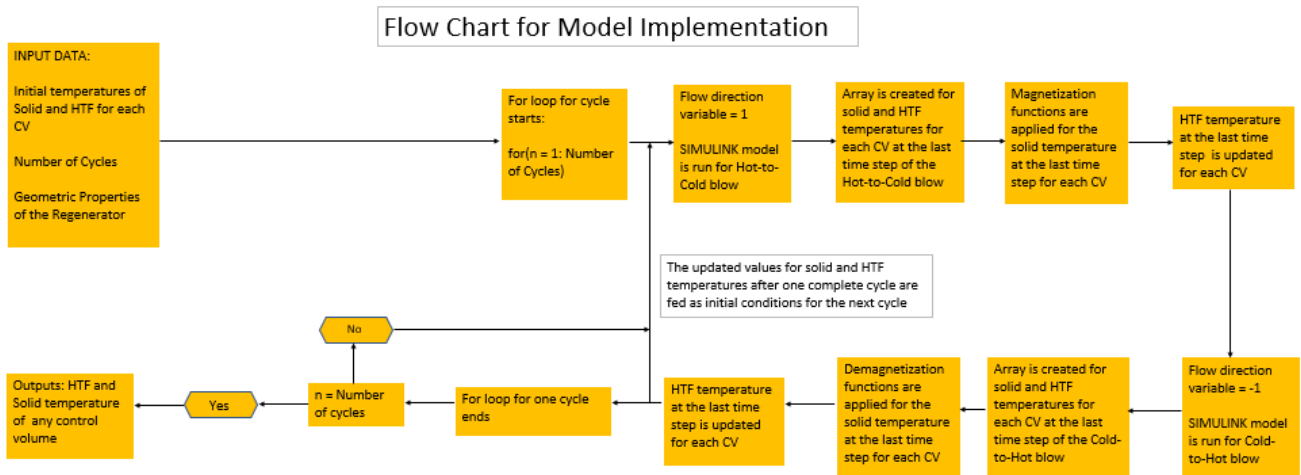
Figure 3.6: Flow chart for model implementation: The blocks on top correspond to the Hot-to-Cold blow and the blocks at the bottom correspond to the Cold-to-Hot blow

In Fig. 3.6, the upper set of blocks correspond to the Hot-to-Cold blow and the lower set of blocks correspond to the Cold-to-Hot blow. The input parameters at the top left corner refer to the geometric properties of the regenerator.

Inside the 'for' loop of the MATLAB script (Second block from the left at the top in Fig. 3.6), each of the blowing processes is run one after the other. This is done by specifying the corresponding value of the flow direction variable. The cycle starts with the Hot-to-Cold blow and the value of the flow direction variable for this blowing process is given as 1 (Third block at the top of Fig. 3.6). This value is given to the flow direction variable before the 'sim()' command is given in the script. The values of the solid and HTF temperatures of each control volume at the last time step of the Hot-to-Cold blow are extracted from SIMULINK and transferred and stored as arrays for the solid and fluid temperature respectively in the loop (Fourth block in Fig. 3.6). Each of these arrays has 30 elements corresponding to each control volume.

3.3.6. Instantaneous Magnetization and Demagnetization

The magnetization and demagnetization of the material is assumed to happen instantaneously and adiabatically. Similar to the specific heat capacity, the entropy also depends on the magnetic field apart from temperature. The total entropy data is required for Gd as a function of its temperature and magnetic field. Similar to the specific heat capacity of Gd, the total entropy of Gd as a function of temperature and magnetic field is obtained and stored in the MATLAB workspace [31]. The data set is obtained for a temperature range of 250 to 350 K, and for a magnetic field range of 0 to 2 T. The total entropy as a function of temperature and magnetic field is actually obtained from the specific heat capacity and the magnetization. Two sets of entropy temperature curves are required: One for no magnetic field and another one for 0.875 T. Similar to the specific heat capacity, a spline is created for the entropy as a function of temperature and spline interpolation is done on MATLAB to obtain the entropy for every value of temperature for 0 T and 0.875 T. However, since the MCE is done in the MATLAB code, the splines are not exported to the SIMULINK model. Using the spline, the entropy of Gd is obtained for its temperature at the last time step at 0 T field for the Hot-to-Cold blow. This is done after creating the array for the solid and HTF temperature at the last time step of this blowing process. Since the magnetization is assumed to be adiabatic, the total entropy remains constant. Therefore, the temperature of the solid after magnetization is obtained using the spline for 0.875 T at the value of the entropy at the last time step of the Hot-to-Cold blow. The temperature of Gd that is obtained using this curve is fed to the solid temperature array specified before the 'for' loop for each control volume, as the initial condition for the next blowing process. The value of the HTF at the last time step of the Hot-to-Cold blow is also fed to the initial HTF temperature array specified before the loop, as the initial condition for the next blowing process.

After updating the values for the solid and HTF temperatures for the next blowing process, the value of the flow direction variable is changed to -1 to suggest that the blowing process to be simulated is the Cold-to-Hot

blow. The SIMULINK model is then run in the MATLAB code for this blowing process. The procedure for this blowing process in the MATLAB code is similar to that for the Hot-to-Cold blow. The difference is the demagnetization process that is done using the splines for entropy as a function of temperature. The entropy of the solid is obtained using the spline for 0.875 T for the temperature of the solid at the last time step of the Cold-to-Hot blow. The new temperature of the solid is then obtained using the spline for 0 T at the value of the entropy at the last time step. This is the temperature of the solid after demagnetization and it is fed to the solid temperature array as the initial condition for the next cycle. The HTF temperature values at the last time step of the Cold-to-Hot blow are also fed to the HTF temperature array as the initial condition for the next cycle. The adiabatic magnetization and demagnetization procedure is summarized in Fig. 3.7 with temperature vs entropy (T-s) curves for 0 T and 0.875 T.
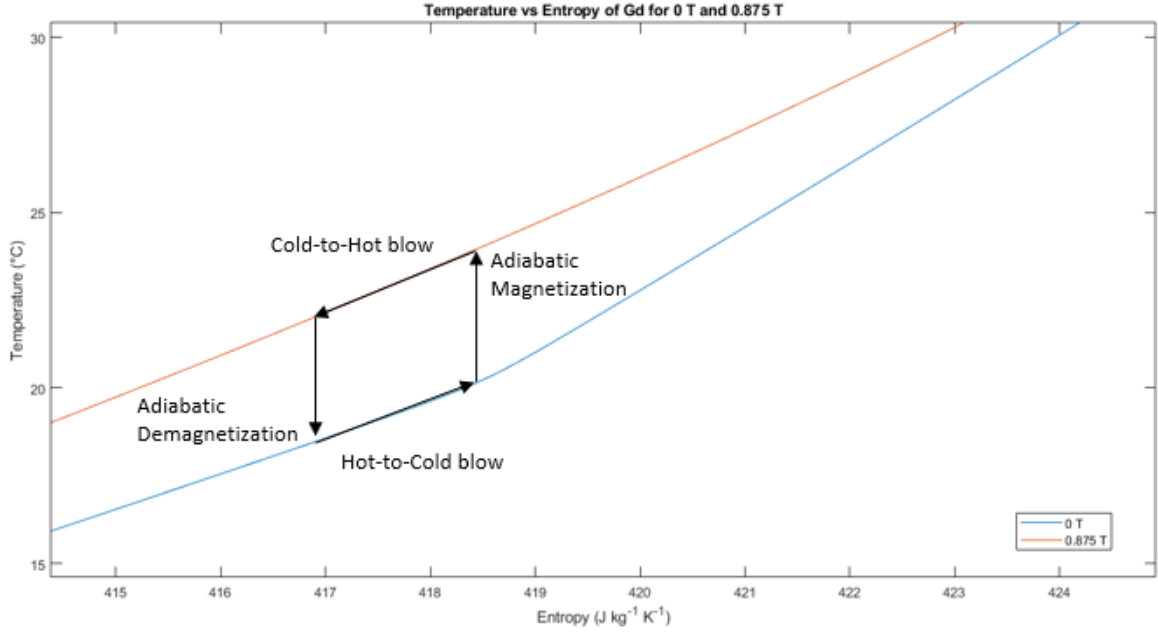
Figure 3.7: Adiabatic magnetization and demagnetization: The magnetic heat pump cycle is also depicted in the figure with the four stages: Hot-to-Cold blow, Adiabatic Magnetization, Cold-to-Hot blow and Adiabatic Demagnetization.

Fig. 3.7 also depicts the cycle that one control volume of the regenerator undergoes, using the temperature vs entropy curves. The first process is the Hot-to-Cold blow, wherein the temperature of the solid is increased by passing the HTF from the hot side through the regenerator, while keeping the regenerator demagnetized. The next process is the adiabatic magnetization wherein, the total entropy is constant and the temperature of the solid increases instantaneously due to the change of magnetic field from 0 T to 0.875 T. Then, the Cold-to-Hot blow takes place wherein, the HTF from the cold side passes through the regenerator, while keeping the material under the magnetic field, resulting in a decrease in solid temperature. Then the adiabatic demagnetization occurs instantaneously, wherein the temperature of the solid decreases at constant entropy due to the removal of the magnetic field.

The concept that is implemented is instantaneous adiabatic magnetization and demagnetization. Therefore, the total entropy remains constant while the temperature changes. However, there is a decrease in magnetic entropy, resulting in an equal increase in electronic and lattice entropy for the total entropy to remain constant (as per Eq. (2.1)). The increase in electronic and lattice entropy causes the temperature increase in the MCM. Therefore, on combining Eq. (2.2) and Eq. (2.3), the equation for adiabatic temperature change as a function of change in magnetic entropy is obtained.

$$\Delta T_{ad}(T, \Delta H) = -\frac{T}{C(T, H)} \Delta S_M(T, \Delta H) \tag{3.26}$$

Although Eq. (3.26) gives the idea of how the adiabatic temperature change is calculated instantaneously, the data that is obtained for Gd is that of the total entropy as a function of magnetic field intensity and temperature. Therefore, the concept is to find the same value of total entropy for 0 T and 0.875 T, and find the

corresponding values of the MCM temperature for each of these fields. The difference between those two temperature values gives the adiabatic temperature change.

To implement this concept in MATLAB, the temperature of the solid at the end of the Hot-to-Cold blow for each control volume is first obtained from the SIMULINK model. Then the entropy at that particular temperature is found using spline interpolation for the T-s curve for 0 T.

$$s_0 = s(B, T) = s(0, T_{s,end}) \tag{3.27}$$

Then using the value of entropy s_0, the temperature of the solid is found from the spline for the T-s curve for 0.875 T, after instantaneous magnetization.

$$T_s = T(B, s) = T(0.875, s_0) \tag{3.28}$$

Therefore, this value T_s is fed to the solid temperature array as the initial condition for the Cold-to-Hot blow. During the simulation of the Cold-to-Hot blow, the solid temperature at the end of this blowing process for each control volume is obtained and the entropy is obtained from the spline for the T-s curve for 0.875 T, since the material is magnetized during this blowing process.

$$s_{0.875} = s(B, T) = s(0.875, T_{s,end}) \tag{3.29}$$

Similarly, using the value of entropy $s_{0.875}$, the value of the solid temperature is obtained from the T-s curve for 0.875 T after instantaneous demagnetization.

$$T_s = T(B, s) = T(0, s_{0.875}) \tag{3.30}$$

The value of T_s is fed to the solid temperature array as the initial condition for the next cycle.

Switching between Hot-to-Cold and Cold-to-Hot blows
The switching of the blowing processes between the Hot-to-Cold and Cold-to-Hot blows is done on SIMULINK with the help of conditional switches. The switching is done control volume wise. This means that if the constant inlet temperature of the HTF at the hot side is the input for the first control volume for the Hot-to-Cold blow, then in case of the Cold-to-Hot blow, the output of the second control volume becomes the input for the first control volume. This happens for all the other control volumes. Similarly, the output of the twenty-ninth control volume is the input for the thirtieth control volume during the Hot-to-cold blow. But for the Cold-to-Hot blow, the constant inlet temperature of the HTF at the cold side is the input for the thirtieth control volume. Fig. 3.9 and Fig. 3.10 are snippets from the SIMULINK model that illustrate the switch between the outputs for the fluid flow between each control volume as per the blowing process.

The flow direction variable is initially created in SIMULINK before it is given a value in MATLAB of 1 or -1 depending on the blowing process. When the MATLAB script is used to run the SIMULINK model, the value of the flow direction variable is set in MATLAB equal to +1 or -1 for the Hot-to-Cold blow and Cold-to-Hot blow respectively. Fig. 3.8 is a snippet from the SIMULINK model that depicts the specification of the flow direction variable and its use for the switch block to switch the direction of flow.
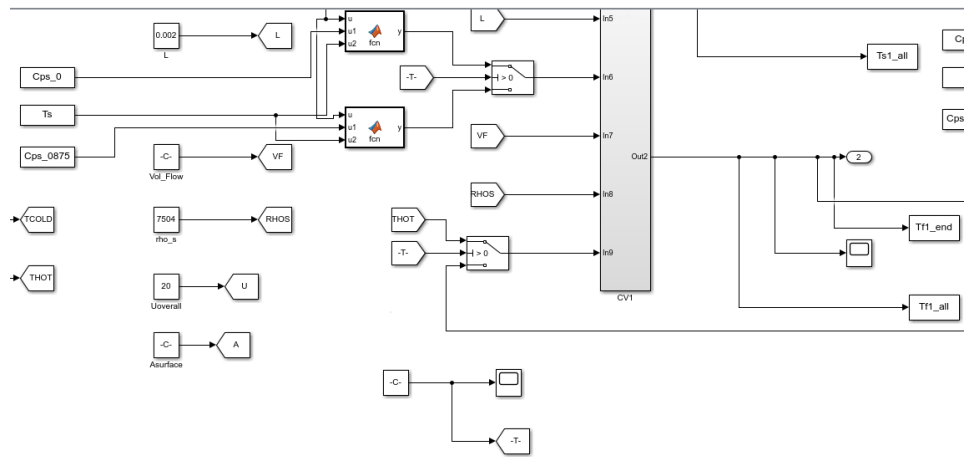
Figure 3.8: Illustration of the use of flow direction variable: The switch is used to change the direction of the flow depending on whether it is the Hot-to-Cold blow or Cold-to-Hot blow

As shown in Fig. 3.8, the flow direction variable block is given a tag with a certain label. This tag with the same label is specified as the condition for switching the flow direction depending on the blowing process. The condition is such that if the flow direction variable is greater than 0 (equal to 1), then the blowing process is Hot-to-Cold blow, otherwise the blowing process is Cold-to-Hot blow. The concept illustrated in Fig. 3.8 is applied to switch the flow of the fluid at the hot side and cold side according to the blowing process shown in Fig. 3.9 and Fig. 3.10 respectively.
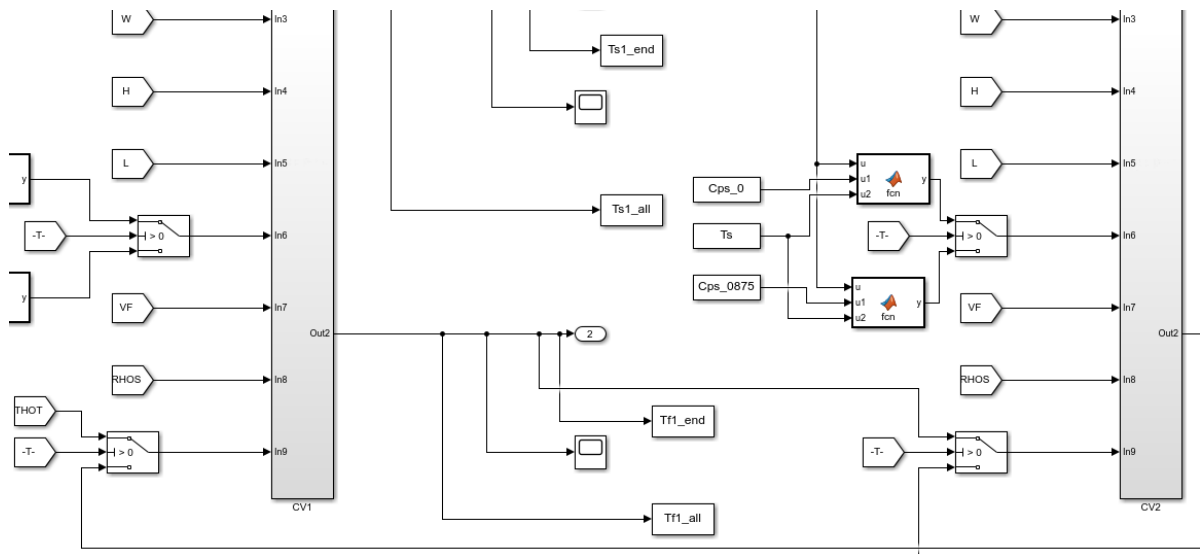
Figure 3.9: Illustration of flow switching for first 2 control volumes
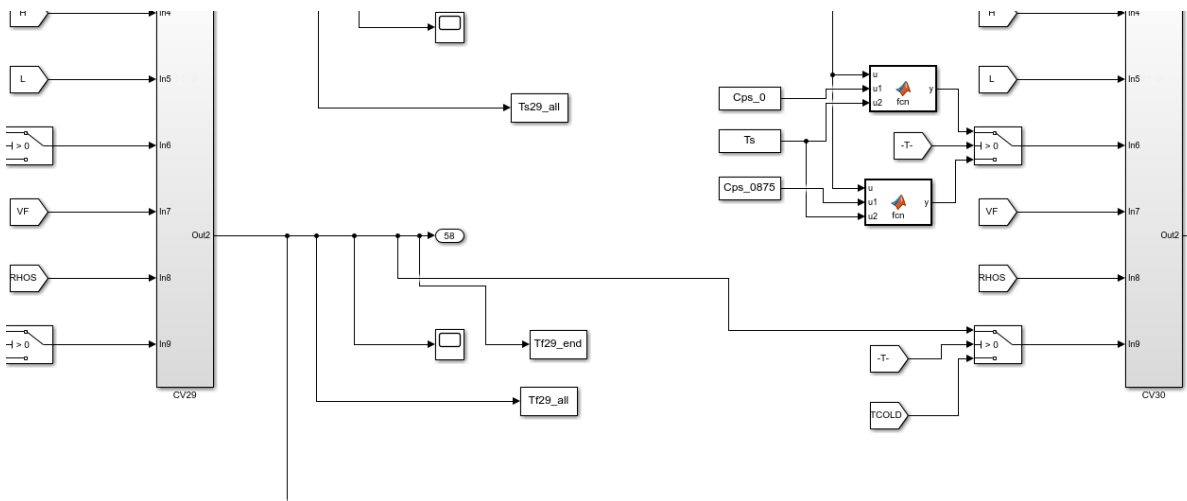
Figure 3.10: Illustration of flow switching for last 2 control volumes

From Fig. 3.9 and Fig. 3.10, it is clear that the condition provided is such that if the flow direction variable is equal to 1 then the Hot-to-Cold blow happens, which means that the output of the first control volume is the input for the second control volume and the output for the twenty-ninth control volume is the input for the thirtieth control volume. Similarly, if the value of the flow direction variable is -1, then the blowing process is Cold-to-Hot and the output of the second control volume is the input for the first control volume and the constant inlet HTF temperature at the cold side is the input for the thirtieth control volume. It is also noticed in Fig. 3.8, Fig. 3.9 and Fig. 3.10 that the MATLAB function for the specific heat capacity of the solid is that for no magnetic field during the Hot-to-Cold blow and the MATLAB function is switched to that for 0.875 T in case of the Cold-to-Hot blow. Therefore, the same condition for the flow direction variable being 1 and -1 is applied for the specific heat capacity MATLAB functions.

The overall complete magnetic heat pump cycle with the four stages is summarized in Fig. 3.11.
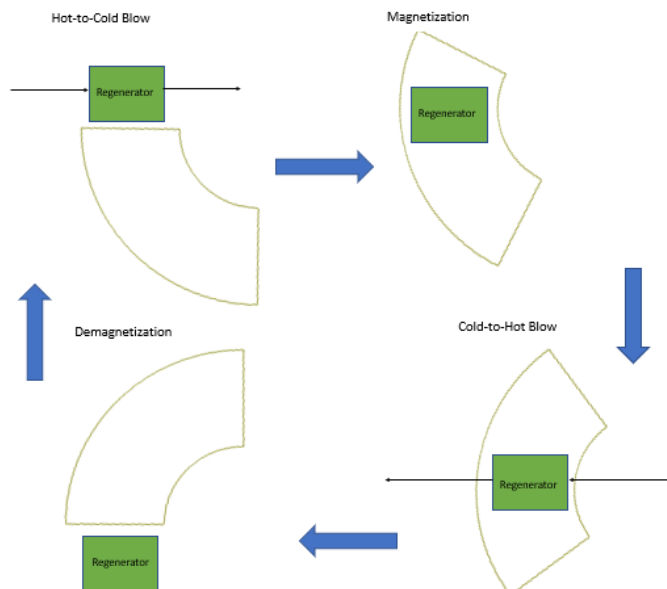
Figure 3.11: Complete Magnetic Heat Pump Cycle with the four stages: Hot-to-Cold blow, Magnetization, Cold-to-Hot blow and Demagnetization

3.4. Validation of the Model

The validation of the heat transfer model discussed in the previous chapter is done by comparing the results of this model with the experimental results reported by Huang et al. (2019) [18]. These authors reported the experimental results for three different sets of operating conditions. Each set had a different cycle frequency and a different volumetric flow rate corresponding to each frequency. The set that is chosen for comparison and validation is that with a cycle frequency of 1.7 Hz and a volumetric flow rate of 4.34 l/min. As discussed previously in this chapter, the number of valves open for the full volumetric flow rate is 4. Therefore, for one blowing process, the number of regenerators into which the flow rate is split is 4 and for the other blowing process it is 3, since the total number of regenerators is 7. Therefore the total volumetric flow rate of 4.34 l/min is considered to split into 3.5 regenerators at a time, such that each regenerator receives 3.5 times less than the total flow rate during one blowing process. The corresponding volumetric flow rate that one regenerator receives is $2.067 * 10^{-5}$ $m^3 s^{-1}$ and is treated as a constant throughout the cycle operation. If the cycle frequency is 1.7 Hz, then the total time for the cycle, i.e. for the Hot-to-Cold blow and Cold-to-Hot blow, is given by Eq. (3.31):

$$t = 1/F = 1/1.7 = 0.58 \ s \tag{3.31}$$

Therefore, if the total cycle time is 0.58 s, then it is safe to divide the time by 2 to obtain 0.29 s for the Hot-to-Cold blow and the Cold-to-Hot blow respectively, since the instantaneous magnetization and demagnetization are implemented in the model. These values are implemented wherever required in the SIMULINK model.

To compare the results of the SIMULINK model with the experimental data, the parameter that is chosen is the average cooling capacity. The graphs for the average cooling capacity against temperature span are obtained for the parameters corresponding to the group for which the frequency is 1.7 Hz.

The temperature of the HTF at the hot side is kept constant by Huang et al. (2019) [18] at 295 K or 21.85°C. This is because for another set of experiments conducted by the authors, the maximum temperature span for zero load was achieved when the hot side temperature was 295 K. Therefore, for expanding the temperature span and obtaining the curve for the temperature span as a function of average cooling capacity, the temperature of the HTF at the hot side is kept constant while the temperature of the HTF at the cold side is changed to obtain the corresponding average cooling capacity. These values are constants that are fed at either end of the regenerator in the SIMULINK model as is depicted in Fig. 3.9 and Fig. 3.10. Therefore, only 1 regenerator is used in the SIMULINK model instead of 7 regenerators, for modelling the heat transfer, since each regenerator will receive the same HTF temperature at the hot side and cold side at its corresponding ends.

Eq. (3.32) is applied in order to obtain the cooling capacity or cooling power (in W) at any point in time during the cycle time:

$$\dot{Q}_{cold} = \dot{m} * c_{p,f} * (T_{f,cold} - T_f) \tag{3.32}$$

This equation is implemented in the SIMULINK model in the last control volume, since that is the cold side. T_f is the transient temperature of the HTF leaving the last control volume and $c_{p,f}$ is obtained as a function of T_f. The mass flow rate $\dot{m}$, is obtained by multiplying the volumetric flow rate with the density of the HTF at the temperature $T_{f,cold}$ which corresponds to the constant cold side HTF temperature. Therefore, the continuously changing cooling capacity is obtained as the simulation is run for 100 complete AMR cycles by providing this value in the MATLAB code. The average cooling capacity is not obtained at a particular instant of time. The average cooling capacity is obtained as an average value over one cycle, which is usually towards the end of the simulation wherein periodic steady-state is achieved. Therefore, the hundredth cycle of simulation is chosen to obtain the average cooling capacity. Since the cooling capacity of an AMR is only relevant during one blowing process which, in this case, is the Hot-to-Cold blow, this average value is taken only for the first 50 time steps during the Hot-to-Cold blow, but divided by two to obtain the cooling capacity over the entire cycle.

Although the volumetric flow rate is considered to be a constant value of $2.067 * 10^{-5}$ $m^3 s^{-1}$, the volumetric flow rate profile as a function of the rotation angle of the permanent magnet is not a constant value in reality. There are many possible profiles of the volumetric flow rate as a function of the rotation angle. One such possible profile that is considered in the model and is closer to the actual volumetric flow rate profile is shown in Fig. 3.12.
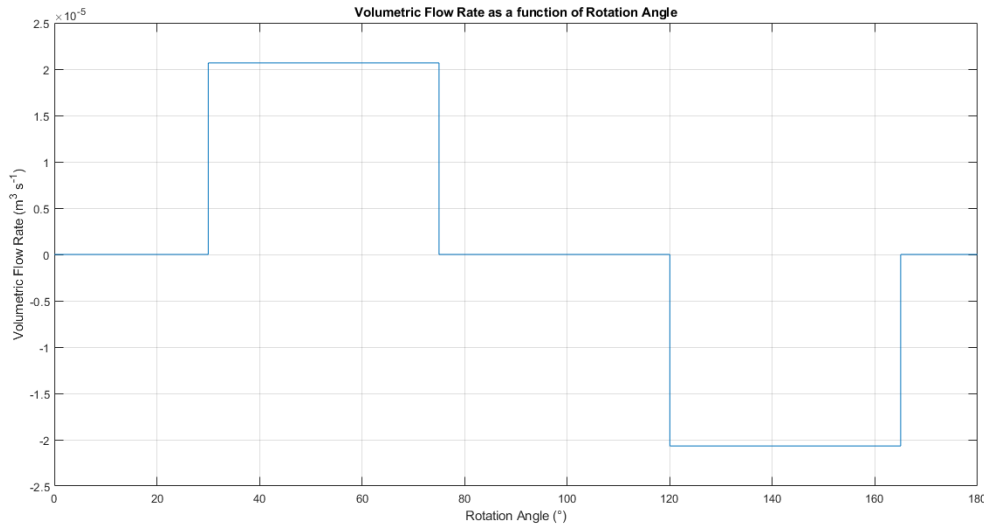
Figure 3.12: Volumetric Flow Rate Profile [18]: This profile is one of the profile that represents a closer version of the actual volumetric flow profile

For each AMR cycle, one permanent magnet completes half a rotation, which means an angle of $180°$. Therefore, a rotation of $90°$ corresponds to half of one cycle. From Fig. 3.12, it is noticed that there is flow rate only from an angular rotation of $30°$ to $75°$ for the first half of the cycle and an angular rotation of $120°$ to $165°$ for the second half of the cycle. This corresponds to an angular distance of $45°$ during each half of the cycle. Therefore, there is flow only during half the time for one blowing process, since each half of the cycle is considered to be one blowing process. Hence, in order to follow this flow profile, the average cooling capacity that is obtained for one regenerator is halved. The resultant cooling capacity is then multiplied by 7 to obtain the maximum cooling capacity for all the 7 regenerators of the regenerator system.

To implement this in the MATLAB code, each blowing process during one cycle is run for one fourth of one full cycle time. Therefore, if the time for one full cycle is 0.58 s, then the SIMULINK model is run using the MATLAB code for one fourth that time, which is 0.145 s. To summarize the actual approach used for calculating the average cooling capacity for the complete regenerator system, Eq. (3.33) is used to implement the approach in MATLAB:

$$\dot{Q}_{cold} = 7 * (\frac{1}{t_{cycle} * nt})(\sum_{n=1}^{nt} \dot{m} * c_{p,f} * (T_{f,cold} - T_f^n)) * t_{simu} \tag{3.33}$$

where:
nt = No. of time steps during one blowing process = 50
t_{cycle} = Total time for one cycle = 0.58 s
t_{simu} = Total time for one blowing process = 0.145 s.

It is to be noted from Eq. (3.33) that the average is taken over 50 to imply the 50 time steps that are considered only for the Hot-to-Cold blow.

After the simulation, the results of the average cooling capacity are obtained for different temperature spans (obtained by changing the cold side HTF temperature, keeping the hot side HTF temperature constant). The comparison of the two graphs that are obtained from the simulation as well as the experimental data are given in Fig. 3.13.
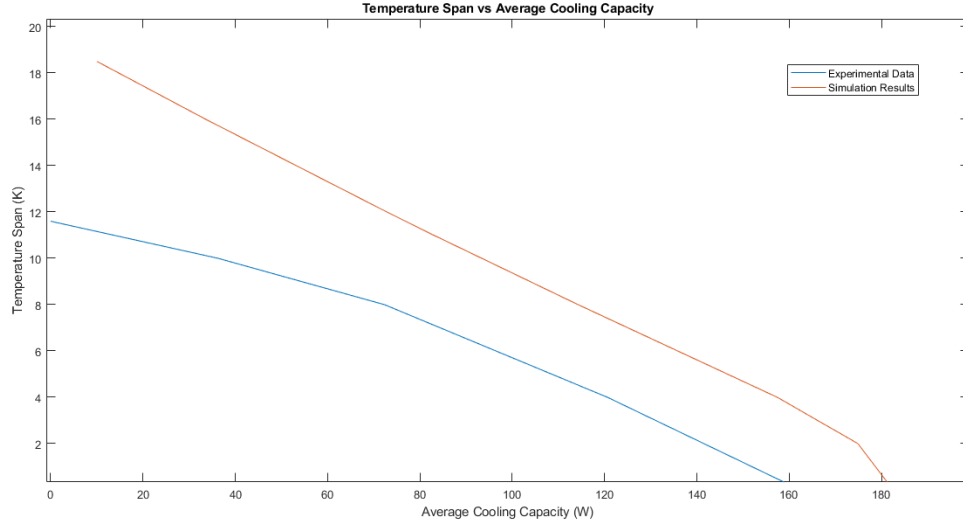
Figure 3.13: Temperature span vs average cooling capacity for comparison. The average cooling capacity obtained from the simulation is much larger than that obtained from the experimental data

The plots in Fig. 3.13 show a large difference between the cooling capacity of the simulation and the experimental data. This is because not enough heat loss mechanisms are considered in the simulation model. The difference between the temperature span of the simulation and the experimental data for a particular value of cooling capacity increases with decrease in the cooling capacity. Since the required trend of decreasing cooling capacity with increasing temperature span is maintained for the simulation, the model is considered valid for further analysis.

3.5. Performance Parameters

The performance parameters of the heat pump cycle are obtained and the temperature span is calculated as a function of these parameters using the improved heat transfer model. The performance parameters that are obtained are average heating capacity and the calculated COP, since they are relevant to the project for delivering the required heat to the heat sink using the heat pump.

3.5.1. Average Heating capacity of the Heat Pump

The average heating capacity is an important parameter for the heat pump relevant to the project, since it helps in indicating whether the heat pump can provide the required heat to the heat sink. The heating capacity is calculated using the same approach as that for the average cooling capacity. However, the equation that is used is slightly different from that for the cooling capacity. In case of Eq. (3.33) for the cooling capacity, the temperature difference is calculated by subtracting the transient HTF temperature from the constant HTF temperature at the cold side. However, in case of the heating capacity, the temperature difference is obtained by subtracting the constant HTF temperature at the hot side from the transient HTF temperature.

$$\dot{Q}_{hot} = 7 * (\frac{1}{t_{cycle} * nt})(\sum_{n=1}^{nt} \dot{m} * c_{p,f} * (T_f^n - T_{f,hot})) * t_{simu} \tag{3.34}$$

There is another important difference between the calculation of the heating capacity and the cooling capacity. In case of the cooling capacity, the calculation is made by taking the average of only the Hot-to-Cold blow for the entire cycle, since the cooling capacity is relevant during this blowing process. But in case of the heating capacity, the average is taken over the entire cycle but only for the Cold-to-Hot blow, since the heating capacity is relevant during this blowing process. After obtaining the average heating capacity for different temperature spans, the plot for the temperature span as a function of the average heating capacity is created as shown in Fig. 3.14.
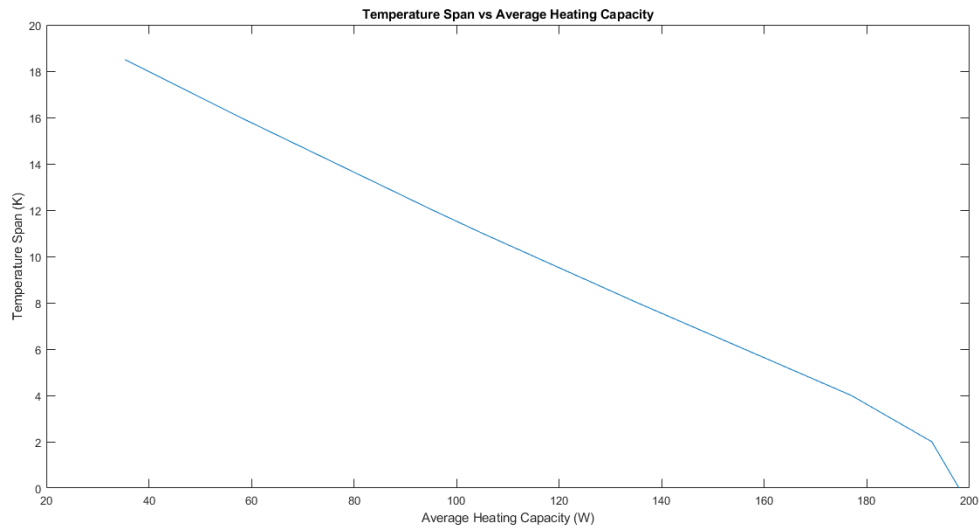
Figure 3.14: Temperature span vs Average Heating capacity

The plot in Fig. 3.14 shows that the temperature span as a function of average heating capacity follows the same trend as that for average cooling capacity. The zero load temperature span in this case is close to 20 K, and the average heating capacity at zero temperature span is around 197 W.

3.5.2. Coefficient of Performance (COP)
The second parameter that is obtained for the heat pump is the calculated COP. Since the objective is to deliver a certain amount of thermal power to a heat sink, the COP that is obtained is that for heating. Eq. (3.35) is used to calculate the heating COP using the values of cooling capacity and heating capacity obtained previously.

$$COP = \frac{\dot{Q}_{hot}}{\dot{Q}_{hot} - (\dot{Q}_{cold} + \dot{Q}_{loss})} \qquad (3.35)$$

Using Eq. (3.35), the COP is obtained for different temperature spans, in order to create the plot for the temperature span as a function of heating COP as shown in Fig. 3.15.
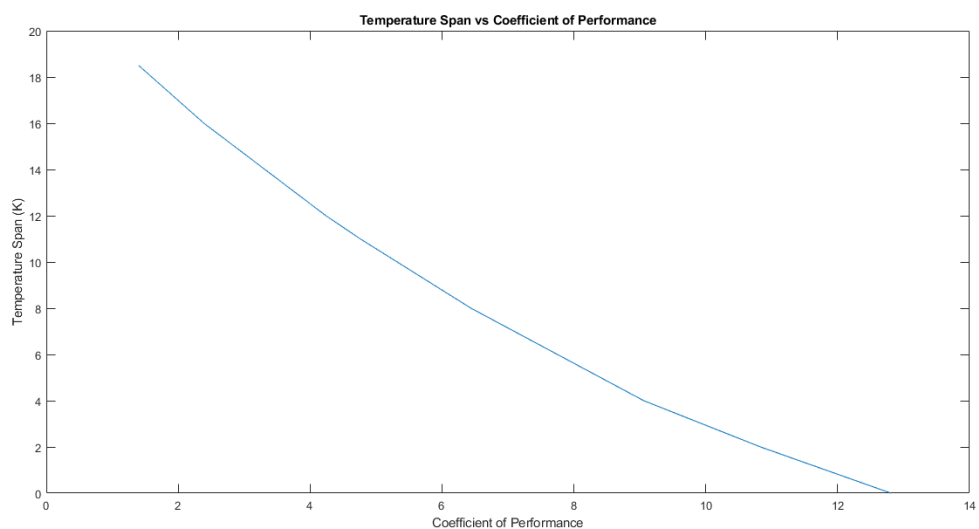
Figure 3.15: Temperature span vs Coefficient of Performance

From Fig. 3.15, it can be deduced that the COP increases with a decrease in temperature span. This trend is expected since the heating capacity increases with a decrease in temperature span, and also because, the difference between the heating capacity and the cooling capacity increases with increase in temperature span. The maximum COP is achieved at zero temperature span and its value is 12.81.

For further validation of the model, the heating COP is plotted as a function of cooling capacity and is shown in Fig. 3.16.
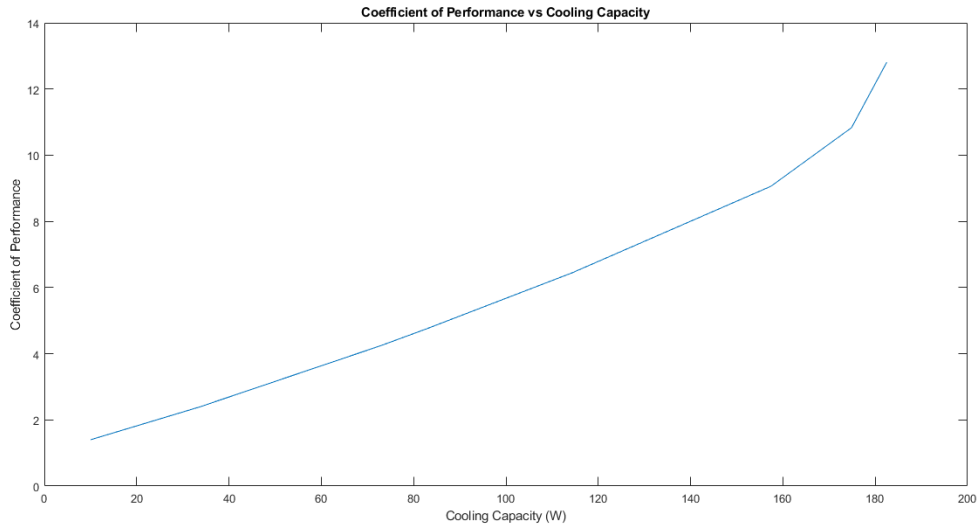
Figure 3.16: Heating COP as a function of cooling capacity

Fig. 3.16 suggests that the heating COP increases with increase in cooling capacity. The plot of heating COP as a function of cooling capacity is helpful in understanding the performance trend and determining whether the model is valid or not, however, for better validation, the cooling COP is obtained as a function of cooling capacity, since the cooling COP was obtained as a function of cooling capacity by Huang et al. (2019) [18]. Therefore, plots of cooling COP as a function of cooling capacity as per the simulation and the experimental data by Huang et al. (2019) [18] are compared in Fig. 3.17.
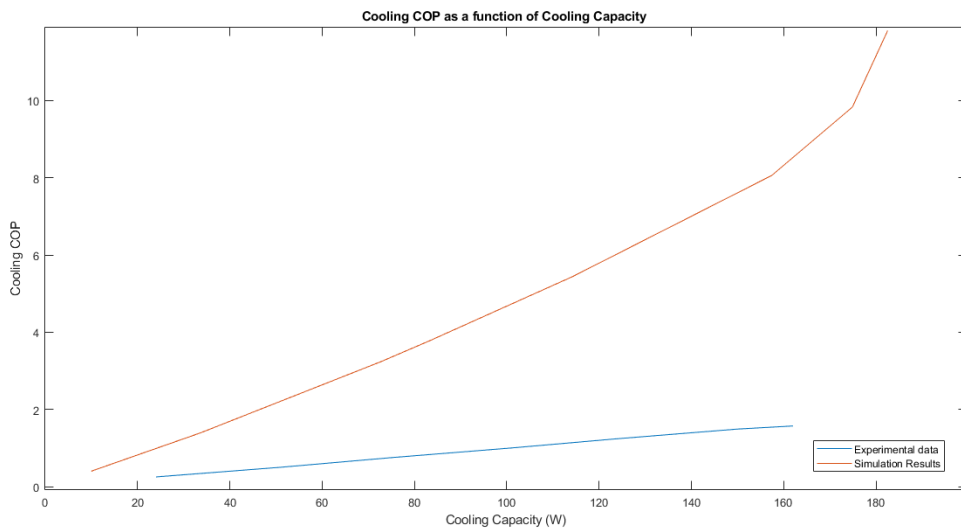
Figure 3.17: Cooling COP as a function of cooling capacity for simulation and experimental data [18]: The cooling COP obtained from the simulation is much larger than that obtained from the experimental data.

The plots in Fig. 3.17 show similar trends, meaning that the cooling COP increases with increase in cooling capacity in each case. However, the values of cooling COP for the simulation are much larger than those for the experimental data. This is because, the heat losses that are not considered are the dead volumes, bypass flow and the likes. Another reason that can be attributed to the high COP is that the thermal conduction term for the solid and fluid in which the temperature has a second-order dependence on distance is not considered in the energy balance. Although, this is justified by the fact that the thermal conductivity of the HTF is low, and that the model complexity increases, it may have an impact in the heat transfer between the solid and the HTF, resulting in a change in COP. The cooling COP is calculated by simply subtracting 1 from the calculated heating COP. Therefore, the work that is considered to be done is only that from the adiabatic magnetization. The work done by the other components of the heat pump like the pump for fluid flow and valve operation is not considered in the model. Therefore, this can also contribute to the high COP obtained in Fig. 3.17.

Therefore, the plots from Fig. 3.13 to Fig. 3.17 suggest that the model that has been developed for the regenerator is highly optimistic compared to the experimental data. However, since the required trend is achieved in each of the plots, this model is used for the sensitivity analysis discussed in Chapter 4.

4

Results and Discussion

4.1. Sensitivity Analysis

The sensitivity analysis is carried out in order to analyze how certain parameters of the AMR heat pump influence its performance. The performance of the AMR device is judged through its temperature span as a function of cooling capacity, heating capacity and COP. The parameters that are used for this sensitivity analysis are those that can measurably impact the performance of the device. These parameters are the diameter of the Gd particles, the porosity, frequency of the cycle and the heat transfer coefficient for losses to the environment. While one of the parameters of the regenerator is varied to analyze the performance, the other parameters are maintained at the original values that are used for obtaining the performance parameters discussed in the previous chapter. The original values of the regenerator parameters are listed in Table 4.1 before undergoing changes.

Table 4.1: Original Properties of Regenerator Parameters

Property	Value
Diameter of Gd Particles (m)	0.0006
Porosity	0.36
Cycle Frequency (Hz)	1.7
Heat transfer coefficient for losses (W m$^{-2}K^{-1}$)	20

4.1.1. Diameter of the Gd Particles

In this part of the sensitivity analysis, the influence of the diameter of the Gd spherical particles over the performance of the AMR device is analyzed. This parameter is chosen for the sensitivity analysis as it influences the specific surface area for heat transfer. The diameter of the spherical particles can be varied from 0.0004 m to 0.0008 m. The other parameters like the porosity, frequency and the loss heat transfer coefficient are kept constant while changing the diameter of the particle. Fig. 4.1 shows the plots for temperature span as a function of cooling capacity for the simulated AMR model for different particle diameters.
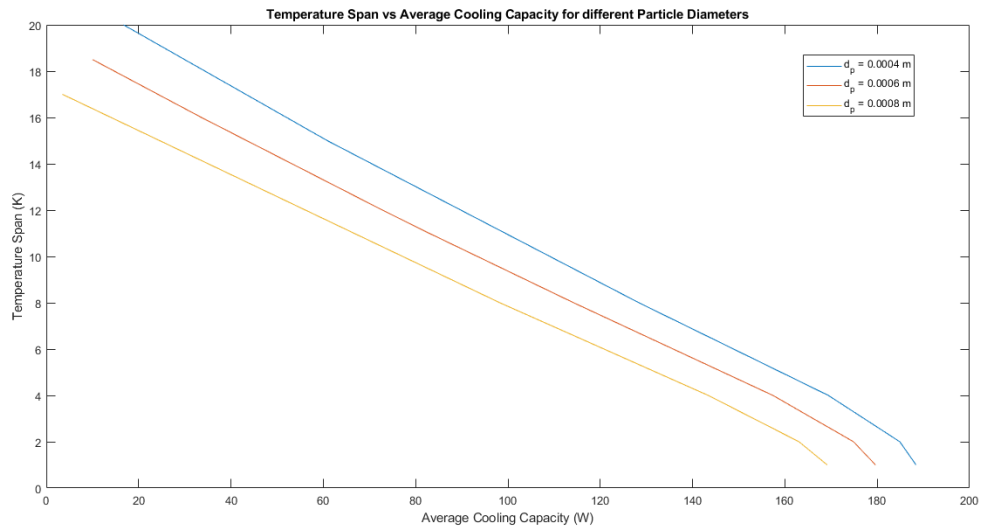
Figure 4.1: Sensitivity analysis with particle diameter for cooling capacity. For a particular temperature span, the average cooling capacity increases with decrease in particle diameter.

The plots in Fig. 4.1 suggest that the average cooling capacity and the temperature span increase with decrease in particle diameter. This can be attributed to the fact that by decreasing the particle diameter, the specific surface area increases, thereby providing more heat transfer surface area per unit volume.

Similar plots are made for the temperature span as a function of heating capacity for different particle diameters as shown in Fig. 4.2.
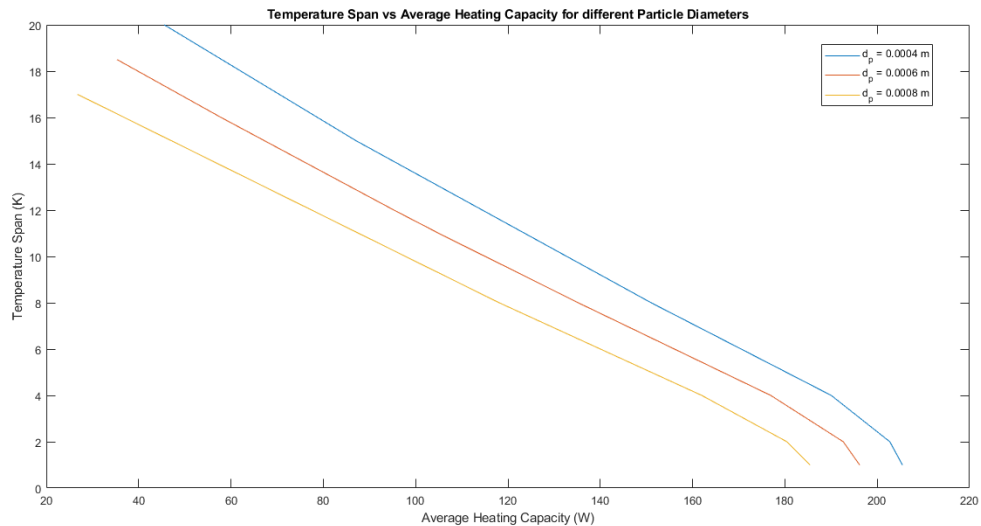
Figure 4.2: Sensitivity analysis with particle diameter for heating capacity: For a particular temperature span, the average heating capacity increases with decrease in particle diameter.

A similar trend is observed in the plots of Fig. 4.2 when compared to the plots in Fig. 4.1. There is an increase in average heating capacity and the temperature span with a decrease in the particle diameter. This is also due to the increase in specific surface area for heat transfer.

The sensitivity analysis with the particle diameter is complete for plotting the temperature span as a function of the heating COP for different values of the diameter. The plots are shown in Fig. 4.3.
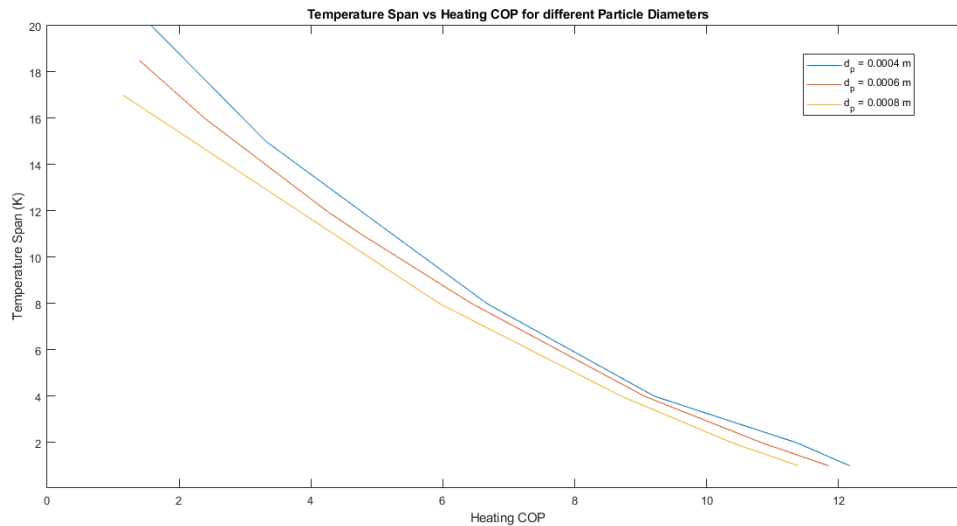
Figure 4.3: Sensitivity analysis with particle diameter for heating COP: For a particular temperature span, the heating COP increases with decrease in particle diameter.

It is observed in Fig. 4.3 that the COP decreases with an increase in temperature span for all particle diameters. But, the COP increases with decrease in particle diameter. This is because of the more specific surface area for heat transfer between the HTF and the solid. Therefore, the heat exchange between the HTF and the solid is higher than the work done during magnetization.

4.1.2. Porosity of the Regenerator Packed Bed

This part is focused on the influence that the porosity of the packed bed regenerator has on the performance of the system. This parameter is chosen because it has an influence on the mass of the solid MCM and the HTF in the packed bed at a particular instant of time. Therefore, it may have an impact in the transient temperature response of the system. It also influences the velocity of the flow and therefore it can have a measurable impact on the convective heat transfer coefficient. The porosity can be varied between 0.3 and 0.5. The porosity is changed keeping the other parameters constant. Fig. 4.4 shows the plots for the temperature span as a function of cooling capacity for different values of porosity.
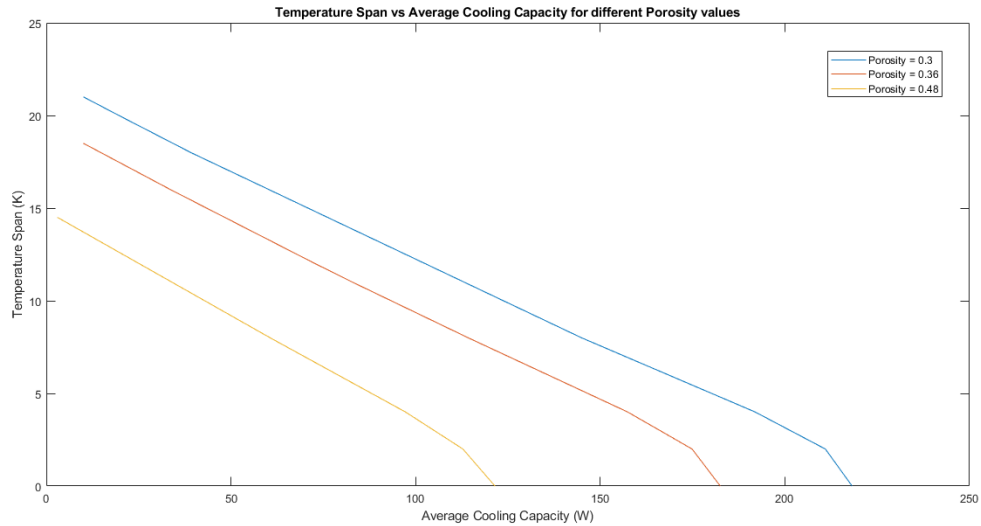
Figure 4.4: Sensitivity analysis with porosity for cooling capacity: For a particular temperature span, the average cooling capacity increases with decrease in porosity.

The plots in Fig. 4.4 indicate that a decrease in porosity results in an increase in the average cooling capacity and the temperature span. This can be attributed to the fact that for a constant volumetric flow rate and cross section area of the packed bed regenerator, a decrease in porosity results in an increase in the fluid flow velocity, resulting in a increase in the convective heat transfer coefficient. Another way of reasoning is that the decrease in porosity results in an increase of MCM for a given bed volume. An increase in the solid mass may result in an increase of the overall energy stored due to the MCE.

The plots for temperature span as a function of heating capacity for varying porosity are given in Fig. 4.5.
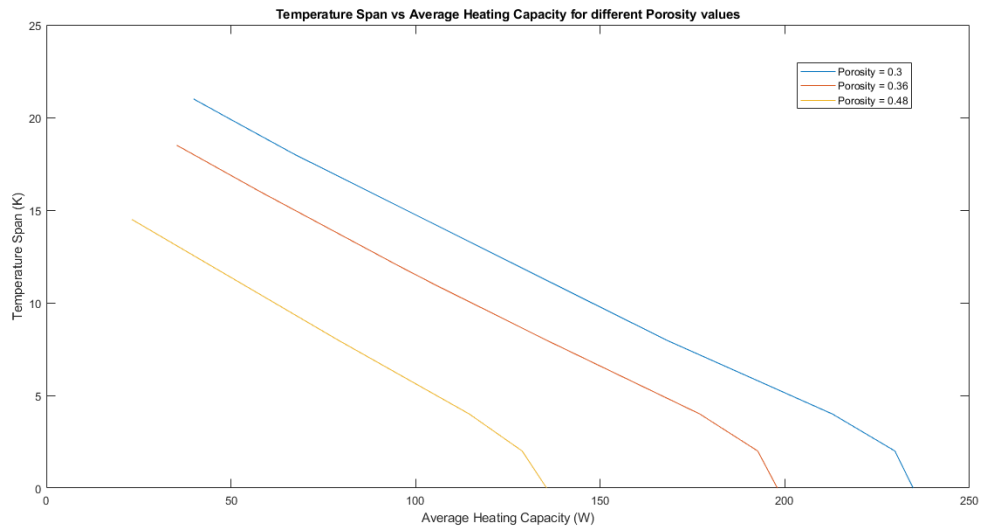
Figure 4.5: Sensitivity analysis with porosity for heating capacity: For a particular temperature span, the average heating capacity increases with decrease in porosity.

From Fig. 4.5, it is deduced that decreasing the porosity increases the average heating capacity and the temperature span of the AMR device quite significantly. This can also be attributed to the increase in MCM for a given bed volume with an increase in porosity and an increase in the fluid velocity for a decrease in porosity for constant volumetric flow rate and area of cross section.

The temperature span as a function of the heating COP is plotted for varying porosity in Fig. 4.6.
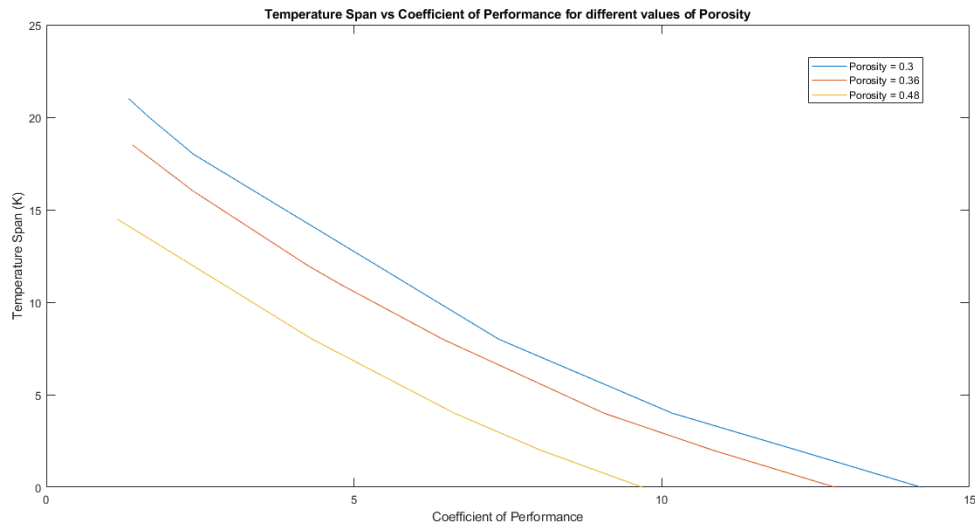
Figure 4.6: Sensitivity analysis with porosity for COP: For a particular temperature span, the heating COP increases with decrease in porosity.

The plots in Fig. 4.6 suggest that the COP increases with a decrease in porosity of the regenerator. The maximum COP is obtained at zero temperature span and for a porosity of 0.3, with a value of 14.21. The change in COP with porosity is also quite significant, suggesting that the porosity has a major impact in the performance of the AMR device.

4.1.3. Frequency of the cycle

The frequency of the cycle is the parameter whose influence on the performance of the regenerator is analyzed in this part. This parameter is chosen since it can influence the temperature that the solid and the HTF attain at the end of each blowing process, and therefore, influences the performance of the regenerator. The other parameters are kept constant as the cycle frequency is varied. Along with the frequency, the volumetric flow rate is also varied, such that the utilization is kept constant. The utilization is defined by Eq. (4.1).

$$UT = \frac{\rho_f * c_{p,f} * \dot{V}}{F * m_s * c_{p,s}} \tag{4.1}$$

Therefore, if the utilization is to be constant then, the volumetric flow rate is varied in direct proportion to the cycle frequency.

Fig. 4.7 shows the plots for the temperature span as a function of average cooling capacity for the simulated model for different frequencies.
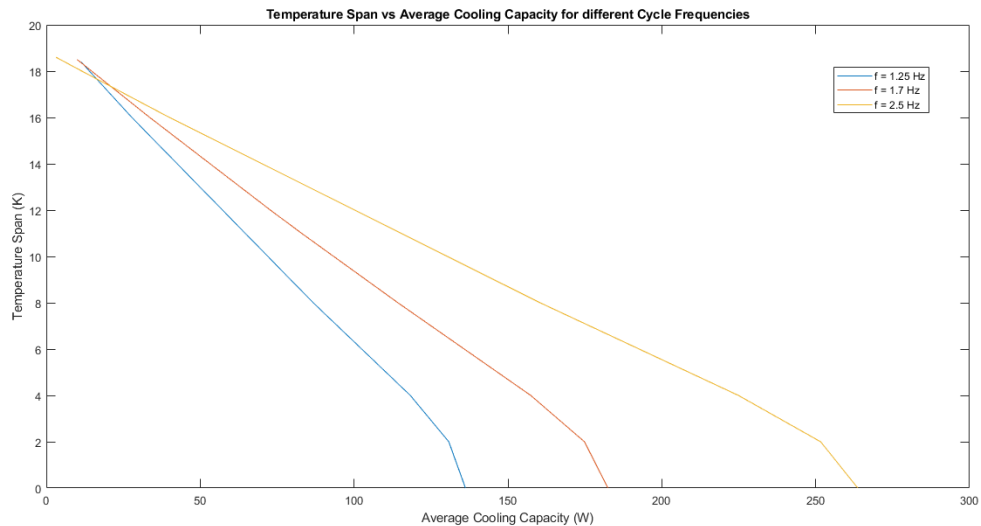
Figure 4.7: Sensitivity analysis with frequency for cooling capacity: For a temperature span lower than 18 K, the average cooling capacity increases with an increase in cycle frequency.

Fig. 4.7 indicates that on increasing the frequency of the cycle, the average cooling capacity and temperature span of the AMR device increase. This is because there is less blowing time for a process which means there is less heat loss from the HTF to the surroundings through the casing during each blowing process. Another way of reasoning this trend is the higher volumetric flow rate being used for higher frequency for constant utilization. This results in higher convective heat transfer coefficient. The frequency has a high impact on the average cooling capacity, except for higher temperature spans.

The temperature span as a function of heating capacity is plotted for different values of cycle frequency and is shown in Fig. 4.8.
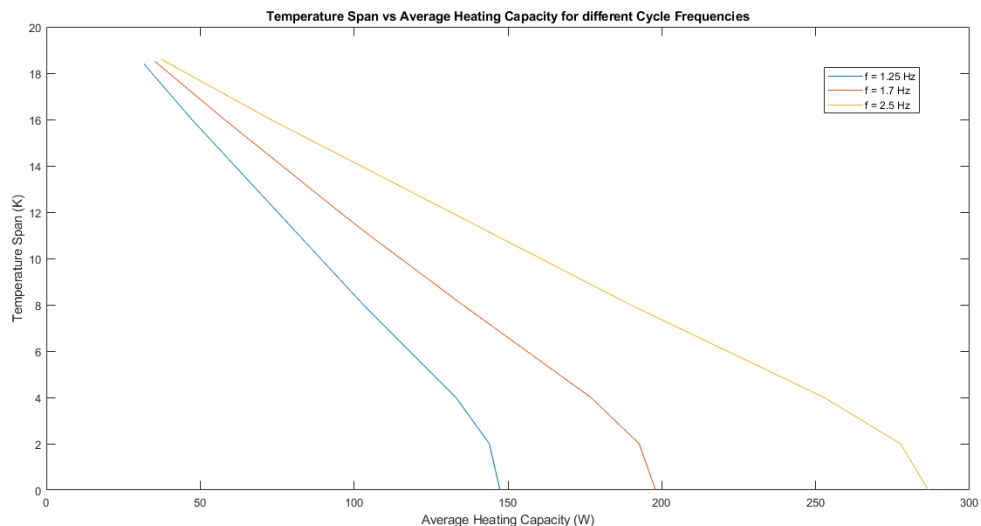
Figure 4.8: Sensitivity analysis with frequency for heating capacity: For a temperature span lower than 18 K, the average heating capacity increases with an increase in cycle frequency.

The general trend in the plots of Fig. 4.8 is that the average heating capacity increases with an increase in cycle frequency. This is also attributed to the fact that the blowing time is less for higher frequencies, meaning that there is reduced heat loss from HTF to the surroundings through the casing, during each blowing process. The frequency has a high impact on the average heating capacity, except for higher temperature spans.

The plots for temperature span as a function of heating COP for varying cycle frequency are shown in Fig. 4.9.
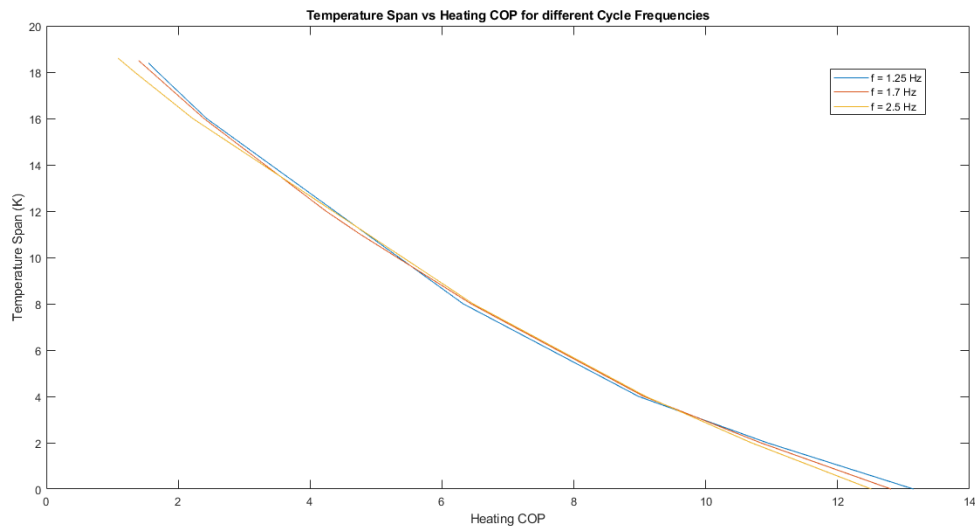
Figure 4.9: Sensitivity analysis with frequency for COP: The change in COP is not significant for a change in cycle frequency.

From Fig. 4.9, the general trend that is seen is that a lower frequency gives a higher COP. This can be attributed to the fact that there are more magnetization processes during a given time for higher cycle frequencies, therefore, the work done is more and the COP is lower. It is also evident from Fig. 4.9 that the cycle frequency does not impact the COP as significantly as the heating or cooling capacity. The maximum COP is obtained at zero temperature span for a frequency of 1.25 Hz, and its value is 13.15.

4.1.4. Heat losses

The heat losses to the environment through the regenerator casing is considered as another parameter for the sensitivity analysis. This is because, it changes the temperature of the HTF, thereby affecting its performance. This is done by developing plots for the temperature span as a function of the different performance parameters for different values of the heat loss coefficient.

The plots for temperature span as a function of cooling capacity is developed for different values of heat loss coefficient and are shown in Fig. 4.10.
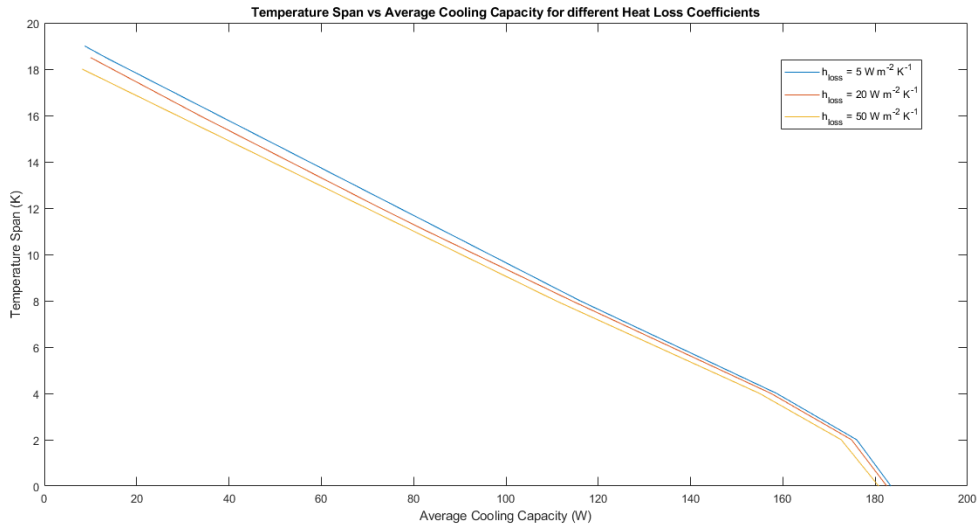
Figure 4.10: Sensitivity analysis with heat losses for cooling capacity: Cooling capacity decreases with increase in heat loss coefficient

From Fig. 4.10, it is evident that the average cooling capacity and the temperature span decrease with increase in the heat loss coefficient, with the trend not being very measurable. This is because the heat loss is actually heat addition to the HTF from the environment, which results in an increase in HTF temperature, hence, a reduction in cooling capacity.

The plots are made for temperature span as a function of heating capacity for varying heat loss coefficient, shown in Fig. 4.11.
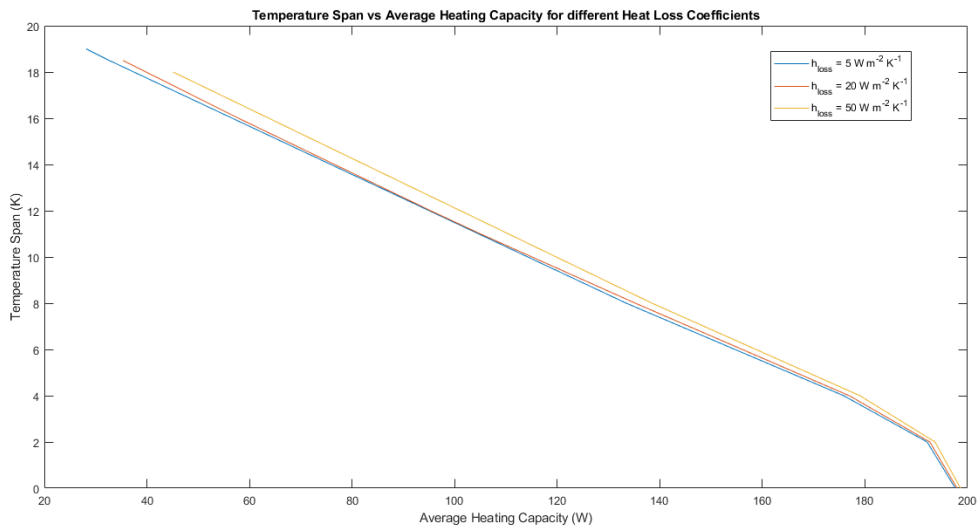
Figure 4.11: Sensitivity analysis with heat losses for heating capacity: Heating capacity increases with increase in heat loss coefficient

The plots in Fig. 4.11 indicate that the average heating capacity slightly increases with the increase in heat losses. This is due to the fact that the heat losses are heat addition, resulting in an increase in HTF temperature and thereby, an increase in the heating capacity of the device.

The plots in Fig. 4.12 are for the temperature span as a function of heating COP for different values of heat loss coefficient.
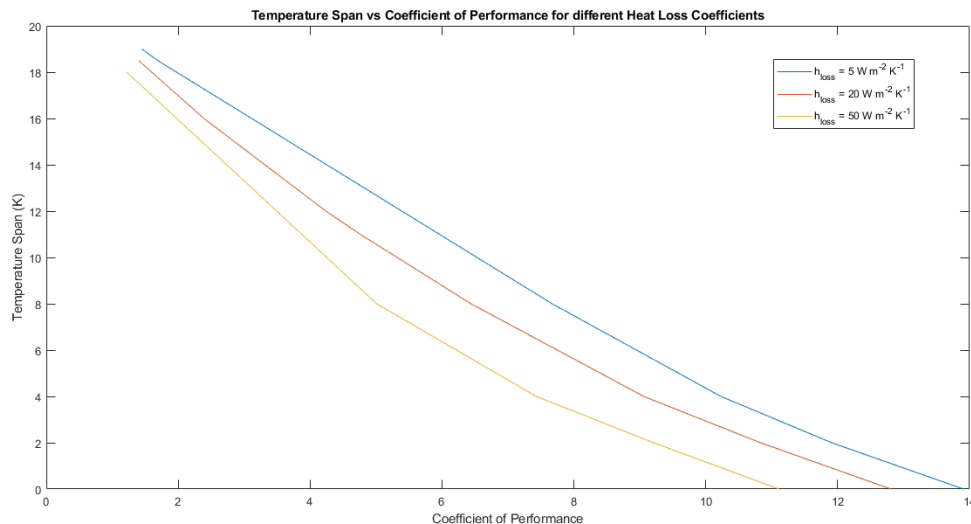
Figure 4.12: Sensitivity analysis with heat losses for COP: Heating COP increases with decrease in heat loss coefficient.

The plots in Fig. 4.12 indicate that the general trend is a decrease in the heating COP with an increase in heat losses. This is because, with increase in heat losses, the magnitude of the heating capacity increases while the magnitude of the cooling capacity decreases. Therefore, the difference between the heating capacity and cooling capacity increases, resulting in a decrease in COP. The maximum COP is obtained for zero temperature span and a heat loss coefficient of 5 $Wm^{-2}K^{-1}$. It has a value of 13.91.

4.2. Temperature distribution for the HTF at different stages of one cycle

The temperature variation in the HTF is analyzed along the length of the regenerator for different stages of one cycle. The cycle that is chosen for analysis is the hundredth cycle of simulation, since periodic steady state is achieved at this point. Three stages of the cycle are chosen for analysis: The beginning of the hundredth cycle, the end of the Hot-to-Cold blow (one half of the cycle) and the end of the Cold-to-Hot blow (completion of one cycle). This analysis is done for the original values of the regenerator parameters before the sensitivity analysis and for a temperature span of 8 K. Fig. 4.13 is the plot for the HTF temperature along the regenerator length for the two stages of the hundredth cycle.
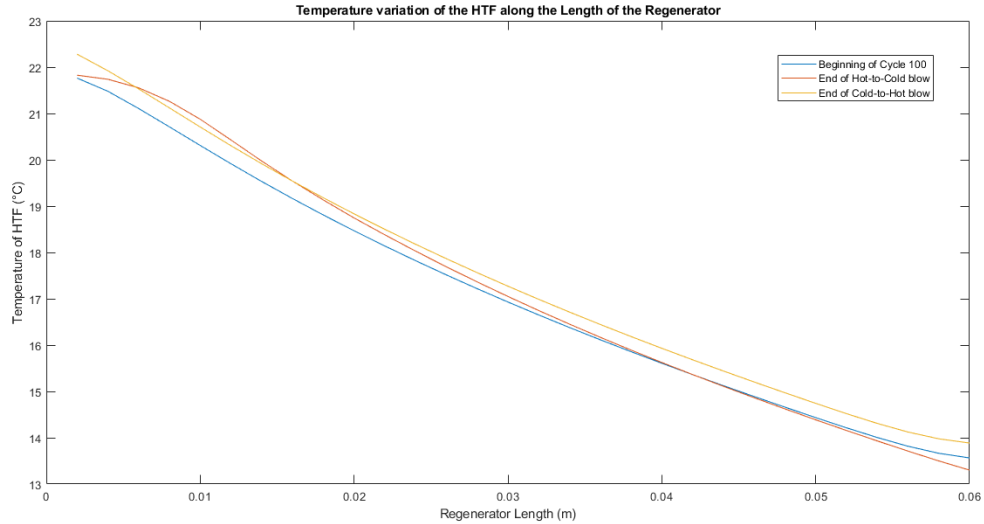
Figure 4.13: Temperature variation of the HTF along the regenerator length. Three stages of the cycle are depicted: The beggining of the cycle, the end of the first blowing process (Hot-to-Cold blow) and the end of the cycle (End of Cold-to-Hot blow)

In Fig. 4.13, it is seen that the temperature of the HTF at the cold side of the regenerator (0.06 m) is at a temperature lower than the constant temperature at the cold side (13.85°C) at the end of the Hot-to-Cold blow. This means that the heat source is working properly, giving heat to the HTF flowing through it. Similarly, at the end of the Cold-to-Hot blow, the temperature of the HTF at the hot side (0.002 m) is at a temperature higher than the constant temperature at the hot side (21.85°C). This means that the heat sink is working properly taking away heat from the HTF flowing through it. It is also noticed in Fig. 4.13 that there are some certain instants of time, wherein the magnitude of the difference between the constant temperature of the hot side and the temperature of the HTF at the hot side is less than that between the constant temperature at the cold side and the HTF temperature at the cold side. Even if this is the case, the average magnitude in this difference is higher for the hot side than the cold side, suggesting a higher heating capacity than cooling capacity predominantly.

4.3. Transient temperature response of HTF and Solid Regenerator in one control volume during Simulation

The transient temperature response of the HTF and the solid are shown for the last control volume (cold side) for the simulation of 25 cycles to illustrate the type of profile that is obtained when the flow is switched after magnetization or demagnetization depending on the process. The original conditions of the regenerator before the sensitivity analysis with a temperature span of 8 K are used to obtain the plot for the HTF shown in Fig. 4.14.
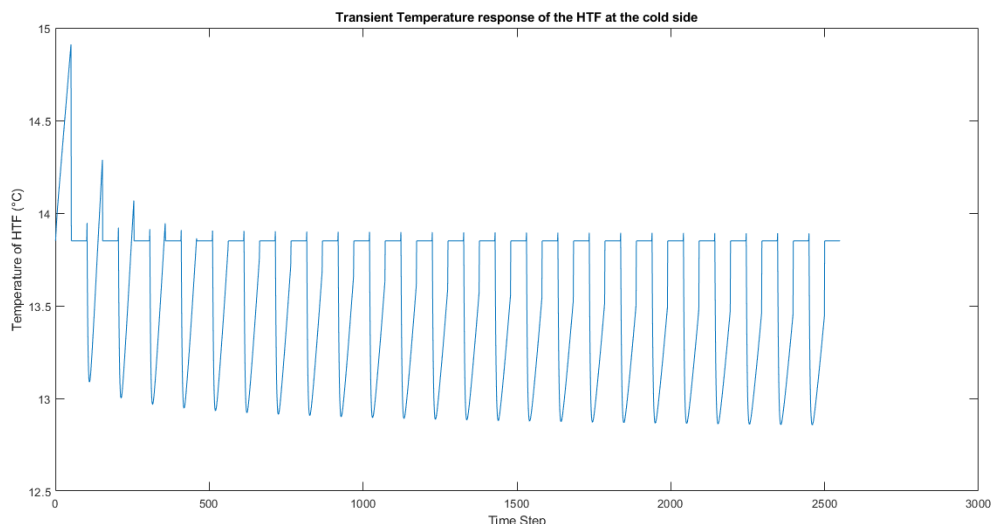
Figure 4.14: Transient temperature response of the HTF at the cold side: The horizontal lines depict that the Cold-to-Hot blow is not considered for obtaining this plot, since it is not relevant for the cold side.

The x-axis of the plot shown in Fig. 4.14 is the number of time steps in the entire simulation. As is discussed in previous chapters, each blowing process consists of 50 time steps. Therefore, one full cycle consists of 100 time steps. Since the simulation is done for 25 cycles, the total number of time steps is 2500 which is illustrated in Fig. 4.14. There are horizontal lines in the temperature profile because for one half of one cycle the flow of the HTF temperature is from control volume 29 to control volume 30 during the Hot-to-Cold blow in the SIMULINK model, and during the Cold-to-Hot blow, the constant value of HTF temperature at the cold side enters control volume 30 in the SIMULINK model.

A similar plot is made for the solid MCM for the last control volume shown in Fig. 4.15. The conditions are the same as those used to obtain the plot in Fig. 4.14.
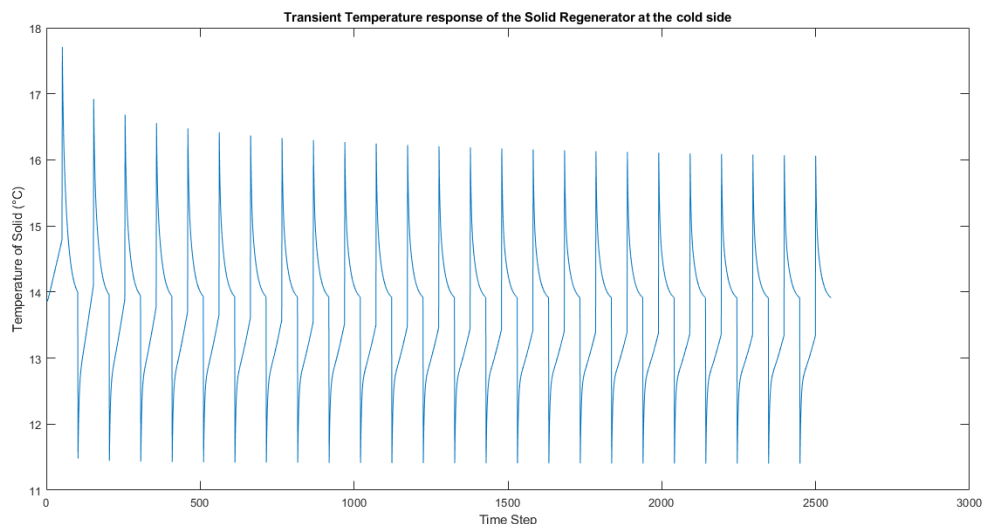
Figure 4.15: Transient temperature response of the Solid at the cold side: The plot has discontinuities due to the instantaneous magnetization and demagnetization.

The discontinuities in the plot shown in Fig. 4.15 are due to the instantaneous application and removal of the magnetic field at the end of each blowing process.

The transient temperature response of the solid at the cold side can also be analyzed with the help of a T-s diagram similar to that shown in Fig. 3.7. The transient temperature response is shown in Fig. 4.16 in the form of a T-s diagram with the steps of the AMR cycle.
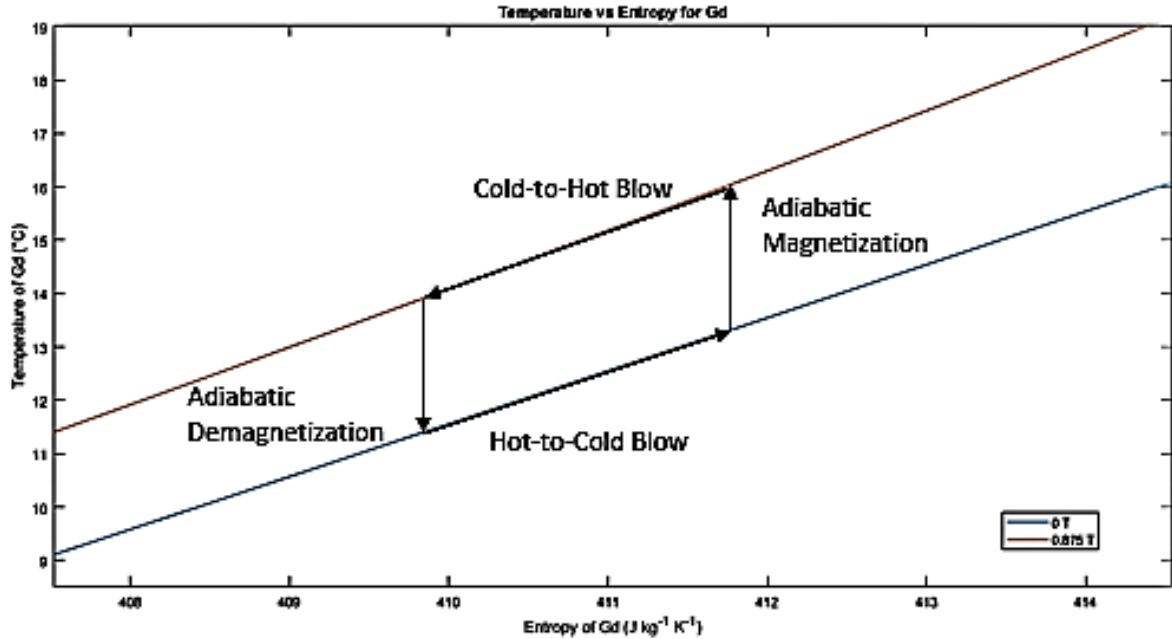
Figure 4.16: Transient temperature response of the Solid at the cold side with T-s diagram: The four stages of the magnetic heat pump cycle are depicted for the solid MCM at the cold side.

In Fig. 4.16, the adiabatic temperature increase and decrease during the instantaneous magnetization and demagnetization can be compared with the vertical lines in the plot shown in Fig. 4.15. During the adiabatic magnetization, the temperature of the solid goes up from around 13.2°C to around 15.9°C, that can be seen in both Fig. 4.15 and Fig. 4.16. The same is observed in both Fig. 4.15 and Fig. 4.16 for the demagnetization, where the temperature of the solid decreases from around 13.9°C to around 11.4°C.

4.4. Methods of Optimizing the Heat Pump Performance

The sensitivity analysis developed in the previous parts of the chapter is helpful in obtaining methods for optimizing the performance of the heat pump system. For a heat pump, the parameters that are considered for optimization are the heating capacity, the heating COP and the temperature span. The cooling capacity is not considered, since this is not a relevant parameter of a heat pump and also because the methods for optimizing the heating capacity are similar to those for optimizing the cooling capacity. The methods for increasing the heating capacity of the heat pump are as follows:

1. Decrease in the diameter of the particle increases the specific surface area for heat transfer, thereby increasing the heating capacity.

2. Reducing the porosity of the regenerator packed bed helps in increasing the mass of the solid MCM in the regenerator. Therefore, more energy can be stored in the regenerator at a particular instant of time. Therefore, the heating capacity increases significantly. It also increases the specific surface area of the regenerator packed bed per unit volume, therefore, it enhances the heat transfer between the solid and the HTF.

3. Increasing the frequency of the cycle, reduces the blowing time. This may result in less heat entering the HTF from the surroundings through the casing and in achieving more magnetization processes per unit time. Therefore, it increases the heating capacity of the regenerator. Moreover, increasing the cycle frequency, requires a proportional increase in the volumetric flow rate in order to maintain the

utilization factor. Increasing the volumetric flow rate increases the convective heat transfer coefficient, thereby increasing the heating capacity.

The methods used for increasing the maximum temperature span are the following:

1. Reduction in particle diameter.

2. Reducing the porosity of the regenerator.

3. Reducing the heat added to the HTF from the environment through the regenerator casing.

The following methods can be used for increasing the calculated heating COP of the system:

1. Decreasing the particle diameter helps in increasing the heating capacity and cooling capacity, thereby increasing the COP of the regenerator. The decrease in particle diameter also leads to an increase in the required pumping power, which means more work required for the cycle resulting in a lower COP. This is not considered while calculating the COP. Therefore, it is assumed that the magnitude of increase in heating capacity exceeds the magnitude of increase in the required pumping power, thereby increasing the COP of the regenerator.

2. Decreasing the cycle frequency, means less number of magnetization processes per unit time. This results in less work being done, and therefore, the COP increases. On the contrary, decreasing the cycle frequency also decreases the heating capacity, but since there is an overall increase in the COP, it is assumed that the magnitude of decrease in the power of magnetization is larger than the magnitude of decrease in heating capacity, resulting in higher heating COP.

3. Decreasing the porosity of the regenerator, results in a significant increase in the heating capacity and cooling capacity. Therefore, it significantly increases the COP of the regenerator. Decreasing the porosity also increases the required pumping power, but the magnitude of this decrease is less than the magnitude of increase in the heating capacity, resulting in an increase in the heating COP.

4. Decreasing the heat added from the environment increases the cooling capacity and decreases the heating capacity. Therefore, the difference between the heating capacity and cooling capacity reduces, resulting in an increase in COP as per Eq. (3.35).

From the above listed methods to enhance each of the performance parameters of the regenerator, it is clear that some of the methods are common like decreasing the particle diameter and decreasing the porosity. However, on increasing the temperature span, the heating capacity decreases and vice-versa. Therefore, it is possible to have a regenerator with a very high temperature span and a low heating capacity, and a very high heating capacity but with near zero temperature span. Although this is the case, it is preferred to have a balance between these two parameters. Therefore, a good combination with an in-between value of heating capacity and temperature span is required. This is the process of optimization, wherein the most suitable combination of performance is found. The cooling capacity is also enhanced along with the heating capacity with a decrease in temperature span and vice-versa. Therefore, it is better to analyze only one of cooling capacity or heating capacity and the temperature span. The heating capacity is chosen because it is the more relevant parameter for a heat pump.

The plots in Fig. 4.7 and Fig. 4.8 suggest that the increase in cycle frequency results in a significant increase in the heating capacity. This is the case for temperature spans below 18 K. It is also noticed from these plots that for a temperature span around 10 K and a cycle frequency of 2.5 Hz, the heating capacity is around 170 W. The resulting heating COP for this combination is around 4.86. This is a combination for an in-between value of temperature span which is giving a good combination of heating capacity. The COP is also reasonable, and can be improved by other methods like reducing the particle diameter and the porosity, keeping the temperature span at 10 K and the cycle frequency at 2.5 Hz. Implementing these methods can also result in an increase in the heating capacity. With this increase in heating capacity, the temperature span of the regenerator can be further expanded. Therefore, this is one method of optimizing the performance of the regenerator such that the right combination of performance is found. The performance parameters of the regenerator are obtained for in-between temperature spans like 10 K, 15 K. The performance parameters of the regenerator are also obtained for a temperature span of 20 K, since this is a requirement for the application

of heat pumps to Dutch dwellings.

Table 4.2 shows the performance parameters of the regnerator for temperature spans of 10 K and 15 K for the standard design as per Huang et al. (2019) [18].

Table 4.2: Performance of Regenerator for standard design with a cycle frequency of 1.7 Hz

$T_{span}(K)$	$\dot{Q}_{cool}$ (W)	$\dot{Q}_{heat}$ (W)	COP_{heat}
10	96	117	5.57
15	42.5	67.5	2.7

For the application of heat pumps to Dutch dwellings, the required temperature span is at least 20 K. As per the trend in Table 4.2, the temperature span cannot reach 20 K in the standard design, as it will result in a negative cooling capacity, which means the heat source will not function correctly. Also, for a temperature span of 15 K, the cooling and the heating capacity are not that high. Therefore, the frequency of the cycle is increased to 2.5 Hz in order to increase the cooling capacity and heating capacity of the regenerator. The results of this implementation are shown in Table 4.3 for temperature spans of 10 K and 15 K.

Table 4.3: Performance of Regenerator for a cycle frequency of 2.5 Hz

$T_{span}(K)$	$\dot{Q}_{cool}$ (W)	$\dot{Q}_{heat}$ (W)	COP_{heat}
10	135	170	4.86
15	56	90	2.65

Table 4.3 shows that for a frequency of 2.5 Hz, the cooling capacity and heating capacity have increased significantly. However, this impact is lowered as the temperature span gets to 15 K as per the trend. Therefore, the temperature span is not enhanced by increasing the cycle frequency. Also, the COP decreases with an increase in the cycle frequency. Therefore, the particle diameter is decreased to 0.0004 m and the porosity is decreased to 0.3. The performance of the regenerator for a particle diameter of 0.0004 m (keeping the other parameters at the standard values) is shown in Table 4.4 for temperature spans of 10, 15 and 20 K.

Table 4.4: Performance of Regenerator for a particle diameter of 0.0004 m

$T_{span}(K)$	$\dot{Q}_{cool}$ (W)	$\dot{Q}_{heat}$ (W)	COP_{heat}
10	112	136	5.67
15	60.87	87.06	3.32
20	16.72	45.55	1.58

From Table 4.4, it is clear that the temperature span reaches 20 K, with a low cooling capacity and a low heating capacity. The heating COP is also low in this case. For temperature spans of 10 K and 15 K, the values of the heating capacity and cooling capacity are lower than the respective values in Table 4.3 for a higher frequency, but the heating COP is higher for the respective values in Table 4.3. Therefore, with a decrease in particle diameter, the heating capacity, cooling capacity and COP can be enhanced. This evident from comparing the COP values in Table 4.4 and those in Table 4.2, wherein the COP is slightly higher in Table 4.4 then Table 4.2, for a particular temperature span. The results for a decreased porosity value of 0.3 are shown in Table 4.5.

Table 4.5: Performance of Regenerator for a porosity of 0.3

$T_{span}(K)$	$\dot{Q}_{cool}$ (W)	$\dot{Q}_{heat}$ (W)	COP_{heat}
10	127	148.6	6.88
15	74	97	4.22
20	19.65	48.96	1.67

As per Table 4.5, decreasing the porosity to 0.3 increases the heating capacity, cooling capacity and the heating COP. Therefore, a temperature span of 20 K is reached with this implementation. The values of the heating capacity, cooling capacity and COP are still low, but they are higher than the corresponding values in Table 4.4. Therefore, a combination of increased cycle frequency, decreased particle diameter and decreased porosity can produce a good optimum value of heating capacity, cooling capacity and heating COP for the corresponding temperature spans of 10, 15 and 20 K. The performance parameters of the regenerator are obtained after increasing the cycle frequency to 2.5 Hz, decreasing the particle diameter to 0.0004 m and decreasing the porosity to 0.3, and the results are shown in Table 4.6.

Table 4.6: Performance of Regenerator for a cycle frequency of 2.5 Hz, particle diameter of 0.0004 m and porosity of 0.3

$T_{span}(K)$	$\dot{Q}_{cool}$ (W)	$\dot{Q}_{heat}$ (W)	COP_{heat}
10	193.11	235.06	5.66
15	117.96	164.2	3.55
20	48.44	99.1	1.96

Table 4.6 shows that after implementing an increased frequency, decreased particle diameter and decreased porosity, the heating capacity and cooling capacity increase significantly for each of the temperature spans in Table 4.6. The increase in the heating COP is not so significant compared to those of heating capacity and cooling capacity, given the fact that the COP reduces for an increase in frequency. For an in-between temperature span of 15 K, the heating capacity has a reasonable value of 164.2 W. Also, for a temperature span of 20 K, the heating capacity of the device is 99.1 W, which is also comparatively reasonable. Therefore, the heating capacity and the temperature span have been optimized, since a reasonable in-between value is obtained for both. The COP is only slightly enhanced during this optimization.

4.5. Discussion

From the sensitivity analysis, it is clear that the temperature span and the heating capacity are enhanced by reducing the particle diameter, reducing the porosity and increasing the cycle frequency. Although it is helpful in obtaining the maximum temperature span for a minimum heating load, and the maximum heating capacity for a minimum temperature span, a balance of these parameters is always preferred. Therefore, an optimization is done in order to obtain reasonable values for temperature span as well as heating capacity. After optimization, a heating capacity of 99.1 W is obtained for a temperature span of 20 K. In order to understand whether the magnetocaloric heat pump is suitable for Dutch dwellings based on the findings from the optimized model, it is important to understand its thermal requirements.

As per the discussion in Chapter 2, the heating required in Dutch dwellings is divided into two parts: the space heating and the hot water buffer. The temperature requirement for the hot water buffer is much higher than that for space heating. The temperature of the HTF that is required for the space heating is 35-40°C and that for hot water buffer is around 50-60°C. Although the temperature requirement for the hot water buffer is higher, the thermal power requirement for the space heating is much higher than that required for the hot water buffer. The space heating requires 1.8 kW, while the hot water buffer requires 0.9 kW. After model optimization, the heating capacity is only 99.1 W for a temperature span of 20 K. Therefore, as far as temperature span is concerned, the device is better suited for space heating than the hot water buffer, since the HTF gets closer to the required temperature for the space heating in the hot side of the heat pump. However, as far as the thermal power is concerned, the device is not suited for any part of the heating in Dutch dwellings, since it only gives 99.1 W for 20 K temperature span. It is also to be noted that the model that is developed is optimistic, since most of the thermal losses and certain aspects of the heat transfer are not considered. Therefore, a more realistic model would indicate that the magnetocaloric heat pump device may not be suitable even for the temperature requirement of the space heating.

5

Conclusion and Further Recommendations

A heat transfer model for the AMR heat pump cycle has been developed and compared using the findings reported in the Literature Review. A sensitivity analysis was conducted for the model. From the sensitivity analysis, methods of optimizing the performance are deduced and reported. The following conclusions are drawn based on the sensitivity analysis:

1. The maximum COP is obtained for zero temperature span and a porosity of 0.3, with a value of 14.21.

2. The maximum heating capacity of the device is obtained for zero temperature span and a cycle frequency of 2.5 Hz, with a value of around 286.6 W.

3. The maximum cooling capacity of the device is obtained for a cycle frequency of 2.5 Hz and zero temperature span, with a value of around 263.7 W.

4. The maximum temperature span of the device that can be obtained for a particle diameter of 0.0004 m. Its value will be around 22 K.

5. The parameter that influences the performance of the regenerator system the most is its porosity. This is due to the fact that the porosity influences a few important parameters of the device like the amount of solid MCM in a given bed volume and the specific surface area per unit regenerator volume, which result in higher convective heat transfer coefficient. Therefore, it influences the heating capacity, cooling capacity and the COP significantly.

6. The frequency of the cycle also has a significant impact on the heating capacity and the cooling capacity of the cycle up to temperature spans of around 17 to 18 K. However, it does not have a profound impact on the COP of the cycle

7. The heat losses through the casing have very little impact on the performance of the regenerator.

There are other conclusions that can be drawn based on optimizing the regenerator model:

1. Since the highest frequency gives the best heating capacity, for zero temperature span, it is further justified that this frequency can be implemented for obtaining the optimum temperature span between 0 and 18 K which gives a reasonable heating capacity.

2. It is observed that for a cycle frequency of 2.5 Hz and a temperature span of 10 K, a heating capacity of 170 W is obtained. The COP is also reasonable with a value of around 4.86.

3. The COP can be improved by operating at the same frequency and temperature span but decreasing the particle diameter and porosity. This also results in an increase in the heating capacity along with the increase in COP.

4. After optimizing the regenerator by increasing the frequency to 2.5 Hz, reducing the particle diameter to 0.0004 m and reducing the porosity to 0.3, the heating capacity and the temperature span are optimized. For a temperature of 15 K, the heating capacity that is obtained is 164.2 W and for a temperature span of 20 K, the heating capacity is 99.1 W.

5. As far as the temperature requirement is concerned, the device is better suited for space heating than the hot water buffer. However, as far as the thermal power requirement is concerned, the device is suited neither for the space heating, nor the hot water buffer.

The following are further recommendations on approaching the project differently and developing it further:

1. The project can be approached differently by simulating for two regenerators that are operating alternatively. This means that when one regenerator undergoes the Hot-to-Cold blowing process, the other regenerator undergoes the Cold-to-Hot blowing process. In this way, a thermal load can be added and the model can be optimized as per the thermal requirements of Dutch dwellings. Such a model can be created for each part of the heat load that Dutch dwellings require.

2. Another development in the model that can be implemented is the use of the heat transfer equations for the BHE reported in previous chapters along with the heat transfer equations for the regenerator, and therefore, connect the heat source to the regenerator.

3. In order to further improve the performance of the regenerator, a higher magnetic field of around 2 T can be applied to the regenerator model. 2 T is the maximum field that can be applied for a permanent magnet. A permanent magnet is preferred because it has better availability and is less expensive.

4. Gd can be replaced by another MCM, which is preferably an alloy of Gd, since it will provide a higher MCE for a particular magnetic field. This will result in better regenerator performance. However, the use of Gd based alloys is more expensive compared to pure Gd.

5. The heating capacity and temperature span can be further improved by increasing the dimensions of the regenerator. This means more energy stored in the regenerator after magnetization due to increased regenerator volume. However, this should be done keeping in mind that the regenerator should fit well into the air gap of the permanent magnet such that, the regenerator gets fully magnetized when the magnets passes through it. This can result in analyzing the influence of the aspect ratio on the performance of the regenerator, since it is the ratio of the width to the height of the regenerator.

6. If the dimensions of the regenerator cannot be increased too much owing to the size of the air gap, another method would be to add more regenerators to the system. This increases the heating capacity of the heat pump. But it would result in a more expensive system due to the addition of more components.

Bibliography

[1] Negrao, C. O. R., Hermes, C. J. L. (2011), *Energy and cost savings in household refrigerating appliances: A simulation-based design approach*, Applied Energy 88 (2011) 3051–3060

[2] Kitanovski, A. (2020), *Energy Applications of Magnetocaloric Materials*, Advanced Energy Materials 2020, 10, 1903741

[3] Sarkar, A. B. (2017), *Magnetocaloric effect and magnetic refrigeration*, Department of Physics, IIT Kanpur

[4] Brown, G. V. (1976), *Magnetic heat pumping near room temperature*, Appl Phys 47 (1976) 3673–3680

[5] Pecharsky, V. K., Gschneidner Jr., K. A. (1997), *Giant Magnetocaloric Effect in $Gd_5(Si_2Ge_2)$*, Physical Review Letters, Volume 78, Number 23

[6] Pecharsky, V. K., Gschneidner Jr., K. A. (2000), *Magnetocaloric Materials*, Annu. Rev. Mater. Sci. 2000. 30:387–429

[7] Miller, C. W., Belyea, D. D., Kirby, B. J. (2014), *Magnetocaloric effect in nanoscale thin films and heterostructures*, J. Vac. Sci. Technol., A 32, 040802 (2014)

[8] Belo, J. H., Pires, A. L., Araujo, J. P., Pereira, A. M. (2019), *Magnetocaloric materials: From micro- to nanoscale*, Early Career Scholars in Material Sciences 2019: Reviews

[9] Jeong, S. (2014), *AMR (Active Magnetic Regenerative) refrigeration for low temperature*, Cryogenics 62 (2014) 193–201

[10] Shah, Hardik V., Shahapure, Rahul M., Menghani, Prof P. D., Sawant, Prof. V. P. (2017), *Study of Magnetic Refrigerator Based on AMR Cycle*, International Conference on Ideas, Impact and Innovation in Mechanical Engineering (ICIIIME 2017), Volume: 5 Issue: 6, 582-588

[11] Saito, A. T., Kobayashi, T., Fukuda, H., Arai, R., Nakagome, H. (2016), *Cooling Properties of Gd Alloys and $La(Fe, Si)_{13}$-Based Compounds in Active Magnetic Refrigeration for Environmentally-Friendly Cooling Systems*, International Journal of Environmental Science and Development, Vol. 7, No. 5, May 2016

[12] Pecharsky, V. K., Gschneidner Jr., K. A. (1999), *Magnetocaloric effect and magnetic refrigeration*, Journal of Magnetism and Magnetic Materials 200 (1999) 44-56

[13] Trevizoli, P. V., Christiaanse, T. V., Govindappa, P., Niknia, I., Teyber, R., Barbosa Jr., J. R., Rowe, A. (2016), *Magnetic heat pumps: An overview of design principles and challenges*, Science and Technology for the Built Environment (2016) 00, 1–13

[14] Torregrosa-Jaime, B., Vasile, C., Risser, M., Muller, C., Corberan, J., Paya, J. (2013), *Application of Magnetocaloric Heat Pumps in Mobile Air- Conditioning*, SAE Int. J. Passeng. Cars - Mech. Syst. 6(2): 2013

[15] Torregrosa-Jaime, B., Vasile, C., Risser, M., Muller, C., Corberan, J., Paya, J. (2014), *Sizing of a reversible magnetic heat pump for the automotive industry*, International Journal of Refrigeration 37 (2014) 156-164

[16] de Vries, W., van der Meer, T. H. (2017), *Applications of Peltier thermal diodes in a magnetocaloric heat pump*, Applied Thermal engineering, Vol. 111, pp. 377-386.

[17] Aprea, C., Cardillo, G., Greco, A., Maiorino, A., Masselli, C. (2016), *A rotary permanent magnet magnetic refrigerator based on AMR cycle*, Applied Thermal Engineering 101 (2016) 699–703

[18] Huang, B., Lai, J., W., Zeng, D., C., Zheng, Z., G., Harrison, B., Oort, A., van Dijk, N., H. (2019), *Development of an experimental rotary magnetic refrigerator prototype*, International Journal of Refrigeration 104 (2019) 42–50

[19] Nielson, K. K. (2010), *Numerical modeling and analysis of the active magnetic regenerator*, Technical University of Denmark

[20] Johra, H., Filonenko, K., Heiselberg, P., Veje, C., Dall'Olio, S., Engelbrecht, K., Bahl, C. (2019), *Integration of a magnetocaloric heat pump in an energy flexible residential building*, Renewable Energy 136 (2019) 115-126

[21] Risser, M., Vasile, C., Muller, C., Noume, A. (2013), *Improvement and application of a numerical model for optimizing the design of magnetic refrigerators*, International Journal of Refrigeration 36 (2013) 950-957

[22] Kamran M. S., Sun, J., Tang, Y. B., Chen, Y. G., Wu, J. H., Wang, S. H. (2016), *Numerical investigation of room temperature magnetic refrigerator using microchannel regenerators*, Applied Thermal Engineering 102 (2016) 1126–1140

[23] Kamran M. S., Sun, J., Tang, Y. B., Chen, Y. G., Wu, J. H., Wang, S. H. (2016), *Performance optimisation of room temperature magnetic refrigerator with layered/multi-material micro-channel regenerators*, International Journal of Refrigeration 68 (2016) 94–106

[24] Mugica, I., Poncet, S., Bouchard, J. (2018), *3D Direct Numerical Simulation of Magneto-Caloric regenerators*, International Refrigeration and Air Conditioning Conference. Paper 2018

[25] Singh, R. K., Sharma, R. V. (2017), *Numerical analysis for ground temperature variation*, Geothermal Energy 5, Article number: 22 (2017)

[26] Al-Khoury, R., Kolbel, T., Schramedei, R. (2010), *Efficient numerical modeling of borehole heat exchangers*, Computers Geosciences 36 (2010) 1301–1315

[27] Rees, S. J., He M. (2013), *A three-dimensional numerical model of borehole heat exchanger heat transfer and fluid flow*, Geothermics 46 (2013) 1– 13

[28] NL Soil Temperatures, `http://projects.knmi.nl/cabauw/insitu/observations/soiltemp/`

[29] The Engineering ToolBox,
`https://www.engineeringtoolbox.com/ethylene-glycol-d`$_1$`46.html`

[30] Mills, A. F., (1998), *Basic Heat and Mass Transfer*, Pearson Education

[31] Bjork, R., Bahl, C. R. H., Katter, M., (2010), *Magnetocaloric Properties of $LaFe_{13-x-y-}Co_xSi_y$ and commercial grade Gd*, Journal of Magnetism and Magnetic Materials 322 (2010) 3882–3888